Mesoscience & Nanotechnology

Volume 1, Issue 1, September 2025

ISSN: 3034-6622

ΜΕΣΟ

Table of contents

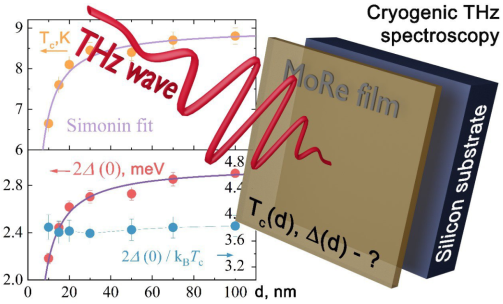

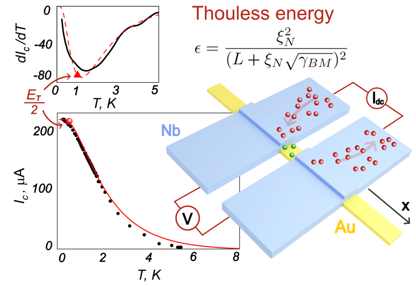

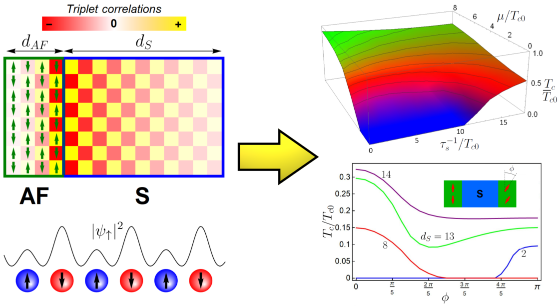

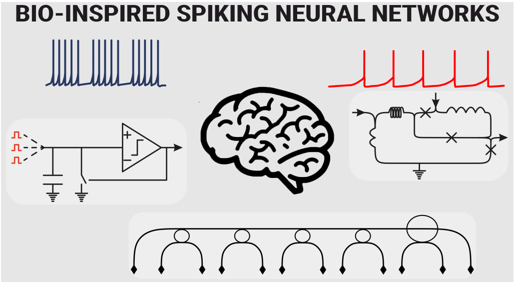

& Nanotechnology Science

DOI: 10.64214/jmsn.01.01001 **Editorial**

Welcome to Mesoscience & Nanotechnology

A Journal Facilitating Open Science Across the Intersect of Mesoscopic Physics and Nanotechnology

V. S. Stolyarov

Editor-in-Chief of the Mesoscience & Nanotechnology

submitted 1 December 2023, published 8 December 2023

Dear Colleagues,

Throughout the latter half of the twentieth century, there was a remarkable surge in scientific exploration encompassing physical processes across various length scales from the atomic to the macroscopic. This trend is particularly evident in the research of nanosized devices and quantum materials along with a comprehensive understanding of their characteristics. The strides made in this field have been facilitated by the invention of innovative methods for producing low-dimensional, topological, and other materials. Additionally, the development of sophisticated techniques has allowed for the examination and precise control of physical and chemical parameters across different length scales.

This scientific progress has spurred global advancements in physics, generating heightened interest in a variety of artificial structures such as superlattices, heterostructures, quantum dots, thin films, and interfaces. Consequently, researchers are expanding their focus beyond purely theoretical issues, turning their attention to current and future practical applications in real-world nanodevices. Mesoscopic physics and chemistry, or Mesoscience can be considered a critical bridge between physics at the nano- and micro- scales, encompassing both fundamental and applied research. This motivation has inspired us to launch a new international scientific journal, Mesoscience & Nanotechnology, dedicated to facilitating the exchange of scientific information. In a commitment to fostering an open platform for knowledge sharing, we have opted for a *free-of-charge* publication format, benefiting both readers and authors.

Developed *by scientists for scientists*, our journal emphasizes responsiveness, high-level research contributions, rigorous peer-review standards, and an unwavering commitment to scientific ethics devoid of any political and other biases. We firmly believe that this approach will propel the advancement of Mesoscience on a global scale.

Covering a wide array of topics, the journal spans superconductivity and superconducting devices, nanoelectronics and nanotechnology, surfaces and interfaces, functional materials (fabrication and properties), quantum physics and materials, topologically protected electronic phenomena, 2D materials and devices, quantum dots, low-dimensional magnetism and superconductivity, heterostructures and superlattices, strongly correlated electronic systems, ferroelectricity, multiferroics, thin films, neuromorphic systems, nanobiotechnology, and innovative methods.

Mesoscience & Nanotechnology operates as a peer-reviewed, *open-access* interdisciplinary journal, publishing original research results in various formats, including articles, letters, reviews, methodological notes, and analyses of perspectives and trends across physics, chemistry, materials science, and related disciplines. Notably, our non-commercial initiative is led by individuals passionate about fostering scientific discourse. The list of editors can be accessed on the journal's website: jmns.press.

We invite authors worldwide to submit their manuscripts for prompt consideration. The editorial board is committed to making the first decision on manuscript suitability for further consideration and publication within 10 days. All submissions will then go through a rigorous single-blind review process conducted by three referees with the first evaluation round expected to conclude within 21 days of submission. Upon acceptance, manuscripts undergo proof preparation before electronic publication on the journal's website under the CC BY-NC-ND 4.0 license, allowing free distribution. Our aim is to garner community support and expedite the inclusion of Mesoscience & Nanotechnology in national and international abstract and citation databases, including Crossref, Web of Science, Scopus, RSCI, and others.

We are proud to present the inaugural issue of Mesoscience & Nanotechnology, the result of dedicated efforts from authors, reviewers, members of the editorial board, and IT engineers.

On behalf of the Editorial Board,

Prof. Vasily S. Stolyarov,
Editor-in-Chief
editor.chief@phtreatise.com

DOI: 10.64214/jmsn.01.01002 **Article**

Thickness-dependent superconductivity in MoRe films studied by terahertz spectroscopy

E. S. Zhukova,[1] B. M. Nekrasov,[1] L. S. Kadyrov,[1] A. V. Melentev,[1] A. S. Shaimardanov,[1,2] A. G. Shishkin,[1,2,3] A. A. Golubov,[4] M. Yu. Kupriyanov,[2,5] B. P. Gorshunov,[1] and V. S. Stolyarov[1,2,3]

[1] *Moscow Institute of Physics and Technology (National Research University), 141700 Dolgoprudny, Russia*
[2] *National University of Science and Technology (MISIS), 119049 Moscow, Russia*
[3] *Dukhov Research Institute of Automatics (VNIIA), 127055 Moscow, Russia*
[4] *Faculty of Science and Technology and MESA+ Institute for Nanotechnology, University of Twente, 7500 AE Enschede, Netherlands*
[5] *Skobeltsyn Institute of Nuclear Physics, Lomonosov Moscow State University, 119991 Moscow, Russia*

submitted 9 Septemper 2023, accepted 24 November 2023, published 8 December 2023

Terahertz time-domain spectroscopy is used to perform the first detailed studies of the electrodynamic properties of MoRe (60%/40%) films with thicknesses ranging from 10 to 100 nm. Films are prepared by magnetron sputtering technique on silicon substrates. The critical temperatures vary from 6.5 K (for 10 nm film) to 9.5 K (for 100 nm film). Spectra of complex permittivity, conductivity, refraction index, surface impedance and reflection coefficient for the films are acquired at frequencies 0.15–2.4 THz (wavenumbers 5–80 cm^{-1}) and in the temperature interval $T = 5$–300 K. For all films, temperature dependencies of the superconducting energy gap, penetration depth, superconducting condensate plasma frequency, and normalised superfluid density are obtained on a quantitative level. It is shown that the reduction of film thickness leads to a strong decrease of the critical temperature and magnitude of the energy gap. The observed suppression of superconductivity is assigned to reduction of the superconducting order parameter due to the contribution to the free energy of the electronic energy states at the surface of superconductor. The MoRe films with the obtained characteristics can be used in designing advanced superconducting electronic devices.

Introduction

Molybdenum-rhenium superconducting alloys continue to attract the attention of researchers from a fundamental viewpoint because of their intriguing properties in the superconducting (SC) state as well as their significant potential for use in modern electronics. Mo$_{1-x}$Re$_x$ films exhibit superconductivity with a superconducting critical temperature T_c reaching up to 15 K,[1–4] which is of the order of magnitude higher than $T_c = 0.9$ K in Mo and $T_c = 1$ K in Re.[5] The compounds are $s-$wave type-II superconductors, with the upper critical field of 8 T at 4 K.[6–8] There are indications of a two-band/two-gap superconductivity in the MoRe alloys[9,10] allowing to consider them as materials for the studies of multiband superconductivity. As an intriguing property, one can consider an electronic topological transition that is observed around the critical concentration $x_c = 0.11$[11–13] making MoRe an ideal playground for study of time-reversal symmetry breaking in unconventional superconductors.[14]

Thin MoRe films exhibit excellent superconducting properties,[15] stable chemical, electrical and mechanical characteristics,[15–17] high radiation stability,[18] ability to make good electrical contact with carbon-based materials (graphene, carbon nanotubes),[19] stability for electron beam lithography.[20] All of these properties have revived a lively interest in MoRe alloys in the context of their use in developing elements for modern electronic systems. As a transparent for carriers interface to graphene and carbon nanotubes,[8,19] MoRe films are promising for the development of elements for quantum computation[21,22] and quantum memory.[23,24] Few nanometers thick MoRe films can be used for the fabrication of SQUID-on-tip devices with enhanced characteristics[20,25] and spin-qubit elements.[26,27]

The growing interest in thin MoRe films has emerged among communities working on developing sensitive single-photon detectors.[15,28] These detectors commonly use NbN thin films with the critical temperature T_c close to 9 K (for a 4 nm-thick film).[28] With the doubled SC energy gap $2\Delta \approx 6$ meV (for 15 nm thick film),[29] high quantum efficiency NbN-based detectors operating in visible and middle infrared spectra regions can be realized.[28] To achieve even lower, terahertz (THz) working frequencies, superconductors with smaller gap values are necessary. Numerous compounds fit this requirement, such as MoSi ($2\Delta(0) = 2.28$ meV), MoGe ($2\Delta(0) = 2.2$ meV), WSi ($2\Delta(0) = 1.52$ meV), and NbSi ($2\Delta(0) = 0.94$ meV), as reported in Ref.[30] (here $\Delta(0)$ stands for the SC energy gap at zero temperature). However, their critical temperatures are rather low even for bulk samples. Thin MoRe films stand out because of their relatively high T_c values, which is close to that for NbN films.

Thus, detailed studies of the electrodynamic properties of MoRe films in sub-terahertz and terahertz frequency domains are needed. In this frequency range the temperature evolution of the superconducting gap can be spectroscopically traced in detail and analyzed. In addition, operating frequencies of electronic communication systems of the next generation indeed belong to this range. Since such studies have not been reported so far, our goal was to perform the first systematic measurements and analyses of the electrodynamic characteristics of Mo$_{0.6}$Re$_{0.4}$ films with various thicknesses at frequencies $f = 0.15 - 2.4\,\mathrm{THz}$ (wavenumbers $\nu = 1/\lambda_{\mathrm{cm}} = 5 - 80\,\mathrm{cm}^{-1}$, where λ_{cm} is radiation wavelength in cm) and in the temperature interval $T = 5 - 300\,\mathrm{K}$.

Results and discussion

Experimental procedure. The $\mathrm{Mo}_{0.6}\mathrm{Re}_{0.4}$ films were prepared by magnetron sputtering on highly insulating and thus transparent for terahertz radiation silicon substrates of thickness ≈0.5 mm, as described in Ref. [20] Films thicknesses were 10, 15, 20, 30, 50, 70, and 100 nm. Terahertz characteristics of the films were determined using the commercial TeraView TPS Spectra 3000 time-domain spectrometer by measuring complex-valued (amplitude and phase) transmission coefficient spectra of the films on the substrates. Temperature-dependent THz spectra of the real parts of permittivity $\varepsilon'(\nu, T)$ and conductivity $\sigma'(\nu, T)$ of the MoRe films were calculated with the TeraCalc software. This employs numerical solution of the system of two essentially non-linear equations for the amplitude $Tr(\varepsilon', \sigma')$ and the phase $\varphi_{Tr}(\varepsilon', \sigma')$ of the complex transmission coefficient $Tr(\varepsilon', \sigma')\exp[i\varphi_{Tr}(\varepsilon', \sigma')]$ of a two-layered system (a film on a substrate), see Eqs. (1)–(5) in Supporting Information. Other quantities, such as the real and imaginary parts of the complex refractive index $n^* = n + ik$, and the surface impedance $Z_s = R_s + iX_s$, were also calculated using standard expressions (see, *e. g.*, textbook[31]). THz parameters of the Si substrates were determined beforehand. Measurements were performed in a quasi-optical configuration of the measurement scheme of the spectrometer, with a homemade helium-flow cryostat equipped with Mylar windows.

Normal state. Figure 1a shows room-temperature spectra of transmission coefficient Tr of the bare silicon substrate and of substrates with $\mathrm{Mo}_{0.6}\mathrm{Re}_{0.4}$ films of thickness 10, 20, 50, and 100 nm. The periodic oscillations in the spectra arise from the interference of the electromagnetic waves inside the plane-parallel transparent substrate, which can be considered as a Fabry-Pérot resonator. The interval $\Delta\nu$ between oscillations is mainly determined by the substrate refraction index n and thickness d: $\Delta\nu = (2nd)^{-1}$, while the amplitudes of the peaks are determined by the transparency of the films. For the bare substrate, the transmission of the interferometric peaks reaches nearly unity, while the transmission of the peaks for the samples with MoRe films is significantly lower (at about two orders of magnitude for the 100 nm thick film). There is a phase shift at about π between the maxima observed for the bare substrate and the substrates covered with MoRe films. This is a consequence of impedance matching of the silicon-air interface by conducting $\mathrm{Mo}_{0.6}\mathrm{Re}_{0.4}$ film with a thickness smaller than the skin depth. The phenomenon was considered in detail in Refs.[32,33]

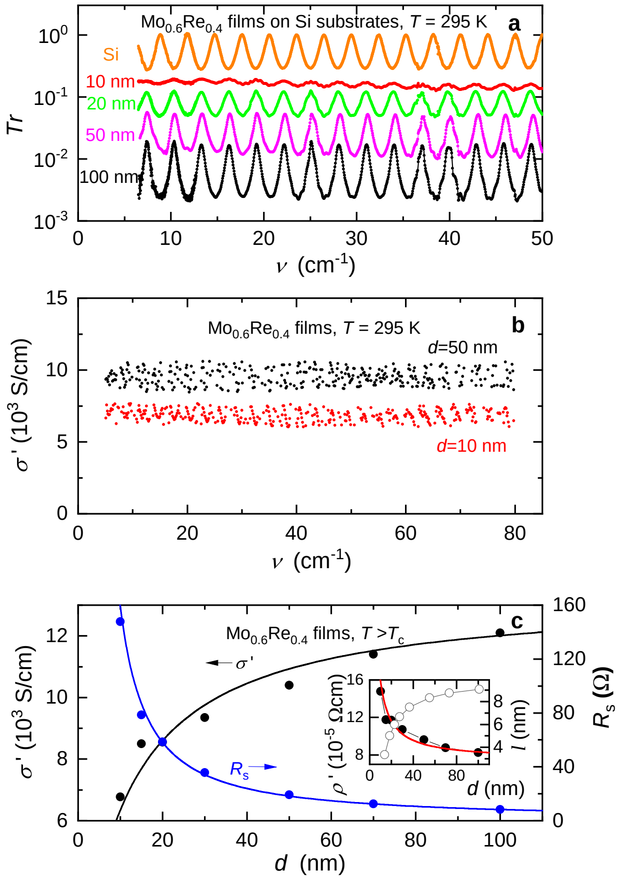

Figure 1. **a** – Room-temperature spectra of the transmission coefficient of $\mathrm{Mo}_{0.6}\mathrm{Re}_{0.4}$ films of various thicknesses deposited on silicon substrates. Periodic oscillations are due to the Fabry-Pérot effect – *i. e.* interference of electromagnetic waves inside plane-parallel substrate. **b** – Room-temperature dispersionless conductivity spectra of $\mathrm{Mo}_{0.6}\mathrm{Re}_{0.4}$ films of thickness $d = 50\,\mathrm{nm}$ and $d = 10\,\mathrm{nm}$. **c** – Thickness dependence of AC conductivity σ' (left axis) and surface resistance $R_s = (\sigma' d)^{-1}$ (right axis) in the normal state ($T > T_c$). Inset shows thickness dependence of AC resistivity $\rho' = 1/\sigma'$ and mean-free path l, determined from fit of $\rho'(d)$ with Eq. (1), for charge carriers in the films. Lines show least-square fits based on expression (1) from Ref.[35]

Spectra of transmission coefficient of all samples, as well as frequency dependences of conductivity and permittivity of all films did not reveal any significant changes during cooling from 300 K down to the critical temperature T_c, in accordance with the literature data.[34] At all temperatures in the normal state (at $T > T_c$) the conductivity spectra of all films were dispersionless, indicating the metal-type response in the low-frequency limit ($\nu \ll \gamma$, where γ is the scattering rate of carriers) of the Drude conductivity model.[36,37] This is demonstrated in figure 1b, where the conductivity spectra of two films, 10 nm and 50 nm thick, are shown as examples. Figure 1c shows the dependence of the normal-state AC conductivity σ', AC resistivity $\rho' = 1/\sigma'$, and surface impedance $(\sigma' d)^{-1}$ on the thickness d of the MoRe films. It is seen that the dependences are well described by the following expression obtained for granular films accounting additional scattering effects at film surface and grain boundaries[38]

$$\rho(d) = \rho_0 \left(1 + A\,\frac{l_0}{d}\right). \tag{1}$$

Here, ρ_0 and l_0 are the bulk resistivity and the bulk mean free path of the charge carriers, respectively, and A is a constant of the order of unity. Fitting the $\rho(d)$ depen-

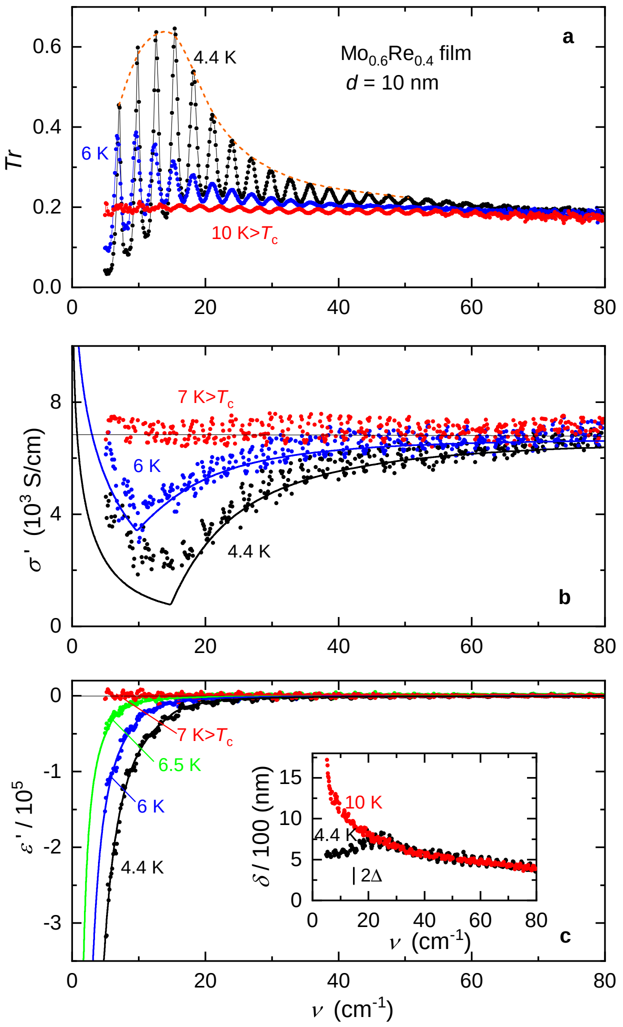

Figure 2. **a**, **b**, **c** – Frequency dependence of the transmission coefficient (**a**), the real part of AC conductivity (**b**), and the real part of dielectric permittivity (**c**) for 10 nm-thick $\mathrm{Mo_{0.6}Re_{0.4}}$ film on silicon substrate, measured at different temperatures above and below T_c. Oscillations in the spectra in panel **a** are due to the interference of radiation within the plane-parallel Si substrate. Red dashed envelope line shows that the oscillations at $T = 4.4$ K display broad maximum around the value $2\Delta/hc$. Inset in panel **c** represents radiation penetration depth[39] $\delta = (2\pi k\nu)^{-1}$ above and below T_c (here k is the extinction coefficient); vertical bar marks SC energy gap at 4.4 K. Solid lines in panels **b** and **c** are the least-square fits with BCS expressions.[40]

dence by Eq. (1) allows to determine $l_0 = 10$ nm and $\rho_0 = 75\,\mu\Omega$·cm. The value $l_0 = 10$ nm is more than two times larger than $l = 4.2$ nm obtained for MoRe alloy.[14] Taking the Fermi velocity $v_F = 2.34 \cdot 10^7$ cm/s,[14] we estimate the scattering rate of charge carriers $\gamma = v_F/(2\pi c l_0) \approx 120\,\mathrm{cm}^{-1}$ (c is the speed of light). This value lies above our working frequency interval, thus confirming that the normal-state response of the films corresponds to the low-frequency limit of the Drude conductivity model.

Superconducting state. Spectra of transmission coefficient, conductivity and permittivity of all studied films undergo strong changes when these films enter the SC state. This is demonstrated in figure 2 by the spectra obtained for 10 nm-thick MoRe film on silicon substrate (see also the spectra for 50 nm-thick MoRe film on silicon substrate in figure S1 in Supporting Information). These changes are typical for SC films as it was first demonstrated by Tinkham and coworkers[41–44] and reproduced later by other researchers in numerous experiments on conventional and high-T_c superconductors. As described below, by analyzing the spectra of the real parts of conductivity (σ') and permittivity (ε') through model fitting, we enable accurate determination of the critical temperature T_c (with an accuracy ±0.2 K) and the energy gap Δ (with an accuracy ±0.14 meV), as well as other characteristics of the SC state for MoRe films. At the lowest achievable temperature $T = 4.4$ K, the envelope for the interferometric peaks in the transmission spectrum (dashed red line in figure 2a) displays broad maximum around the value $2\Delta/hc$ (where h is Planck's constant), corresponding to the SC gap. The THz conductivity that characterizes absorption of radiation becomes suppressed at below $50 - 60\,\mathrm{cm}^{-1}$, showing a kink around $2\Delta/hc$ (figure 2b). Also, the dielectric permittivity strongly decreases below $20\,\mathrm{cm}^{-1}$ (see Ref.[45]) according to the relationship $\varepsilon' = -(\nu_{pl}^{SC}/\nu)^2$ representing dielectric response of SC condensate, where $\nu_{pl}^{SC} = (2\pi c)^{-1}\sqrt{4\pi n_e e^2/m^*}$ is the plasma frequency of SC condensate, n_e is the density of electrons in SC condensate, e is the electron charge, and m^* is the electron effective mass. The dielectric permittivity reaches large negative values that characterise the inductive response of Cooper-pairs condensate under the zero-frequency delta function in the conductivity spectrum. The superconducting transition also leads to strong changes in other electrodynamic quantities. Figure 3 shows the temperature evolution of the spectra of real and imaginary parts of the complex refraction coefficient $n^* = n + ik$ of the 10 nm-thick film (similar data for 50 nm-thick film is shown in figure S2). In the normal state, $n \approx k \sim (\sigma'/\nu)^{0.5}$, as expected for a good conductor.[36,37] Below T_c, the extinction coefficient k strongly increases and refraction index n decreases, leading to a strong enhancement in the bulk reflection coefficient R below $2\Delta/hc$ (inset in figure 3b).[†] Similar spectra for the 50 nm-thick film are presented in figure S2. One can see in figures 2b and 3a that in the SC state at low wavenumbers, $\nu < 2\Delta/hc$, there is significant scattering in the experimental data for the conductivity σ' and the refraction index n; it is especially pronounced for the 50 nm-thick film (figures S1 and S2). The reason is that the transmission spectra measured in the SC state are mainly determined by the large negative permittivity ε' and the large positive extinction coefficient k. As a result, both quantities ε' and k are determined much more precisely compared to σ' and n.[32,33,46]

To add more to the THz electrodynamic properties of

[†] Note that an ideal $s-$wave superconductor at $T = 0$ and $\nu < 2\Delta/hc$ would have zero AC conductivity σ' and large negative permittivity ε' values leading to $n = 0$ and $k \gg 1$. This case would correspond to an ideal reflector with a bulk reflection coefficient[31] $R_{bulk} = [(n-1)^2 + k^2]/[(n+1)^2 + k^2] = 1$.

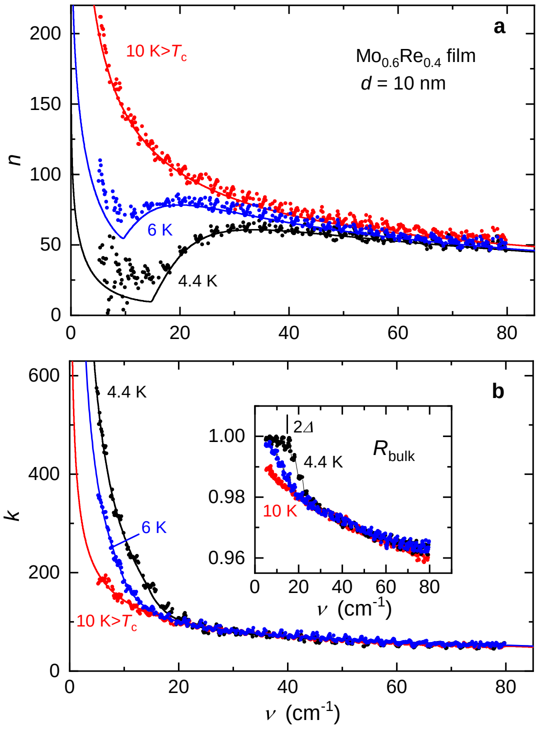

Figure 3. **a**, **b** – Frequency dependence of the refraction coefficient (**a**) and the extinction coefficient (**b**) for 10 nm-thick $Mo_{0.6}Re_{0.4}$ film on silicon substrate measured at temperatures above and below T_c. Solid lines in panel **b** for $T = 4.4$ K and $T = 6$ K are the least-square fits with BCS expressions;[40] lines corresponding to normal-state spectra at $T = 10$ K are plotted according to the low-frequency limit ($\nu \ll \gamma$) of the Drude conductivity model:[36,37] $n \approx k \approx (\sigma'/\nu)^{0.5}$. Inset in panel **b** shows spectra of the bulk reflection coefficient calculated according to the expression $R_{bulk} = [(n-1)^2+k^2]/[(n+1)^2+k^2]$; vertical bar marks SC energy gap at 4.4 K.

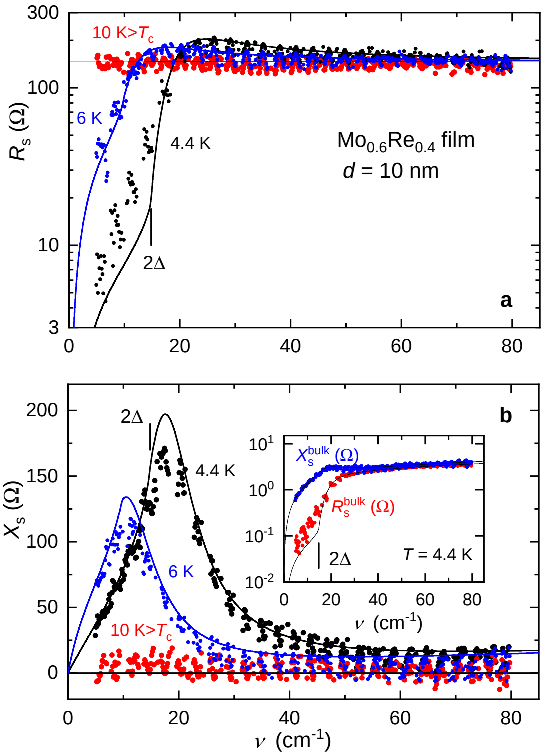

Figure 4. **a**, **b** – Frequency dependence of the real R_s (**a**) and the imaginary X_s (**b**) parts of the surface impedance $Z_s = R_s + iX_s = (\sigma^* d)^{-1} = \sigma'/[d(\sigma'^2+\sigma''^2)] + i\sigma''/[d(\sigma'^2+\sigma''^2)]$ of 10 nm-thick $Mo_{0.6}Re_{0.4}$ film on silicon substrate measured at temperatures above and below T_c; $\sigma^* = \sigma' + i\sigma''$ is the complex conductivity. Solid lines are the least-square fits with BCS expressions.[40] Inset in panel **b** shows R_s and X_s spectra of bulk material calculated using the formulas $R_s = Z_0 n/(n^2+k^2)$, and $X_s = Z_0 k/(n^2+k^2)$, where $Z_0 = 376.7\,\Omega$. In normal state $|R_s| \approx |X_s|$, as expected in the low-frequency limit ($\nu \ll \gamma$) of the Drude conductivity model;[36] at $T < T_c$ both quantities strongly decrease.[48] Vertical bar marks SC energy gap at 4.4 K.

the studied $Mo_{0.6}Re_{0.4}$ films, we present in figure 4 the spectra of the real R_s and imaginary X_s parts of surface impedance $Z_s = R_s + iX_s$. For a thin film, it reads $Z_s = (\sigma^* d)^{-1} = \sigma'[d(\sigma'^2+\sigma''^2)]^{-1} + i\sigma''[d(\sigma'^2+\sigma''^2)]^{-1}$, where $\sigma^* = \sigma' + i\sigma''$ is the complex-valued conductivity of the film material. At $T > T_c$ we observe dispersionless dependences R_s and $X_s \approx 0$ on the wavenumber, as expected for a good conductor.[37,47] In the SC state, the real impedance R_s (related to absorption) is strongly suppressed, while the frequency dependence of X_s has a broad maximum around the doubled gap frequency. These findings are typical fingerprints of a superconducting response.[48]

Although MoRe compounds are considered as two-band superconductors,[9,10] we do not observe any corresponding feature in the measured THz spectra (figures 2–4, as well as figures S1 and S2). The reason might be that the contribution to the electrodynamic response of one of the bands considerably exceeds the contribution of the other band. Thus, in order to model the experimental spectra, we used the BCS expressions derived for a single-band superconductor.[40] The fitting results shown by the solid lines in figures 2–4, S1–S2 describe the experimental spectra quite well. From figure 2b we see that the measured conductivity values are slightly above the BCS results, indicating extra below-gap absorption that may be due to bulk and/or surface defects. The performed fitting of the spectra allows us to determine temperature dependences of characteristics of the SC condensate – namely, the plasma frequency ν_{pl}^{SC}, the London penetration depth $\lambda_L = 1/(2\pi\nu_{pl}^{SC})$, the normalised superfluid density $1/\lambda_L^2$ and the energy gap (figure 5). The temperature dependences of ν_{pl}^{SC}, λ_L and $1/\lambda_L^2$ are in agreement with the expressions of two-fluid superconductivity model:[47]

$$\nu_{pl}^{SC}(T) = \nu_{pl}^{SC}(0)\sqrt{1-(T/T_c)^4}, \tag{2}$$

$$\lambda_L(T) = \frac{\lambda_L(0)}{\sqrt{1-(T/T_c)^4}}, \tag{3}$$

The temperature dependences of the gap energy values for the MoRe films of different thicknesses are well described by the BCS-like empirical expression[49]

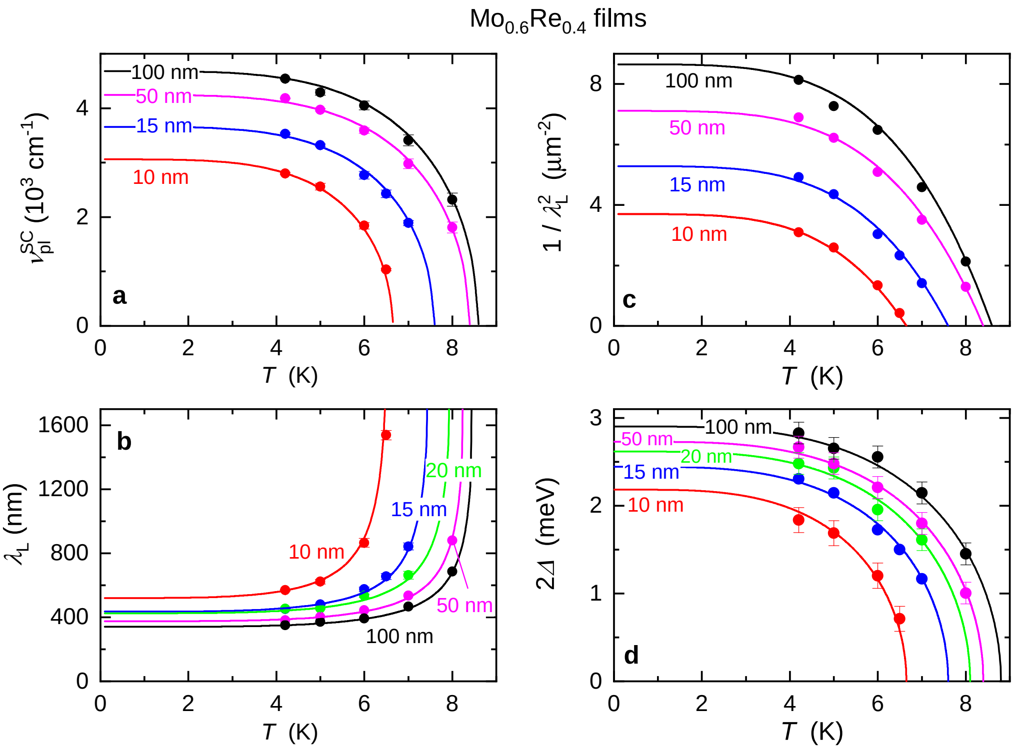

Figure 5. **a**, **b**, **c** – Temperature dependences of the plasma frequency of superconducting condensate ν_{pl}^{SC} (**a**), the London penetration depth λ_L (**b**), and the normalized superfluid density $1/\lambda_L^2$ (**c**) for the MoRe films of various thicknesses. Lines show least-square fits using expressions of the phenomenological Gorter-Cazimir two-fluid model of superconductivity,[47] corresponding expressions (2) and (3) are given in the text. **d** – Temperature dependences of the superconducting energy gap values for $\mathrm{Mo}_{0.6}\mathrm{Re}_{0.4}$ films of different thicknesses. Solid lines show the least-square fits with the empirical expression[49] (4).

$$2\Delta(T) \simeq 2\Delta(0)\,\tanh\left\{1.82\left[1.081\left(\frac{T_c}{T}-1\right)\right]^{0.51}\right\}. \quad (4)$$

In the above expressions (2)–(4) $\nu_{pl}^{SC}(0)$, $\lambda_L(0)$, and $2\Delta(0)$ represent zero-temperature values of the corresponding quantities. The doubled SC gap values obtained for all films are below 3 meV, so that the corresponding gap frequencies $2\Delta(0)/hc < 24\,\mathrm{cm}^{-1}$ are smaller than the estimated scattering rate $\gamma \approx 120$ cm^{-1}. This means that we deal with the dirty-limit superconductivity for all tested MoRe films.

Earlier, it was shown[9] that the superfluid density in $\mathrm{Mo}_{0.6}\mathrm{Re}_{0.4}$ polycrystalline samples cannot be explained within the framework of a single-band approach, since they show clear deviation from single-band behavior at low temperatures 2-6 K. Those data were described considering a two-band approach with the energy gaps $2\Delta_1 = 3.9$ meV and $2\Delta_2 = 1$ meV. The gap value $2\Delta(0) = 2.9$ meV obtained in our experiment for the thickest (100 nm) film falls between $2\Delta_1$ and $2\Delta_2$.

Thickness dependence of THz characteristics of $\mathrm{Mo}_{0.6}\mathrm{Re}_{0.4}$ films in superconducting state. Figure 6 presents the dependences of the penetration depth $\lambda_L(0)$, the critical temperature T_c and the SC gap energy $2\Delta(0)$ on the thickness d of the MoRe films. The reduction of the film thickness leads to an increase of the penetration depth and the decrease in both the critical temperature and zero-temperature energy gap. The ratio $2\Delta(0)/k_BT_c = 3.8 \pm 0.2$ is slightly higher than the standard BCS value 3.52 for weak-coupling regime, and this indicates moderately strong electron-phonon coupling in the MoRe films (k_B is the Boltzmann constant). By fitting the experimental dependence of $\lambda_L(0)$ on d using the expression[50]

$$\lambda_L(d) = 0.62\,\lambda_0\sqrt{\frac{\xi_0}{l(d)}}, \quad (5)$$

which is valid in the dirty limit, we are able to estimate the bulk BCS coherence length $\xi_0 = 26$ nm; λ_0 corresponds to the bulk penetration depth. The result of the fitting is shown in figure 6a by solid line. Taking $2\Delta(0) = 3$ meV as typical energy gap for bulk material (according to figure 6c) and the Fermi velocity[14] $v_F = 2.34 \cdot 10^7$ cm/s and using well-known expression[50] $\xi_0 = \hbar v_F/(\pi\Delta)$, we get the value of the BCS coherence length $\xi_0 \approx 33$ nm that is close to the above estimate $\xi_0 = 26$ nm. It makes possible to estimate the Ginsburg-Landau parameter $\kappa = \lambda_L/\xi \sim 10$, indicating type-II superconductivity in MoRe films. Using the dirty-limit expression[50]

$$\xi(d) = 0.855\sqrt{\xi_0 l(d)}, \quad (6)$$

we can evaluate the dependence of the coherence length

ξ on film thickness. The result is shown in the inset of figure 6a together with the thickness dependence of the mean free path l. For all films, we have $\xi(d) > l(d)$, what again confirms the dirty-limit SC. Smallness of the coherence length ξ and the mean free path ℓ with respect to both the penetration depth in normal state $\delta = (2\pi k\nu)^{-1}$ and in SC state λ_L (see insets in figures 2c, S1c, and 5b) means that the local approach holds in the normal and SC states of the studied $\mathrm{Mo_{0.6}Re_{0.4}}$ films.

Let us consider the suppression of superconductivity in thin films that is accompanied by a reduction of both the critical temperature and the energy gap. Since $\mathrm{Mo_{0.6}Re_{0.4}}$ films are binary alloy, such suppression could be due to disorder. Maekawa and Fukuyama[51] were the first to analyze the suppression caused by Cooper pairs localization in disordered thin films leading to an enhanced Coulomb repulsion and suppressed electronic density of states. They obtained the following expression

$$\ln\left(\frac{T_c}{T_c^{bulk}}\right) = -\frac{1}{2}\frac{(g_1-3g')N(0)e^2R_\square}{2\pi^2\hbar}\left[\ln\left(5.5\frac{\xi_0}{l}\frac{T_c^{bulk}}{T_c}\right)\right]^2 - \frac{1}{3}\frac{(g_1+g')N(0)e^2R_\square}{2\pi^2\hbar}\left[\ln\left(5.5\frac{\xi_0}{l}\frac{T_c^{bulk}}{T_c}\right)\right]^3, \tag{7}$$

where $g' < 0$ stands for the attractive interaction responsible for Cooper pair formation, $g_1 > 0$ characterizes Coulomb repulsion, $N(0)$ is the electronic density of states at the Fermi level per spin, $R_\square$ is the sheet resistance, and T_c^{bulk} is the critical temperature of bulk sample. The expression (7) with the parameters $g' = -0.2$ and $g_1 = 7$ describes the experimental $T_c(d)$ data quite well (dashed line in figure 6b), but the value $g_1 = 7$ seems to be too large as compared with $g_1 \sim 1$, considered in Maekawa and Fukuyama's paper.

Alternatively, we can use the theory of Finkel'shtein[52] based on the renormalization group approach and leading to the following expression

$$\frac{T_c}{T_c^{bulk}} = e^{-1/\gamma}\left[\frac{1+\sqrt{t/2}/(\gamma-t/4)}{1-\sqrt{t/2}/(\gamma-t/4)}\right]^{1/\sqrt{2t}}, \tag{8}$$

where $t = e^2R_\square/(2\pi^2\hbar)$, $\gamma = 1/\log(T_c^{bulk}\tau)$, and τ is the transit time. Taking the Fermi velocity $v_F = 2.34 \times 10^7$ cm/s[14] and thickness-dependent mean free path (see inset of figure 6a), we conclude that the expression (8) cannot reproduce our experimental data (see red line in the inset of figure 6b), since we should consider unreasonably short bulk mean free path, $l_0 = 0.56$ Å (see blue line in the inset of figure 6b).

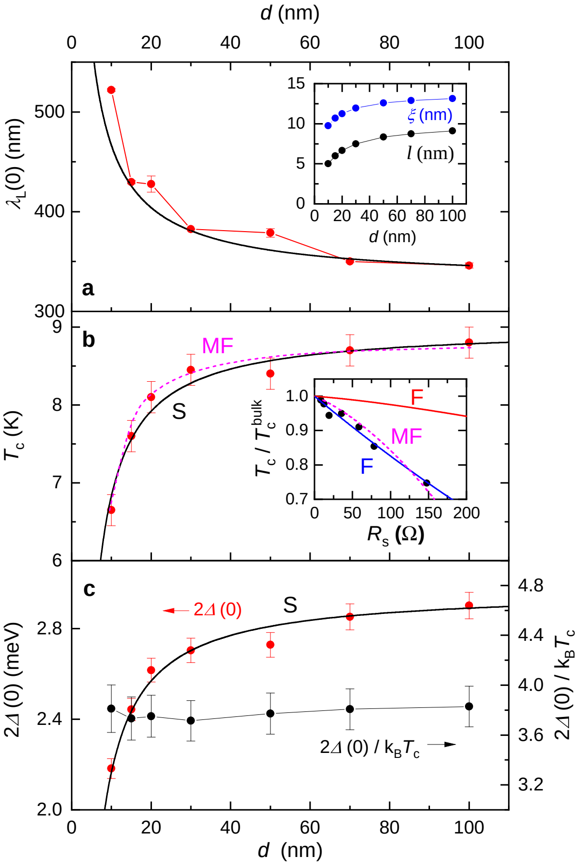

Figure 6. **a**, **b**, **c** – Thickness dependence of the zero-temperature London penetration depth $\lambda_L(0)$ (**a**), the critical temperature (**b**), the superconducting energy gap $2\Delta(0)$ and the ratio $2\Delta(0)/k_BT_c$ (**c**) for $\mathrm{Mo_{0.6}Re_{0.4}}$ films. Solid line in panel **a** is the least-square fit according to Eq. (5). In panel **b** the dashed line (labelled MF) is a result of calculation according to the expression (7) taken from Maekawa and Fukuyama's paper,[51] and solid line (labelled S) corresponds to the least-square fit with the expression (9) taken from Simonin's paper.[53] In panel **c** the solid line (S) shows a fit with $2\Delta(d) \sim (1 - \mathrm{const}/d)$, see Eq. (9). Inset in panel **a**: thickness-dependent coherence length and electron mean free path. Inset in panel **b**: dots – the dependence of the critical temperature of $\mathrm{Mo_{0.6}Re_{0.4}}$ films on their surface resistance; dashed line (MF) – least-square fit with expression (7); blue line (labelled F) – fit according to the expression (8) taken from Finkel'shtein's paper[52] ($v_F = 2.34 \cdot 10^7$ cm/s and $l_0 = 0.56$ Å); red line (F) – calculation using the expression (8) with the same parameters as before, but with the thickness-dependent mean free path, see inset in panel **a**.

Following the paper of Simonin[53] we consider a surface contribution[‡] to the Ginzburg-Landau free energy functional that leads to decrease in the density of states near the surface. This effect becomes significant in thin films where the surface-to-volume ratio is dominant. The theory of Simonin predicts the following dependence

$$T_c(d) = T_c^{bulk}\left(1 - \frac{d_c}{d}\right), \tag{9}$$

where $d_c = 2a/N(0)V$ is the critical thickness, corresponding to $T_c = 0$, a is the Thomas-Fermi screening length that is of the order of lattice parameter, V is the interaction potential, and $N(0)V$ is the bulk interaction potential. The expression (9) describes well the experimental data with the ratio $2a/N(0)V = 1.2$ nm (solid line in figure 6b). Taking $a \approx 0.3$ nm for $\mathrm{Mo_{0.6}Re_{0.4}}$, we

---

[‡] The author adds the term proportional to an integral $\int_S \psi^2 ds$ over the surface of a superconductor into the free-energy functional, where ψ is the normalized order parameter. This leads to the modification of the boundary conditions and results in the suppression of T_c.

obtain a quite reasonable value for the interaction potential $N(0)V \approx 0.5$. This allows us to conclude that the reduction of the order parameter near the surfaces of SC films can be considered as a more appropriate mechanism of suppression of superconductivity in the studied films. We note that similar results have been obtained for pure molybdenum films.[54]

According to figure 6c, the ratio $2\Delta/k_BT_c = 3.8 \pm 0.2$ seems to be thickness-independent, suggesting that the critical temperature depends on the film thickness in the same way as the energy gap. This is demonstrated by a fit of the experimental dependence $2\Delta(d)$ with an expression $2\Delta(d) \sim (1 - \text{const}/d)$ that is similar to Eq. (9). We thus suggest that the suppression of both the critical temperature and the SC energy gap are governed by the same mechanism – the alteration of the boundary conditions caused by the surface term introduced in the GL functional, resulting in change of the interaction potential $N(0)V$.

Conclusion

The first systematic studies of terahertz electrodynamic properties of $\mathrm{Mo_{0.6}Re_{0.4}}$ films of thicknesses ranging from 10 to 100 nm and corresponding critical temperatures from 6.5 to 9.5 K are performed at frequencies $0.15 - 2.4$ THz and in the temperature interval $T = 5 - 300$ K. The spectra of conductivity and permittivity are described within the BCS single-band approach. The obtained ratio $2\Delta(0)/k_BT_c = 3.8 \pm 0.2$ slightly exceeds the BCS value 3.52, demonstrating moderately strong electron-phonon coupling. The temperature dependencies of the superconducting energy gap, the penetration depth, the superconducting condensate plasma frequency and the normalized superfluid density are reproduced within the two-fluid superconductivity model. A strong decrease in the critical temperature and the energy gap in thin MoRe films is associated with the suppression of the mean superconducting order parameter due to a decrease in the local electronic density of states in MoRe films near their surfaces. Although our thinnest films have slightly smaller values of the critical temperature than those obtained earlier,[28] the values $T_c(d)$ are still higher than the critical temperatures of the alloys[30] MoSi, MoGe, WSi, NbSi, mentioned in the Introduction section. This makes MoRe alloy a perspective material for the design of elements and devices of advanced electronics and optoelectronics, for example, single-photon detectors, high-Q resonators for frequency locking systems (see figure S3), etc.

Acknowledgements

This work was supported by RSF 23-72-30004 (terahertz experiments and data analysis). Magnetron sputtering fabrication supported by the Ministry of Science and Higher Education of the Russian Federation (No. FSMG-2022-0014).

Supporting information and data availability

The Supporting Information is available free of charge at https://jmsn.colab.ws/publications/01-01002/supporting-file.

The data that support the findings of this study are available from the corresponding authors upon request.

Contact information

Corresponding author: Boris M. Nekrasov, orcid.org/0000-0003-3324-2893, e-mail nekrasov.bm@phystech.edu.

Corresponding author: Vasily S. Stolyarov, orcid.org/0000-0002-5317-0818, e-mail stolyarov.vs@phystech.edu.

Author contribution

Elena S. Zhukova, Alexander V. Melentev and Lenar S. Kadyrov carried out the THz experiments, spectra processing and data analysis. Boris M. Nekrasov, Anton S. Shaimardanov, Andrey G. Shishkin, Aleksander A. Golubov, Mikhail Yu. Kupriyanov performed data analysis, Boris P. Gorshunov and Vasily S. Stolyarov conceived and supervised the work. All authors contributed to the manuscript.

Competing Interests

The authors declare no competing financial or non-financial interests.

References

[1] Testardi L. R., Hauser J. J., Read M. H. *Enhanced superconducting T_c and structural transformation in Mo-Re alloys.*. Solid State Commun., vol. **9**, 1829-1831 (1971).

[2] Gavaler J. R., Janocko M. A., Jones C. K. *A-15 structure Mo-Re superconductor.* Appl. Phys. Lett., vol. **21**, 179-180 (1972).

[3] Postnikov V. S., Postnikov V. V., Zheleznyi V. S. *Superconductivity in Mo-Re system alloy films produced by electron beam evaporation in high vacuum.* Physica Status Solidi (a), vol. 39, K21-K23 (1977).

[4] Gavaler J. R., Janocko M. A., Jones C. K. *Superconductivity and Metastability in Alloys of the Mo-Re System.* In: Timmerhaus, K. D., O'Sullivan, W. J., Hammel, E. F. (eds) Low Temperature Physics–LT 13. Springer, Boston, MA (USA), 558-562 (1974).

[5] Vonsovsky S. V., Izyumov Y. A., Kurmaev E. Z. *Superconductivity of transition metals: their alloys and compounds.* Springer Series in Solid-State Sciences, vol. **27** (1982).

[6] Faley M. I., Reith P., Satrya C. D., Stolyarov V. S., Folkers B., Golubov A. A., Hilgenkamp H., Dunin-Borkowski R. E. *MoRe/YBCO Josephson junctions and π-loops.* Superconductor Sci. Technol., vol. **33**, 044005 (2020).

[7] Amet F., Ke C. T., Borzenets I. V., Wang J., Watanabe K., Taniguchi T., Deacon R. S., Yamamoto M., Bomze Y., Tarucha S., Finkelstein G. *Supercurrent in the quantum Hall regime.* Science, vol. **352**, 966-969 (2016).

[8] Calado V. E., Goswami S., Nanda G., Diez M., Akhmerov A. R., Watanabe K., Taniguchi T., Klapwijk T. M., Vandersypen L. M. K. *Ballistic Josephson junctions in edge-contacted graphene.* Nature Nanotechnology, vol. **10**, 761-764 (2015).

[9] Sundar, S., Sharath Chandra, L. S., Chattopadhyay, M. K., Roy, S. B. *Evidence of multiband superconductivity in the $\beta-$phase $Mo_{1-x}Re_x$ alloys.* J. Phys.: Condens. Matt., vol. **27**, 045701 (2015).

[10] Tarenkov V., Shapovalov A., Boliasova O., Belogolovskii M., Kordyuk A. *Two-band superconductivity in a Mo-Re alloy with an equal concentration of the components.* Low Temp. Phys., vol. **47**, 101-105 (2021).

[11] Gornostyrev Y. N., Katsnelson M. I., Peschanskikh G. V., Trefilov A. V. *On the Nature of the Rhenium Effect. Peculiarities of the Band Structure and Elastic Moduli of W-and Mo-Based Alloys.* Physica Status Solidi (b), vol. **164**, 185-193 (1991).

[12] Okada M., Rotenberg E., Kevan S. D., Schäfer J., Ujfalussy B., Stocks G. M., Genatempo B., Bruno E., Plummer E. W. *Evolution of the electronic structure in $Mo_{1-x}Re_x$ alloys.* New J. Phys., vol. **15**, 093010 (2013).

[13] Tarenkov V., Shapovalov A., Zhitlukhina E., Belogolovskii M., Seidel P. *Mo-Re alloy: A new benchmark two-band superconductor.* Low Temp. Phys., vol. **49**, 103-107 (2023).

[14] Shang T., Baines C., Chang L., Gawryluk D. J., Pomjakushina E., Shi M., Medarde M., Shiroka T. *$Re_{1-x}Mo_x$ as an ideal test case of time-reversal symmetry breaking in unconventional superconductors.* npj Quantum Materials, vol. **5**, 76 (2020).

[15] Seleznev V. A., Tarkhov M. A., Voronov B. M., Milostnaya I. I., Lyakhno V. Y., Garbuz A. S., Mikhailov M. Y., Zhigalina O. M., Gol'tsman G. N. *Deposition and characterization of few-nanometers-thick superconducting Mo-Re films.* Supercond. Sci. Technol., vol. **21**, 115006 (2008).

[16] Sundar S., Sharath Chandra L. S., Sharma V. K., Chattopadhyay M. K., Roy S. B. *Electrical transport and magnetic properties of superconducting $Mo_{52}Re_{48}$ alloy.* AIP Conf. Proc., vol. **1512**, 1092-1093 (2013).

[17] Mohsin A., David C. H., Saverio R. 1 *Molybdenum-rhenium superconducting suspended nanostructures.* Appl. Phys. Lett., vol. **104**, 233102 (2014).

[18] Andreone A., Baldini A., Borchi E., Del Carmine P., Di Chiara A., Mandò P. A., Persico V. *Radiation hardness of $Mo_{60}Re_{40}$ superconducting thin films.* Nucl. Phys. B – Proc. Suppl., vol. **44**, 688-692 (1995).

[19] Schneider B. H., Etaki S., van der Zant H. S., Steele G. A. *Coupling carbon nanotube mechanics to a superconducting circuit.* Sci. Rep., vol. **2**, 599 (2012).

[20] Shishkin A. G., Skryabina O. V., Gurtovoi V. L., Dizhur S. E., Faley M. I., Golubov A. A., Stolyarov V. S. *Planar MoRe-based direct current nanoSQUID.* Supercond. Sci. Technol., vol. **33**, 065005 (2020).

[21] Schmidt F. E., Jenkins M. D., Watanabe K., Taniguchi T., Steele G. A. *A ballistic graphene superconducting microwave circuit.* Nature Commun., vol. **9**, 4069 (2018).

[22] Yu C. G., Kim B., Doh Y.-J. *Fabrication and characterization of magnetic-field-resilient MoRe superconducting coplanar waveguide resonators.* Curr. Appl. Phys., vol. **47**, 24–29 (2023).

[23] Ranjan V., de Lange G., Schutjens R., Debelhoir T., Groen J. P., Szombati D., Thoen D. J., Klapwijk T. M., Hanson R., DiCarlo L. *Probing dynamics of an electron-spin ensemble via a superconducting resonator.* Curr. Appl. Phys., vol. **47**, 24-29 (2023).

[24] Amsüss R., Koller C., Nöbauer T., Putz S., Rotter S., Sandner K., Schneider S., Schramböck M., Steinhauser G., Ritsch H., Schmiedmayer J., Majer J. *Cavity QED with Magnetically Coupled Collective Spin States.* Phys. Rev. Lett., vol. **107**, 060502 (2011).

[25] Wang J. I., Rodan-Legrain D., Bretheau L., Campbell D. L., Kannan B., Kim D., Kjaergaard M., Krantz P., Samach G. O., Yan F., Yoder J. L., Watanabe K., Taniguchi T., Orlando T. P., Gustavsson S., Jarillo-Herrero P., Oliver W. D. *Coherent control of a hybrid superconducting circuit made with graphene-based van der Waals heterostructures.* Nature Nanotechnology, vol. **14**, 120-125 (2019).

[26] Borjans F., Croot X. G., Mi X., Gullans M. J., Petta J. R. *Resonant microwave-mediated interactions between distant electron spins.*, Nature, vol. **577**, 195-198 (2020).

[27] Banszerus L., Hecker K., Möller S., Icking E., Watanabe K., Taniguchi T., Volk C., Stampfer C. *Spin relaxation in a single-electron graphene quantum dot.* Nature Commun., vol. **13**, 3637 (2022).

[28] Milostnaya I., Korneev A., Tarkhov M., Divochiy A., Minaeva O., Seleznev V., Kaurova N., Voronov B., Okunev O., Chulkova G., Smirnov K., Gol'tsman G. *Superconducting single photon nanowire detectors development for IR and THz applications.* J. Low Temp. Phys., vol. **151**, 591-596 (2008).

[29] Beck M., Klammer M., Lang S., Leiderer P., Kabanov V. V., Gol'tsman G. N., Demsar J. *Energy-gap dynamics of superconducting NbN thin films studied by time-resolved terahertz spectroscopy.* Phys. Rev. Lett., vol. **107**, 177007 (2011).

[30] Banerjee A., Baker L. J., Doye A., Nord M., Heath R. M., Erotokritou K., Bosworth D., Barber Z. H., MacLaren I., Hadfield R. H. *Characterisation of amorphous molybdenum silicide (MoSi) superconducting thin films and nanowires.* Supercond. Sci. Technol., vol. **30**, 084010 (2017).

[31] Born M., Wolf E., Bhatia A. B. *Principles of Optics: Electromagnetic Theory of Propagation, Interference and Diffraction of Light.* 6^{th} ed., Cambridge University Press (1980).

[32] Anzin V. B., Gorshunov B. P., Kozlov G. V., Volkov A. A., Lebedev S. P., Fedorov I. V., Schutzmann J., Renk K. F. *Measurement of electrodynamic parameters of superconducting films in far-infrared and submillimeter frequency ranges.* Appl. Supercond., vol. **1**, 467-478 (1993).

[33] Gorshunov B. P., Kozlov G. V., Volkov A. A., Lebedev S. P., Fedorov I. V., Prokhorov A. M., Makhov V. I., Schützmann J., Renk, K. F. *Measurement of electrodynamic parameters of superconducting films in the far-infrared and submillimeter frequency ranges.* Int. J. Infrared Milli Waves, vol. **14**, 683-702 (1993).

[34] Makise K., Mizokami Y., Nogami T., Sawada G., Asano T., Shinozaki B., Ichikawa F. *Estimations of superconducting fluctuation effects in amorphous MoRu and MoRe alloy thin films*, Mater. Res. Expr., vol. **5**, 096406 (2018).

[35] Mayadas A. F., Shatzkes M. *Electrical-resistivity model for polycrystalline films: the case of arbitrary reflection at external surfaces.*, Phys. Rev. B, vol. **1**, 1382 (1970).

[36] Sokolov A. V. *Optical Properties of Metals.* American Elsevier Publishing Company (1967).

[37] Dressel M., Grüner G. *Electrodynamics of Solids: Optical Properties of Electrons in Matter.* Cambridge University Press (2002).

[38] Sondheimer E. H. *The mean free path of electrons in metals.* Adv. Phys, vol. **50**, 499-537 (2001).

[39] Kittel C. *Introduction to Solid State Physics.* 8^{th} ed., Wiley (2004).

[40] Zimmermann W., Brandt E. H., Bauer M., Seider E., Genzel L. *Optical conductivity of BCS superconductors with arbitrary purity.* Physica C: Supercond., vol. **183**, 99-104 (1991).

[41] Glover III R. E., Tinkham M. *Conductivity of Superconducting Films for Photon Energies between 0.3 and 40* kT_c. Phys. Rev., vol. **108**, 243 (1957).

[42] Palmer L. H., Tinkham M. *Far-Infrared Absorption in Thin Superconducting Lead Films.* Phys. Rev., vol. **165**, 588-595 (1968).

[43] Ginsberg D. M., Tinkham M. *Far Infrared Transmission through Superconducting Films.* Phys. Rev., vol. **118**, 990-1000 (1960).

[44] Richards P. L., Tinkham M. *Far-Infrared Energy Gap Measurements in Bulk Superconducting In, Sn, Hg, Ta, V, Pb, and Nb.* Phys. Rev., vol. **119**, 575-590 (1960).

[45] Tinkham M. *Introduction to Superconductivity.*, 2^{nd} ed., McGraw Hill (1996).

[46] Gorshunov B. P., Volkov A. A., Prokhorov A. S., Spektor I. E. *Methods of terahertz-subterahertz BWO spectroscopy of conducting materials.* Phys. Solid State, vol. **50**, 2001-2012 (2008).

[47] Van Duzer T., Turner C. W. *Principles of superconductive devices and circuits.* 2^{nd} ed., Prentice Hall (1999).

[48] Miller P. B. *Surface impedance of superconductors.* Phys. Rev., vol. **118**, 928 (1960).

[49] Carrington A., Manzano F. *Magnetic penetration depth of* MgB_2. Physica C: Superconductivity, vol. 385, 205-214 (2003).

[50] De Gennes P. G. *Superconductivity of metals and alloys.* CRC press (2019).

[51] Maekawa S., Fukuyama H. *Localization effects in two-dimensional superconductors.* J. Phys. Soc. Japan, vol. **51**, 1380-1385 (1982).

[52] Finkel'shtein A. M. *Superconducting transition temperature in amorphous films.* JETP Lett., vol. **45**, 37-40 (1987); World Scientific Series in 20th Century Physics, vol. **11**, 288-291 (1996).

[53] Simonin J. *Surface term in the superconductive Ginzburg-Landau free energy: Application to thin films.* Phys. Rev. B, vol. **33**, 7830 (1986).

[54] Fàbrega L., Camón A., Fernández-Martínez I., Sesé J., Parra-Borderías M., Gil O., González-Arrabal R., Costa-Krümer J. L., Briones F. *Size and dimensionality effects in superconducting Mo thin films.* Supercond. Sci. Technol., vol. **24**, 075014 (1911).

Publisher's note: We encourage readers to explore the guiding philosophy of the Journal of Mesoscience & Nanotechnology [V. Stolyarov, Mesosci. Nanotechnol., vol. 1, 01001 (2023)] and consider submitting their work for potential publication in our journal.

DOI: 10.64214/jmsn.01.01003 **Article**

Thouless energy in Josephson SN-N-NS bridges

S. V. Bakurskiy,[1,2] V. I. Ruzhickiy,[1,2] A. A. Neilo,[1] N. V. Klenov,[2,3] I. I. Soloviev,[1,2] A. A. Elistratova,[2,4]
A. G. Shishkin,[2,4] V. S. Stolyarov[2,4] and M. Yu. Kupriyanov[1]

[1] *Skobeltsyn Institute of Nuclear Physics, Lomonosov Moscow State University, Moscow 119991, Russia*
[2] *Dukhov All-Russia Research Institute of Automatics, Moscow 101000, Russia*
[3] *Faculty of Physics, Lomonosov Moscow State University, Moscow 119992, Russia*
[4] *Center for Advanced Mesoscience and Nanotechnology, Moscow Institute of Physics and Technology, Dolgoprudny 141700, Russia*

submitted 9 February 2024, accepted 20 June 2024, published 27 July 2024

We have studied the Thouless energy in Josephson superconductor – normal metal – superconductor (SN-N-NS) bridges analytically and numerically, considering the influence of the sub-electrode regions. We have discovered a significant suppression of the Thouless energy with increasing interfacial resistance, consistent with experimental results. The analysis of the temperature dependence of the critical current in Josephson junctions in comparison with the expressions for the Thouless energy may allow the determination of the interface parameters of S and N-layers.

Introduction

In recent years, there has been a reawakened interest in Josephson structures in which the weak coupling region exhibits a metallic type of conductivity.[1–11] These structures are anticipated to surpass the integration limitations faced by superconducting devices used in digital information processing. The steady-state properties of SNS Josephson sandwiches and superconductor/normal metal/superconductor SN-N-NS bridges have been intensively studied.[10–19]

In Ref.[12] assuming the fulfillment of rigid boundary conditions at the SN interfaces, it was shown that in the case when the distance L between the S-electrodes significantly exceeds the characteristic decay length of superconducting correlations in the N-layer $\xi = (D/2\pi T)^{1/2}$, the decay of the critical current I_c with increasing L depends significantly on the ratio between the operating temperature T and the critical temperature of the superconducting electrodes T_c (here D is the diffusion coefficient of an ordinary metal). At small temperature ($T \ll T_c$) there is a power dependence ($I_c \propto 1/L^2$). With increasing temperature, the dependence of I_c on L becomes exponential: $I_c \propto \exp(-L/\xi)$.

In Ref.[17] these studies were complemented by a more detailed analysis of the temperature dependence of the critical current at low temperatures $T \ll T_c$. Numerical calculations carried out in Ref.[17] allowed the authors to propose an approximation formula for I_c

$$\frac{eI_cR_n}{E_T} = \alpha\left(1-\beta\exp\left(-\frac{\alpha E_T}{3.2T}\right)\right), \quad E_T = \frac{D}{L^2}. \quad (1)$$

The fitting parameters $\alpha \approx 10.82$ and $\beta \approx 1/3$ correspond to the limit of small Thouless energy E_T as compared to the magnitude of the order parameter Δ in S-electrodes. In the opposite limit ($E_T \gg T$) the dependence $I_c(E_T)$ has the following form

$$\frac{eI_cR_n}{E_T} = \frac{32}{3+2\sqrt{2}}\left(\frac{2\pi T}{E_T}\right)^{3/2}\exp\left(-\sqrt{\frac{2\pi T}{E_T}}\right). \quad (2)$$

The publication of these results[17] stimulated the study of SNS-based structures aiming to experimentally determine the Thouless energy.[17,18,20–42] Experimental studies have shown that the values of the parameter α in the expression (1) obtained in Ref.[17] are at least several times larger than their experimental values. As a possible reason for this discrepancy, the presence of finite transparency of the SN boundaries of the studied Josephson contacts has been hypothesized. To account for this circumstance, a renormalization of the Thouless energy was proposed[18]

$$E_T^{\text{eff}} = E_T\frac{Ar^B}{C+r}, \quad \text{where} \quad r = \frac{G_N}{G_B}. \quad (3)$$

Here, r is normalization coefficient, G_N and G_B are the conductance of the normal wire and the SN interface, respectively, A, B, and C are fitting parameters. It is important to note that the authors of Ref.[18] "do not have a good explanation of the factor r^B and the numerical value of B" that they used to fit the data. Additionally, the fitting coefficients A, B, and C are not universal. Even for a set of samples differing by the distance L between the electrodes with fixed other parameters, all these coefficients will be sample-dependent.

It should be noted that almost all the experimental works cited above used the shadow mask technique to fabricate SNS-based Josephson contacts. The resulting hybrid structures had the SN-N-NS bridge geometry shown in figure 1. In this type of contact, the effective distance L_{eff} between the S-electrodes is not the geometric size L of the weak bonding region. This region is delocalized (in the other words, without rigid boundaries) and includes the areas of the N-film under the superconductors where current injection into the superconductor takes place. The presence of such delocalization was also qualitatively indicated by the experimental data. Indeed, substitution of the experimentally determined E_T into the expression (1) gave an estimate of the size of the weak coupling region, which is larger than L. In our opinion, there is a significant difference in the geometry of the SN and SN-NS interfaces that leads to an overestimation of the theoretical value of the Thouless energy calculated using rigid boundary conditions at the interface of the composite SN electrode with the N-film of the bridge. The purpose of this article is to perform a detailed analysis of the proximity effect between the SN electrode and the N-film of SN-N-NS bridge structures and to derive an expression for the Thouless energy that takes into account both the finite transparency of their SN boundaries and the delocalization of the weak link region.

Before that, it is first necessary to define what we mean by the Thouless energy in Eq. (1) in the considered SN-N-NS structures. According to the definition[43–46] E_T characterizes the sensitivity of the energy state of the system to a modification of boundary conditions. This correlates with the existing characteristic scale of spatial changes in the system's parameters with its geometric dimensions. Unfortunately, for SN-N-NS junctions the geometric size of the weak link region cannot be strictly determined. Moreover, a supercurrent across the junction is expressed by the sum of the terms combined by the Green's function over the Matsubara frequencies, therefore the characteristic scale of spatial variations in the N-film $\xi_\omega = (D/2\omega)^{1/2}$ depends on the Matsubara frequencies $\omega = \pi T(2n+1)$, where $n = 0, 1, 2 \ldots$ In the low-temperature range $T \ll T_c$ this sum converges at $\omega \approx \pi T_c$. Thus, there is wide range of parameters (L and ξ_ω) with some uncertainty in the choice of a single characteristic scale for spatial changes in the structure.

There is another interpretation of the Thouless energy. It suggests that two states whose energies differ by less than the Thouless energy are correlated. Otherwise, they can be considered as independent single-particle states whose energies are not shared. In our particular case, we are not dealing with the energy of states, but with a set of Green's functions which determine the supercurrent. The difference in the nature of the spatial changes in these functions is determined by the Matsubara frequency $\omega = \pi T(2n+1)$. Therefore, the interval at which the changes occur is equal to $2\pi T$.

In order to determine from a numerical solution of the Usadel equations or from experimental data the temperature T_{Th} for the transition from a sharp increase to a smooth character of the current change with decreasing temperature, we can introduce the Thouless energy for our problem as $E_T = 2\pi T_{Th}$. The Thouless energy determined in this way gives us the temperature at which the structural transitions from a discrete to an integral representation of its properties, such as the order parameter and the superconducting current (supercurrent), takes place.

It should be emphasized that the definition of $E_T = 2\pi T_{Th}$ is absolutely equivalent to the standard definition of E_{Th} in Eq. (1). By introducing the Thouless energy as described above, we can further use the relation (1) to estimate the characteristic scale of spatial variations in SNS structure as $L = (D/2\pi T_{Th})^{1/2} = \xi$ and thus find that L coincides with ξ_ω at the first Matsubara frequency $\omega = \pi T$ and $T = T_{Th} = E_T/2\pi$, that is, with the maximum value among the scales ξ_ω. In other words, the result of the above reasoning can be reformulated as follows: the Thouless energy is indeed defined by the expression (1). The value of the Thouless temperature $T_{Th} = E_T/2\pi$ required for processing of experimental data follows from the equality of the geometrical size of the structure with the maximum value of ξ_ω among the set of characteristic scales of the problem.

Thus, according to the established rule for the Thouless energy E_T in the considered planar SN-N-NS structures, we have to proceed from the equality of the scale ξ_ω to the effective geometric size of the weak coupling region $L + \zeta_\omega$

$$\xi_\omega = L + 2\kappa\zeta_\omega \tag{4}$$

at the first Matsubara frequency $\omega = E_T/2$. Here, ζ_ω is the maximum value among characteristic scales of spatial changes in the N-layer underneath the S-films and κ is a parameter that fixes the part of the effective coherence length ζ_ω by which the effective distance between the electrodes increases (formal definition of κ is given below). Note that at $\zeta_\omega = 0$ the expression (4) is transformed into the definition (1) of E_T, which was previously used to describe SNS sandwiches with rigid boundary conditions at the SN interfaces.

To determine ζ_ω it is sufficient to solve the problem on the proximity effect between a semi-infinite N-film and an extended SN electrode.

1 Proximity effect between extended SN electrode and semi-infinite N-film

We assume that the dirty-limit conditions are satisfied both in the superconductor and normal metal in the bridge, its SN boundaries have finite transparency, and the thickness of the N-film d_N is much less than $\xi_N = (D/2\pi T_c)^{1/2}$. The suppression of superconductivity in the S-film due to the proximity effect with the N-layer is considered negligible and it is not taken into account. Under these assumptions the proximity effect between the semi-infinite SN electrode (at $x \geq 0$) and the semi-infinite N-film (at $x \leq 0$) can be considered in the framework of the Usadel equations.[47] It was shown[48] that the Usadel equation for the θ function in the N-film under the S-electrode they can be written in the form

$$\zeta_\omega^2 \frac{\partial^2}{\partial x^2}\theta - \sin(\theta - \theta(\infty)) = 0,\ x \geq 0, \tag{5}$$

where

$$\theta(\infty) = \arctan\frac{\pi T_c \sin(\theta_S)}{\omega\gamma_{BM} + \pi T_c \cos(\theta_S)} \tag{6}$$

and

$$\cos(\theta_S) = \frac{\omega}{\sqrt{\omega^2+\Delta^2}},\ \sin(\theta_S) = \frac{\Delta}{\sqrt{\omega^2+\Delta^2}}, \tag{7}$$

$\gamma_{BM} = \gamma_B d/\xi_N$, $\gamma_B = R_B/\rho_N \xi_N$, R_B is the specific boundary resistance, Δ is the absolute value of the order

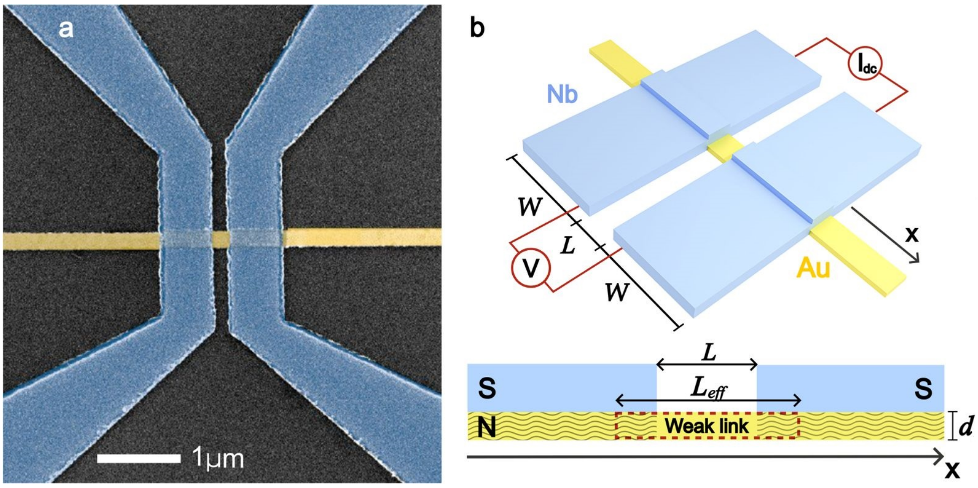

Figure 1. **a** – Scanning electron microscope image of an Nb/Au-Au-Au/Nb bridge with superconducting Nb electrodes and an Au weak link. **b** – Top part: three-dimensional sketch of the Josephson superconductor/normal metal/superconductor (SN-N-NS) bridge. The sample is connected using a four-point scheme. Bottom part: side view of the Josephson SN-N-NS bridge. Wavy lines indicate the proximized region of the N-layer under the S-electrode, and the red frame indicates the effective weak link.

parameter in the S layer, which has the BCS-like temperature dependence. We conclude that

$$\frac{\zeta_\omega}{\xi_\omega} = \sqrt{\frac{\omega\gamma_{BM}}{\sqrt{(\omega\gamma_{BM})^2 + 2\pi T_c\omega\gamma_{BM}\cos(\theta_S) + (\pi T_c)^2}}}. \quad (8)$$

The Usadel equation in the N-film can be written as follows

$$\xi_\omega^2 \frac{\partial^2}{\partial x^2}\theta - \sin\theta = 0, \quad x \leq 0. \quad (9)$$

The existence of the first integrals of the equations (5) and (9)

$$\zeta_\omega \frac{\partial}{\partial x}\theta = 2\sin\left(\frac{\theta(\infty) - \theta}{2}\right), \quad x \geq 0, \quad (10)$$

$$\xi_\omega \frac{\partial}{\partial x}\theta = 2\sin\frac{\theta}{2}, \quad x \leq 0, \quad (11)$$

permits to get their analytical solutions

$$\theta = \theta(\infty) + 4\arctan\left[Q\exp\left(-\frac{x}{\zeta_\omega}\right)\right], \quad x \geq 0, \quad (12)$$

$$\theta = 4\arctan\left[\left(\tan\frac{\theta(-0)}{4}\right)\exp\left(\frac{x}{\xi_\omega}\right)\right], \quad x \leq 0, \quad (13)$$

where

$$Q = \tan\frac{\theta(+0) - \theta(\infty)}{4}.$$

The integration constants $\theta(\pm 0)$ in Eqs. (12)–(13)

$$\theta(\pm 0) = 2\arctan\frac{\sin\frac{\theta(\infty)}{2}}{\cos\frac{\theta(\infty)}{2} + g}, \quad g = \frac{\xi_\omega}{\zeta_\omega}. \quad (14)$$

have been determined from the boundary conditions

$$\frac{\partial}{\partial x}\theta(+0) = \frac{\partial}{\partial x}\theta(-0) \quad \text{and} \quad \theta(+0) = \theta(-0) \quad (15)$$

at SN-N interface ($x = 0$).

2 Thouless energy

Substitution of Eq. (8) into Eq. (4) at the first Matsubara frequency $\omega = E_T/2$ results in

$$\frac{L}{\xi_N} + 2\kappa\sqrt{\frac{\gamma_{BM}}{\sqrt{\epsilon^2\left(\gamma_{BM}^2 + 2\gamma^*\gamma_{BM}\right) + 1}}} = \sqrt{\frac{1}{\epsilon}}, \quad (16)$$

where $\epsilon = E_T/2\pi T_c$, $\gamma^* \approx 1.781$ is Euler's constant. For simplicity we replace Δ with its value $\pi T_c/\gamma^*$ at $T \ll T_c$.

In the limit $\epsilon\gamma_{BM} \gg 1$ Eq. (16) transforms to

$$\epsilon = \frac{\xi_N^2}{L^2}\left(1 - 2\kappa\sqrt{\frac{\gamma_{BM}}{\sqrt{\gamma_{BM}^2 + 2\gamma^*\gamma_{BM}}}}\right)^2. \quad (17)$$

Note that as $\gamma_{BM} \to \infty$ the SN boundaries become completely non-transparent for quasiparticles in the N-region, therefore thequasiparticle current cannot flow from the N-film of the SNS contact into the S-electrodes. If the length of the SN boundaries of the composite SN electrodes of the SN-N-NS structure significantly exceeds ζ_ω, the length of the current localization region in its N-part can be considered infinite. Therefore, in full agreement with Eq. (1), the parameter ϵ should tends to zero, as $\gamma_{BM} \to \infty$. From this requirement we get $\kappa = 1/2$ and

$$\epsilon = \frac{\xi_N^2}{L^2}\left(1 - \sqrt{\frac{\gamma_{BM}}{\sqrt{\gamma_{BM}^2 + 2\gamma^*\gamma_{BM}}}}\right)^2. \quad (18)$$

Suppose further that the parameter κ is independent on γ_{BM} in the opposite limit $\epsilon\gamma_{BM} \ll 1$, then we get

$$\epsilon = \frac{\xi_N^2}{(L + \xi_N\sqrt{\gamma_{BM}})^2}. \quad (19)$$

Figures 2a,b show the dependence of the Thouless energy E_T on the suppression parameter γ_{BM}, calculated using equations (16), (17), and (19), for the distances between the electrodes SN-N-NS structures, which are

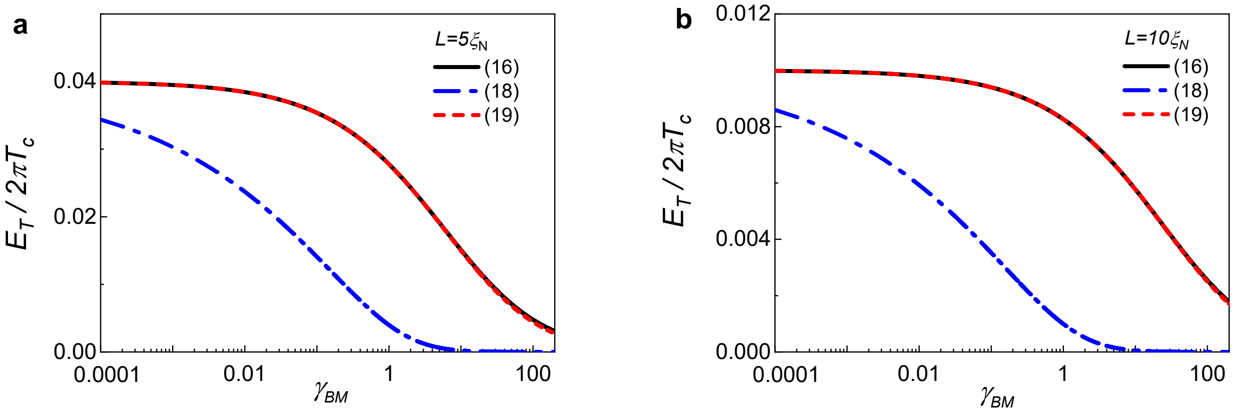

Figure 2. **a**, **b** – Thouless energy E_T versus interface parameter γ_{BM} in the SN-N-NS bridge with the distances between the electrodes $L = 5\xi_N$ (panel a) and $L = 10\xi_N$ (panel b), calculated from the Eq. (16) (solid line) and from the asymptotic expressions (18) (dash-dotted line) and (19) (dashed line), valid in the limit of $\epsilon\gamma_{BM} \gg 1$ and $\epsilon\gamma_{BM} \ll 1$, respectively.

$L = 5\xi_N$ and $L = 10\xi_N$. The calculations show that the approximation formula (19) coincides with the exact dependence $E_T(\gamma_{BM})$ calculated by the formula (16) within the specified range of parameters for long bridges. A noticeable discrepancy between the curves calculated by formulas (16) and (19) only appears in the $\gamma_{BM} \gg 100$ limit – this scenario is not realized in the experiments involving SN-N-NS structures.

At the same time, the expression (17) fits the exact dependency $E_T(\gamma_{BM})$ rather poorly. The reason is that the condition $\epsilon\gamma_{BM} \gg 1$ is not fulfilled even in the region of large γ_{BM}. This is due to the fact that ϵ decreases much faster than γ_{BM}^{-1}. The difference between the exact solution (16) and that resulting from asymptotic expression (17) becomes more obvious as L/ξ_N increases.

It is easy to see that when $L \gg \xi_N\sqrt{\gamma_{BM}}$ the expression (16) is reduced to Eq. (1). Physically, this limit is equivalent to the fulfillment of rigid boundary conditions at the N boundaries of the bridging film with its NS electrodes. In this limit, as in the SNS sandwiches investigated in Ref.[17] the rigid boundary conditions do not impose any additional characteristic lengths characterizing the spatial variations of parameters in the N film of SNS or SN-N-NS structures. The weak coupling region turns out to be a "closed" system, characterized only by its intrinsic parameters, such as the diffusion coefficient D. The Thouless energy (1) was introduced precisely for such "closed" systems.

Going beyond the rigid boundary conditions, such as considering the finite transparency of SN boundaries in SNS sandwiches or the delocalization of the weak coupling region in the studied SN-N-NS structures, violates the closure condition. Additional scales appear in the problems determined by the suppression parameter γ_B in SNS sandwiches or γ_{BM} in SN-N-NS structures. Therefore, in SN-N-NS bridges in accordance with the formula (16) at $L \ll \xi_N\sqrt{\gamma_{BM}}$ the diffusion coefficient no longer characterizes the system and the Thouless energy $E_T = \pi T_c/\gamma_{BM}$ in the first approximation is determined only by the parameter γ_{BM}, *i.e.*, by the properties of the SN boundaries.

The proposed implicit definition (16) of E_T is a compromise solution, considering both the internal parameters of the N-metal in the weak coupling region and the peculiarities of induced superconducting correlations in in the N-metal.

3 Calculation of a supercurrent across SN-N-NS junction

The dependence of the superconducting current density I on the phase difference of the order parameters of the superconducting electrodes φ in the SN-N-NS junctions has been previously calculated by numerically in Ref.[10] for arbitrary values of γ_{BM} and L/ξ_N. Just as in the approach we used earlier in Section II, the suppression of superconductivity in the S-film was not taken into account in Ref.[9] For computational convenience, the Usadel equations were written in the Φ representation (the origin of the $0x$ axis is placed in the center of the structure)

$$\xi_{\mathrm{eff}}^2 \frac{\partial}{\partial x}\left(G^2 \frac{\partial \Phi}{\partial x}\right) - \Phi = -\delta, \quad x \geq L/2; \tag{20}$$

$$\frac{\partial}{\partial x}\left(G^2 \frac{\partial \Phi}{\partial x}\right) - \Omega G \Phi = 0, \quad 0 \leq x \leq L/2; \tag{21}$$

$$\xi_{\mathrm{eff}}^2 = \frac{\gamma_{BM}}{G\left(G_s + \gamma_{BM}\Omega\right)}, \qquad \delta = \frac{G_s \Delta \exp(i\varphi/2)}{\left(G_s + \gamma_{BM}\Omega\right)}; \tag{22}$$

$$\frac{I}{I_0} = \frac{2\pi T}{T_c} \sum_{\Omega \geq 0}^{\infty} \frac{G^2}{\Omega^2}\left(\operatorname{Im}\Phi \frac{\partial \operatorname{Re}\Phi}{\partial x} - \operatorname{Re}\Phi \frac{\partial \operatorname{Im}\Phi}{\partial x}\right). \tag{23}$$

Here, Φ and $G = \Omega/(\Omega^2 + \Phi\Phi^*)^{1/2}$ are Usadel Green's functions, the Matsubara frequencies $\Omega = (2n+1)T/T_c$ are normalized on πT_c, the x-coordinate is normalized on ξ_N, and $I_0 = T_c/e\xi_n\rho_N$, where ρ_N is residual resistivity of the N-film. The modulus of the order parameter in the S-electrode Δ has the BCS-like temperature dependence and it is normalized on πT_c; $\varphi/2$ is the phase of the order parameter for the right electrode ($x \gtrsim L/2$).

Equations (20) and (21) should be supplemented by appropriate boundary conditions. At $x = 0$ these conditions follow from the symmetry of the considered problem

$$\frac{\partial \operatorname{Re}\Phi}{\partial x} = 0 \quad \text{and} \quad \operatorname{Im}\Phi = 0. \tag{24}$$

At a large distance from the N-NS boundary, the function Φ converges to a solution that is independent of x

$$\Phi = \delta. \tag{25}$$

Figures 3a,b show the $I_c(T)$ dependences calculated for $L = 5\xi_N$ and for various interface parameters γ_{BM} ranging from 0.01 to 100. For convenience, they are presented in linear and logarithmic scales. The points on these curves ($\circ$) correspond to the halfed Thouless energy ($T/T_c = E_T/2$). The E_T values are calculated for $L = 5\xi_N$ and various γ_{BM} using Eq. (19). These figures clearly show that in the vicinity of $E_T/2$ the slope of the dependences $I_c(T)$ changes, *i.e.*, there is a transition from a smooth to a sharp temperature drop of $I_c(T)$ with increasing temperature (see figures 3a,b).

In addition to the temperature $T = E_T/2$, two other characteristic temperature values can be noted. They are $T = T_{Th} = E_T/2\pi$ marked with squares and $T = E_T$ marked with triangles on the temperature dependences of the first derivative of the critical current with respect to temperature (see figures 3c-f). Figures 3d,f clearly show that for $L = 5\xi_N$ and $\gamma_{BM} = 0.01$ the Thouless temperature is $T_{Th} \approx 0.04T_c$. The increase of the parameter γ_{BM} is accompanied by a shift of the values of this temperature towards $T = 0$, so that at $\gamma_{BM} = 2$, the value of T_{Th} turns out to be equal to $\approx 0.025T_c$. At $T = T_{Th}$ and below the critical current reaches saturation. So the first derivative dI_c/dT is zero at $T \lesssim T_{Th}$. From the presented in figures 3d,f dependences it also follows that there are two extra points to be mentioned. At $T \approx E_T$ and $\gamma_{BM} < 5$ the local minimum of the derivative is reached. At $T \approx E_T/2$ an inflection point of dI_c/dT appears for $\gamma_{BM} < 5$. Qualitatively, this point corresponds to the transition area between the saturation region and decreasing part of $I_c(T)$ dependence. These reference points at $T = E_T/2$ and $T = E_T$ can be useful when values of $T = T_{Th}$ are difficult to achieve due to limitations on the temperature range allowed for measurements. In the limit $\gamma_{BM} \gg 5$ the effective impact of boundaries increases and the positions of the considered points $T \approx E_T/2$ and $T \approx E_T$ are shifted.

Note that in the limit of a small critical current the boundary value problem (20)-(25) may also have an analytical solution. This limit is realized in the case when it is possible to neglect the suppression of anomalous Green's functions induced in the N-film by the current flowing through it.

4 Critical current of the long SN-N-NS bridge

In the $L \gg \xi$ limit, the superconducting state near the center of the bridge can be described by the superposition of anomalous Green's functions (13)–(14) penetrating from the superconducting banks into the bridge (see Refs.[16, 49, 50])

$$\frac{\Phi}{\omega} = \tan\left[\theta\left(-x-\frac{L}{2}\right)\right] e^{-i\frac{\varphi}{2}} + \tan\left[\theta\left(x-\frac{L}{2}\right)\right] e^{i\frac{\varphi}{2}}, \tag{26}$$

where $\theta(x)$ is the solutions of the proximity problem (12)–(14). By substituting this solution of the Usadel equations into the expression for the supercurrent [see Eq. (23)], we arrived at a sinusoidal dependence of the supercurrent on the phase difference φ with a critical current density equals to

$$\frac{I_c}{I_0} = \frac{128\pi T}{T_c} \sum_{\omega} \tan^2\left(\frac{1}{2}\arctan\frac{\sin\frac{\theta(\infty)}{2}}{\cos\frac{\theta(\infty)}{2} + g}\right) e^{-\frac{L}{\xi_\omega}}. \tag{27}$$

In the considered approximation ($L \gg \xi$) the critical current value is determined by the first term in the sum in Eq. (27):

$$\frac{I_c}{I_0} = \frac{128\pi T}{T_c} \tan^2\left(\frac{1}{2}\arctan\frac{\sin\frac{\theta(\infty)}{2}}{\cos\frac{\theta(\infty)}{2} + g}\right) e^{-\frac{L}{\xi}}, \tag{28}$$

where $\theta(\infty)$ is determined by Eq. (6) with $n = 0$, that is $\omega = \pi T$. The expression (28) is an analog of the formula (2) derived in Ref.[16] for SNS structures with rigid boundary conditions at the SN boundaries. Unlike from Eq. (2), the expression (28) takes into account both the finite transparency of the SN boundaries and the delocalization of the weak-link region.

Note that the expression (27) is also valid in the limit of large $\gamma_{BM} \gg 1$, if the distance L between the SN electrode is not too small, so that the sum in Eq. (27) converges at

$$\omega \lesssim \frac{\pi T_c}{\gamma_{BM}} \max\left[1, \frac{L}{\xi_N}\right]. \tag{29}$$

5 Comparison with experimental data

Theoretical results given above explain how T_{Th} can be determined on the basis of the available (calculated or experimentally obtained) $I_c(T)$ dependence. Then using the formula (19) one can find such an important parameter for practical applications as the effective geometric size of the SN-N-NS Josephson contacts

$$L_{\text{eff}} = L + \xi_N\sqrt{\gamma_{BM}}. \tag{30}$$

Note that Eq. (30) is a direct consequence of Eq. (19) and is valid up to $\gamma_{BM} \approx 100$, as it can be observed from the comparison of the exact (16) and asymptotic (19) solutions for E_T in figure 2.

Our experimental study of a supercurrent transport across Nb/Cu-Cu-Cu/Nb[34] and Nb/Au-Au-Au/Nb[39, 41] bridges has shown that the shape of the exponentially-decreasing dependences of $I_c(T)$ in a wide temperature

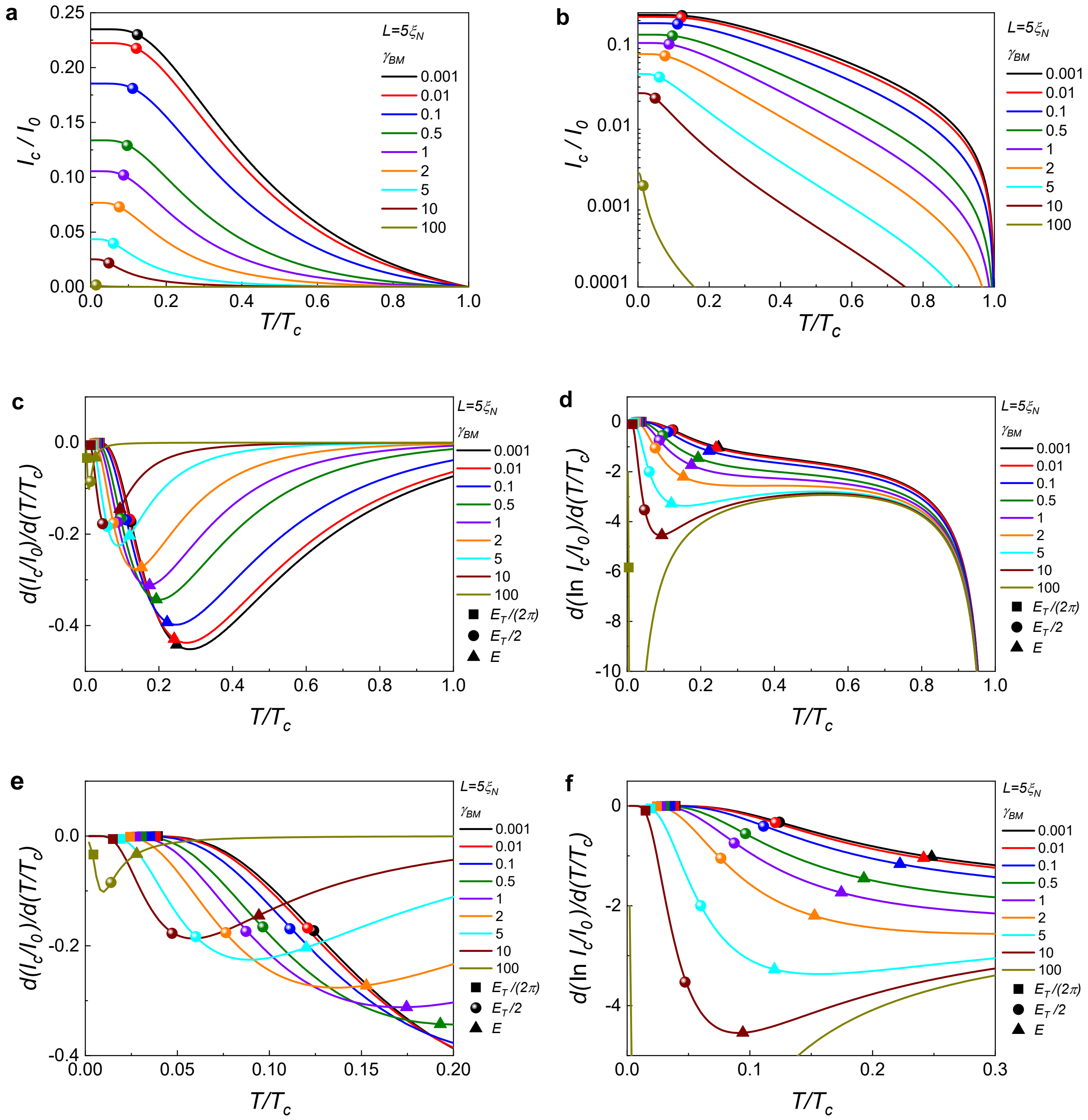

Figure 3. **a**, **b** – Temperature dependences of the critical current density I_c of the SN-N-NS bridge with $L = 5\xi$ calculated numerically for different interface parameters γ_{BM} in linear (panel a) and logarithmic (panel b) scales. **c-f** – Temperature dependences of the first derivative of the critical current density $\frac{dI_c/I_0}{dT/T_c}$ for the same parameters in linear (panel c) and logarithmic (panel d) scales, respectively. The squares, points, and triangles on each of the calculated curves show the temperature values corresponding to $E_T/(2\pi)$, $E_T/2$, and E_T, respectively. The values of E_T were calculated using the expression (19) for each combination of γ_{BM} and ξ_N parameters. Panels e and f are enlarged versions of panels c and d in the low-temperature region.

range closely resembles that shown in figure 3. At $\gamma_{BM} \lesssim 5$ and large values of $L \gtrsim 4\xi_N$ there is the transition at $T \approx T_c(\xi_N/L)^2$ from a sharp rise of $I_c(T)$ to a smoother saturation at $T \ll T_c$ as temperature decreases. At $\gamma_{BM} \gtrsim 5$ and small values of $L \lesssim 4\xi_N$ the change in the slope of the $I_c(T)$ dependence takes place at $T \approx T_c/\gamma_{BM}$.

In figure 4a we show the most recent experimental data for the Nb/Au-Au-Au/Nb Josephson bridge with a diffusive Au stripe operating as weak link. This structure was fabricated by magnetron sputtering and lift-off lithography. Further information concerning the fabrication process can be found in Refs.[39,41,51] The approximate distance between the SN electrodes can be estimated as $L \approx 160\,\mathrm{nm}$ based on the scanning electron microscopy (see figure 1b). The thicknesses of niobium and gold layers are equal approximately 70 nm and 32 nm,

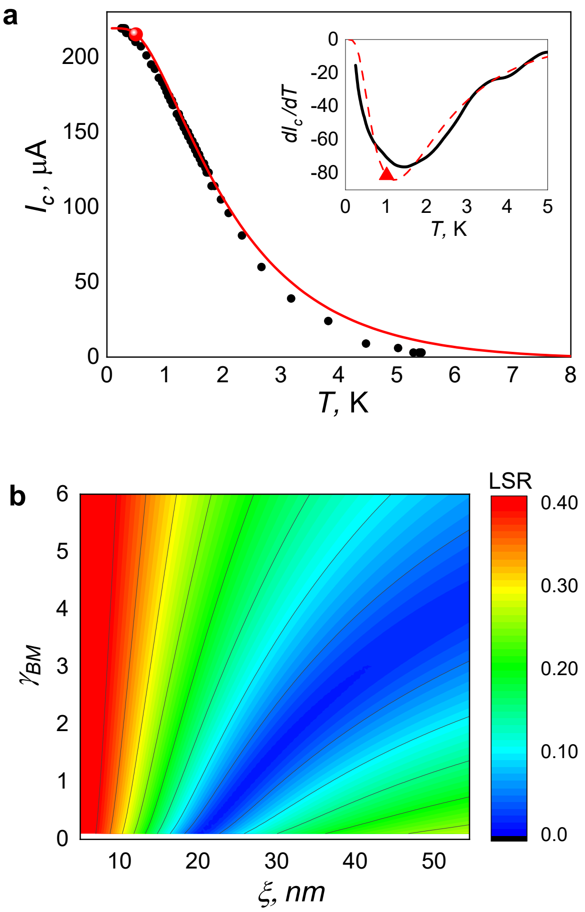

Figure 4. **a** – Temperature dependence of the critical current $I_c(T)$ for the NbAu-Au-AuNb bridge with the length of the weak link $L = 160$ nm (black circles) and numerical fits in the framework of the model (20)-(25) calculated at $\xi_N = 23$ nm and $\gamma_{BM} = 0.12$ (red line). The red dot marks the temperatures corresponding to the halfed Thouless energy $E_T/2$. The inset shows the derivative $dI_c(T)/dT$ of the interpolated experimental (black solid line) and model (red dashed line) $I_c(T)$ dependencies. **b** – The least-squares residual between the experimental data and the model fits in the $\gamma_{BM} - \xi$ plane of the parameters.

respectively.

To compare the experimental data presented in figure 4a with the results of the theoretical calculations, we construct a map which shows the dependence of the standard deviation between the experimental data and calculated dependence. The least-squares calculation of the standard deviation of the theoretical values of the critical current from the experimentally obtained points is shown in figure 4b. This procedure results in a detection of a valley on the $\gamma_{BM} - \xi$ diagram where the experimental points agree quite well with the theoretical calculation. It can be seen that the presence of two free parameters γ_{BM} and ξ does not lead to unique fitted solution. For different sets of γ_{BM} and ξ the formula (19) gives different E_T values.

It should be noted that for the considered case the expression (19) allows us to specify the range of parameters in which it is worthwhile to search for a solution of the system at sufficiently large effective bridge lengths $L \gtrsim 5\xi$ and transparent interfaces $\gamma_{BM} \lesssim 1$. As an example, in figure 4a we have shown one of possible approximation of the experimental dependence $I_c(T)$ with the solution of the Usadel equations obtained for $\xi_N = 23$ nm ($L/\xi_N \approx 7$) and $\gamma_{BM} = 0.12$ (red line). A large red dot on this graph marks the temperature $T \approx 0.5\,$K, which corresponds to $E_T/2$ [see Eq. (19)]. The inset in figure 4a shows the derivative of the theoretical dI_c/dT dependence (red dashed line) and the interpolation curve obtained for the experimental points. The red triangle also marks the point where the temperature $T \approx 1$K coincides with the value corresponding to E_T. It is located near the minimum of the derivative dI_c/dT.

It should be emphasized that according to Eq. (30) for $L/\xi_N \approx 7$ and $\gamma_{BM} = 0.12$ the effective size of the structure $L_{\text{eff}} \approx 7.3\xi_N$ is actually determined by the distance between the electrodes L. In this case, the features of the shape of the dependence $I_c(T)$ are due to the transition from exponential to power laws of growth of I_c with decreasing temperature. As it can be illustrated in figure 3, the position of these features correlates quite well with T_{Th}. For shorter bridges ($L \lesssim 3\xi$) the $I_c(T)$ dependences are smoother and the bending of the curves $dI_c(T)/dT$ at $T = E_T/2$ are not as clear as for large L values. Also, in these case the interface parameter γ_{BM} increases resulting in a change of the shape of the $I_c(T)$ dependence.

Thus, we have shown that the expression (19) can be used to determine the range of parameters in which the optimal approximation of the experimental results should be sought. For a more unambiguous extraction of the structural parameters from the experimental dependence $I_c(T)$, it is necessary to approximate several samples simultaneously with different lengths between the electrodes L, as done in Refs.[34,41] and use additional data ρ_n and γ_B extracted from the temperature dependence of the normal-state resistance at $T > T_c$. This approach allows one to significantly reduce the range of parameters for the best fitting by the microscopic model. However, it requires a complete construction of the parameter map, which is a rather time-consuming.

We demonstrate that the theoretical curve fits the experimental data well at $T \lesssim 4\,$K. The observed discrepancy between the theoretical predictions and the experimental data at higher temperatures ($T \gtrsim 4\,$K) may be due to the following reasons.

Possible difference in the critical temperature of the region of the S layer adjacent to the N-film T_{cl} compared to the measured T_c of the bulk S electrode, as well as coordinate dependence of T_{cl}. Another factor could be an inhomogeneity of the transparency of the NS boundaries, caused both by mechanical stresses at the NS interfaces, and their roughness. All these factors lead to the appearance of inhomogeneous island-type superconductivity in the N-layer which is more pronounced at $T \to T_c$, *i.e.*, to the appearance of the dependence $\delta(x)$ in Eq. (22), which was not considered in the developed theory.

It should be noted that such a successful coincidence of the Thouless energy values found from the numerically calculated dependences $I_c(T)$ and ones based on expression (19) does not mean that the E_T values determined from the shape of the experimental curves $I_c(T)$ will lead to the same $L_{\rm eff}$ value determined by Eq. (30). A deviation of the experimentally determined $L_{\rm eff}$ value and the effective length defined by Eq. (30) may be due to the fact that some constrains controlling the applicability of the considered one-dimensional SN-N-NS contact are not realized experimentally.

Such restrictions include:

1. The smallness of the N-layer thickness compared to the decay length ξ_N. When using low-resistivity normal metals (Al, Au, Ag), the closeness of d to ξ_N can lead partial suppression of superconductivity in the S-layer near the SN boundary.[52,53]

$$\frac{d}{\xi_N}\frac{\rho_S}{\rho_N}\frac{\xi_S}{\xi_N} \lesssim 0.3, \tag{31}$$

where ρ_S and ξ_S are normal-state resistivity and coherence length of the S-film. Going beyond the one-dimensional approximation, the temperature T_{Th} actually decreases as d increases.[54] This automatically leads to an increase in the effective size of the SN-N-NS structure with respect to the $L_{\rm eff}$ value defined by expression (30).

2. The boundary condition (25) states that the current flowing through the N-layer of the SN composite electrode is negligible compared to the current that has entered the S-layer of the electrode, i.e.

$$\frac{d}{d_S}\frac{\rho_S}{\rho_N} \ll (1+\gamma_{BM})^2, \tag{32}$$

where d_S is the thickness of the S-film. A violation of this constraint should lead to the appearance of the dependence of the phase difference φ on the x-coordinate (see also the discussion in point 4 below).

3. At any point of the SN boundary, the density of the supercurrent injected from the normal metal through this interface into the S-layer should be less than the critical current density controlled by the finite transparency of this boundary, *i. e.*

$$1+\gamma_{BM}^{-1} > \frac{d}{\zeta}\max\left[\frac{\xi_N}{L}, 1\right]. \tag{33}$$

4. The final constrain arises from the assumption that the phase difference φ appearing in Eqs. (20) and (22) is independent of the x-coordinate. This assumption is valid for $x \gg L/2$. Away from the N-NS boundary, the superconducting current is uniformly distributed across the thickness of the NS electrode. The current flows along the $0x$ direction, so the current lines do not cross the NS boundary. As a result, at $x \gg L/2$ the phase of the order parameter in each cross sections of the NS electrode turns out to be equal to the phase of the anomalous Green's functions in both N and S-layers, and the $\varphi(x)$ function turns out to be a value independent of x (see Ref.[11] for details).

Conclusion

Thus, through analytical evaluations and numerical calculations, we have shown that the Thouless energy in Josephson SN-N-NS bridges strongly depends on the resistance of the SN interface. The Thouless energy decreases by several times as this resistance increases compared to the SNS sandwich-type contact. We have also specified the range of validity of our analytical results, thus providing the possible explanations for the deviation of the experimentally obtained L_{eff} from our analytical result (30).

The Thouless energy cannot be measured directly. Instead, the Thouless temperature can be determined by analyzing the shape characteristics of experimentally obtained $I_c(T)$ dependences. Thouless temperature can be defined as the temperature corresponding to the saturation of the $I_c(T)$ dependence at low temperatures and vanishing of the first derivative dI_c/dT. The use of this method for the experimental determination of T_{Th} requires measurements at rather low temperatures, which causes additional difficulties in finding T_{Th}. We have shown that the transition from the study of the dependence $I_c(T)$ to the determination of peculiar points on the temperature dependences of $dI_c(T)/dT$ located at $T \approx E_T/2$ and $T \approx E_T$ allows us to estimate the E_T value in the range of temperatures more convenient for measurements.

Our numerical calculations carried out in the framework of the one-dimensional SN-N-NS model of the Josephson SN-N-NS structure have shown that there is a relationship between the value of the Thouless energy $E_T = 2\pi T_{Th}$ determined in this way and the effective geometrical size of the structure $L_{\rm eff}$ [see Eq. (30)] included in formula (19). The estimate of $L_{\rm eff}$ obtained in this way is important in determining the limitations to miniaturization of the size of superconductor devices for processing analog and digital signals. It also provides additional information on the relationship between important technological parameters such as the NS electrode spacing L, decay length ξ_N, and the parameter γ_{BM}, which characterizes the transparency of NS boundaries.

Acknowledgements

We are grateful to A. I. Zaikin and A. A. Golubov for the discussion of the results obtained. A.N. thanks the support of the Foundation for the Development of Theoretical Physics and Mathematics "BASIS". The authors are grateful to MIPT Collective Use Center for providing facilities for samples fabrication. The experiments were carried out with the support of the Russian Science Foundation, Grant No. 23-72-30004.

Contact information

Corresponding author: Sergey V. Bakurskiy, orcid.org/0000-0002-6010-6697, e-mail r3zz@mail.ru.

Competing Interests

The authors declare no competing financial or non-financial interests.

References

[1] Kupriyanov M. Y., Brinkman A., Golubov A. A., Siegel M., Rogalla H. *Double-barrier Josephson structures as the novel elements for superconducting large-scale integrated circuits.* Physica C, vol. **326**, 16-45 (1999).

[2] Holmes D. S., Ripple A. L., Manheimer M. A. *Energy-Efficient Superconducting Computing-Power Budgets and Requirements.* IEEE Trans. Appl. Supercond, vol. **23**, 1701610 (2013).

[3] Shelly C. D, See P., Ireland J., Romans E. J., Williams, J. M. *Weak link nanobridges as single flux quantum elements.* Supercond. Sci. Technol., vol. **30**, 095013 (2017).

[4] Tolpygo S. K. *Superconductor Digital Electronics: Scalability and Energy Efficiency Issues.* Low Temp. Phys., vol. **42**, 361-379 (2016).

[5] Semenov V. K., Polyakov Y. A., Tolpygo S. K. *Very large scale integration of Josephson-junction-based superconductor random access memories.* IEEE Trans. Appl. Supercond, vol. **29**, 1302809 (2019).

[6] Collins J. A., Rose C. S., Casaburi A. *Superconducting Nb Nanobridges for Reduced Footprint and Efficient Next-Generation Electronics.* IEEE Trans. Appl. Supercond, vol. **33**, 1800208 (2023).

[7] Thompson M. L., Castellanos-Beltran M., Hopkins P. F., Dresselhaus P. D.; Benz S. P. *Effects of Nonsinusoidal Current Phase Relationships on Single Flux Quantum Circuits.* IEEE Trans. Appl. Supercond, vol. **33**, 1300205 (2022).

[8] Tolpygo S. K., Rastogi R., Weir T., Golden E. B., Bolkhovsky V. *Development of Self-Shunted Josephson Junctions For a Ten-Superconductor-Layer Fabrication Process: Nb/NbN$_x$/Nb Junctions.* arXiv preprint:2312.13475 (2023).

[9] Tolpygo S. K., Rastogi R., Weir T., Golden E. B., Bolkhovsky V. *Development of Self-Shunted Josephson Junctions for a Ten-Superconductor-Layer Fabrication Process: Nb/NbN$_x$/Nb Junctions.* IEEE Trans. Appl. Supercond, vol. **34**, 1101008 (2024).

[10] Soloviev I. I., Bakurskiy S. V., Ruzhickiy V. I., Klenov N. V., Kupriyanov M. Yu., Golubov A. A., Skryabina O. V., Stolyarov V. S. *Miniaturization of Josephson junctions for digital superconducting circuits.* Phys. Rev. Appl., vol. **16**, 044060 (2021).

[11] Ruzhickiy V., Bakurskiy S., Kupriyanov M., Klenov N., Soloviev I., Stolyarov V., Golubov A. *Contribution of Processes in SN Electrodes to the Transport Properties of SN-N-NS Josephson Junctions.* Nanomaterials, vol. **13**, 1873 (2023).

[12] Likharev K. K. *Superconducting weak links.* Rev. Mod. Phys., vol. **51**, 101 (1979).

[13] Golubov A. A., Kupriyanov M. Yu., Il'ichev E. *The current-phase relation in Josephson junctions.* Rev. Mod. Phys., vol. **76**, 411 (2004).

[14] Likharev K. K. Sov. Tech. Phys. Lett., vol. **2**, 12-13 (1976).

[15] Ivanov Z. G., Kupriyanov M. Y., Likharev K. K., Meriakri S. V., Snigirev, O. V. *Boundary-conditions for the Usadel and Eilenberger equations, and properties of dirty SNS sandwich-type junctions.* Sov. J. Low. Temp. Phys., vol. **7**, 274-281 (1981).

[16] Zaikin A., Zharkov G. Sov. J. Low Temp. Phys., vol. **7**, 184-185 (1981).

[17] Dubos P., Courtois H., Pannetier B., Wilhelm F. K., Zaikin A. D., Schön G. *Josephson critical current in a long mesoscopic SNS junction.* Phys. Rev. B, vol. **63**, 064502 (2001).

[18] Hammer J. C., Cuevas J. C., Bergeret F. S., Belzig, W. *Density of states and supercurrent in diffusive SNS junctions: Roles of nonideal interfaces and spin-flip scattering.* Phys. Rev. B, vol. **76**, 064514 (2007).

[19] Marychev P. M., Vodolazov D. Yu. *A Josephson junction based on a highly disordered superconductor/low-resistivity normal metal bilayer.* Beilstein J. Nanotechnol., vol. **11**, 858–865 (2020).

[20] Giazotto F., Heikkilä T. T., Luukanen A., Savin A. M., Pekola J. P. *Opportunities for mesoscopics in thermometry and refrigeration: Physics and applications.* Rev. Mod. Phys., vol. **78**, 217 (2006).

[21] Angers L., Chiodi F., Montambaux G., Ferrier M., Guéron S., Bouchiat H., Cuevas J. C. *Proximity dc squids in the long-junction limit.* Phys. Rev. B., vol. **77**, 165408 (2008).

[22] Courtois H., Meschke M., Peltonen J. T., Pekola J. P. *Origin of hysteresis in a proximity Josephson junction.* Phys. Rev. Lett., vol. **101**, 067002 (2008).

[23] Carillo F., Born D., Pellegrini V., Tafuri F., Biasiol G., Sorba L., Beltram F. *Relevant energy scale in hybrid mesoscopic Josephson junctions.* Phys. Rev. B, vol. **78**, 052506 (2008).

[24] García C. P., Giazotto F. *Josephson current in nanofabricated V/Cu/V mesoscopic junctions.* Appl. Phys. Lett., vol. **94**, 132508 (2009).

[25] Giazotto F., Peltonen J. T., Meschke M., Pekola J. P. *Superconducting quantum interference proximity transistor.* Nature Phys., vol. **6**, 254-259 (2010).

[26] Frielinghaus R., Batov I. E., Weides M., Kohlstedt H., Calarco R., Schäpers Th. *Josephson supercurrent in Nb/InN-nanowire/Nb junctions.* Appl. Phys. Lett., vol. **96**, 132504 (2010).

[27] Jung M., Noh H., Doh Y.-J., Song W., Chong Y., Choi M.-S., Yoo Y., Seo K., Kim N., Woo B.-C., Kim B., Kim J. *Superconducting junction of a single-crystalline Au nanowire for an ideal Josephson device.* ACS Nano, vol. **5**, 2271-2276 (2011).

[28] Golikova T. E., Hubler F., Beckmann D., Klenov N. V., Bakurskiy S. V., Kupriyanov M. Yu., Batov I. E., Ryazanov V. V. *Critical current in planar SNS Josephson junctions.* JETP Lett., vol. **96**, 668-673 (2012).

[29] Golikova T. E., Wolf M. J., Beckmann D., Batov I. E., Bobkova I. V., Bobkov A. M., Ryazanov, V. V. *Nonlocal supercurrent in mesoscopic multiterminal SNS Josephson junction in the low-temperature limit.* Phys. Rev. B, vol. **89**, 104507 (2014).

[30] Pekola J. P. *Towards quantum thermodynamics in electronic circuits.* Nature Phys., vol. **11**, 118-123 (2015).

[31] Paajaste J., Amado M., Roddaro S., Bergeret F. S., Ercolani D., Sorba L., Giazotto F. *Pb/InAs nanowire Josephson junction with high critical current and magnetic flux focusing.* Nano Lett., vol. **15**, 1803-1808 (2015).

[32] De Cecco A., Le Calvez K., Sacépé B., Winkelmann C. B., Courtois H. *Interplay between electron overheating and ac Josephson effect.* Phys. Rev. B, vol. **93**, 180505 (2016).

[33] Jabdaraghi R. N., Peltonen J. T., Saira O.-P., Pekola J. P. *Low-temperature characterization of Nb-Cu-Nb weak links with Ar ion-cleaned interfaces.* Appl. Phys. Lett., vol. **108**, 042604 (2016).

[34] Skryabina O. V., Egorov S. V., Goncharova A. S., Klimenko A. A., Kozlov S. N., Ryazanov V. V., Bakurskiy S. V., Kupriyanov M. Yu., Golubov A. A., Napolskii K. S., Stolyarov V. S. *Josephson coupling across a long single-crystalline Cu nanowire.* Appl. Phys. Lett., vol. **110**, 222605 (2017).

[35] Kim B.-K., Kim H.-S., Yang Y., Peng X., Yu D., Doh Y.-J. *Strong superconducting proximity effects in PbS semiconductor nanowires.* ACS Nano, vol. **11**, 221-226 (2017).

[36] Shishkin A. G., Skryabina O. V., Gurtovoi V. L., Dizhur S. E., Faley M. I., Golubov A. A., Stolyarov V. S. *Planar MoRe-based direct current nanoSQUID.* Supercond. Sci. Technol., vol. **33**, 065005 (2020).

[37] Zhang J., Jalil A. R., Tse P.-L., Kölzer J., Rosenbach D., Valencia H., Luysberg M., Mikulics M., Panaitov G., Grützmacher D., Hu Z., Lu J. G., Schäpers Th. *Proximity-Effect-Induced Superconductivity in Nb/Sb_2Te_3-Nanoribbon/Nb Junctions.* Ann. Phys., vol. **532**, 2000273 (2020).

[38] Murani A., Sengupta S., Kasumov A., Deblock R., Celle C., Simonato J. P., Bouchiat H., Guéron S. *Long-to short-junction crossover and field-reentrant critical current in Al/Ag-nanowires/Al Josephson junctions.* Phys. Rev. B, vol. **102**, 214506 (2020).

[39] Skryabina O. V., Bakurskiy S. V., Shishkin A. G., Klimenko A. A., Napolskii K. S., Klenov N. V., Soloviev I. I., Ryazanov V. V., Golubov A. A., Roditchev D., Kupriyanov M. Yu., Stolyarov V. S. *Environment-induced overheating phenomena in Au-nanowire based Josephson junctions.* Sci. Rep., vol. **11**, 15274 (2021).

[40] Golod T., Hovhannisyan R. A., Kapran O. M., Dremov V. V., Stolyarov V. S., Krasnov V. M. *Reconfigurable Josephson phase shifter.* Nano Lett., vol. **21**, 5240-5246 (2021).

[41] Sotnichuk S. V., Skryabina O. V., Shishkin A. G., Bakurskiy S. V., Kupriyanov M. Yu., Stolyarov V. S., Napolskii K. S. *Long Single Au Nanowires in Nb/Au/Nb Josephson Junctions: Implications for Superconducting Microelectronics.* ACS Applied Nano Materials, vol. **11**, 17059-17066 (2022).

[42] Babich I., Kudriashov A., Baranov D., Stolyarov V. S. *Limitations of the Current–Phase Relation Measurements by an Asymmetric dc-SQUID.* Nano Lett., vol. **23**, 6713-6719 (2023).

[43] Edwards J. T., Thouless D. J. *Numerical studies of localization in disordered systems.* J. Phys. C: Solid State Phys., vol. **5**, 807 (1972).

[44] Thouless D. J. *Maximum Metallic Resistance in Thin Wires.* Phys. Rev. Lett., vol. **39**, 1167–1169 (1977).

[45] Thouless D. J. *Electrons in disordered systems and the theory of localization.* Phys. Rep., vol. **13**, 93-142 (1974).

[46] Altland A., Gefen Y., Montambaux G. *What is the Thouless Energy for Ballistic Systems?* Phys. Rev. Lett., vol. **76**, 1130-1133 (1996).

[47] Usadel K. D. *Generalized diffusion equation for superconducting alloys.* Phys. Rev. Lett., vol. **25**, 507 (1970).

[48] Golubov A. A., Kupriyanov M. Y., Siegel, M. *Density of states anomalies in hybrid superconductor-ferromagnet-normal metal structures.* JETP Lett., vol. **81**, 180-184 (2005).

[49] Likharev K. K., Iakobson L. A. *Steady-state properties of superconducting bridges.* Sov. Phys. – Tech. Phys., vol. **20**, 950 (1975).

[50] Kupriyanov M. Yu., Lukichev V. F. *The influence of the proximity effect in the electrodes on the stationary properties of S–N–S Josephson structures.* Sov. J. Low Temp. Phys., vol. **8**, 526-529 (1982).

[51] Fabrication process details along with the full experimantal data for these series of the junctions will be published elsewhere soon.

[52] Kupriyanov M. Yu., Lukichev V. F., Orlikovskii A. A. *Stationary properties of quasi-two-dimensional josephson weak links.* Sov. Microelectronics, vol. **15**, 185-189 (1986).

[53] Baryshev Y. P., Vasil'ev A. G., Dmitriyev A. A., Kupriyanov M. Y., Lukichev V. F., Luk'yanova I. Y., Sokolova I. S. *Theoretical and experimental study of the josephson effect in submicron SN-N-NS structures.* Lithography in microelectronics, vol. **8**, 187-197 (1989).

[54] Bosboom V., Van der Vegt J. J. W., Kupriyanov M. Yu., Golubov A. A. *Selfconsistent 3D model of SN-N-NS Josephson junctions.* Supercond. Sci. Technol., vol. **34**, 115022 (2021).

Editor's note: We invite readers to explore the philosophy of the Journal [V. Stolyarov, Mesosci. Nanotechnol., vol. 1, 01001 (2023)] and consider the possibility of submitting their contributions for publication in our Journal.

DOI: 10.64214/jmsn.01.01004 **Review**

Néel proximity effect in superconductor/antiferromagnet heterostructures

I. V. Bobkova,[1] G. A. Bobkov,[1] V. M. Gordeeva,[1] A. M. Bobkov[1]

[1] *Center for Advanced Mesoscience and Nanotechnology, Moscow Institute of Physics and Technology, Dolgoprudny 141700, Russia*

submitted 13 February 2024, accepted 16 July 2024, published 13 August 2024

It is well-known that the cornerstone of the proximity effect in superconductor/ferromagnet heterostructures is a generation of triplet Cooper pairs from singlet Cooper pairs inherent in a conventional superconductor. This proximity effect brought a lot of new exciting physics and gave a powerful impulse to development of superconducting spintronics. Nowadays a new direction of spintronics is actively developing, which is based on antiferromagnets and their heterostructures. It is called antiferromagnetic spintronics. By analogy with an important role played by triplet Cooper pairs in conventional superconducting spintronics based on ferromagnets the question arises: does the triplet proximity effect exist in superconductor/antiferromagnet heterostructures and, if so, what are the properties of the induced triplet correlations and the prospects for use in superconducting spintronics? Recent theoretical findings predict that despite the absence of a net magnetization, the Néel magnetic order of the antiferromagnet does give rise to specific spin-triplet correlations at superconductor/antiferromagnet interfaces. They were called Néel triplet correlations. The goal of this review is to discuss the current understanding of the fundamental physics of these Néel triplet correlations and their physical manifestations.

1 Introduction

Superconducting proximity effect in mesoscopic heterostructures composed of conventional superconductors and normal, that is nonsuperconducting and nonmagnetic, metals (S/N heterostructures) is a penetration of Cooper pairs from a superconductor into an adjacent nonsuperconducting material with partial suppression of the superconducting order parameter in the superconductor near the interface. Conventional superconductors are formed by spin-singlet Cooper pairs[1,2] and, therefore, they induce spin-singlet superconducting correlations in the adjacent normal metal. If a normal metal is replaced with a ferromagnet, the spin-singlet pairs, which penetrate into the ferromagnet, are partially converted into their spin-triplet counterparts due to the presence of a macroscopic spin-splitting field in it.[3–5] Simultaneously the triplet pairs are also induced in the superconductor due to an inverse proximity effect. The same effect occurs if a thin superconducting film is subjected to a parallel magnetic field or if the superconductor is contacted with a ferromagnetic insulator.[6] The triplet pairs are produced at the expense of the singlet ones. This weakens the conventional superconducting state and lowers the critical temperature.[7–9] The generation of triplet Cooper pairs in superconductor/ferromagnet (S/F) heterostructures brought a lot of new exciting physics[3,4] and gave a powerful impulse to development of superconducting spintronics.[5,10,11]

Now what is about the proximity effect in superconductor/antiferromagnet (S/AF) heterostructures? Naively, since the net magnetization in an antiferromagnet averaged over the size of a typical Cooper pair vanishes, one should expect that S/AF heterostructures behave like S/N heterostructures from the point of view of the proximity effect. This means that (i) only singlet pairs can penetrate into the antiferromagnetic metal, and (ii) a superconductor interfaced to antiferromagnetic metal or insulator via a compensated interface is expected to experience no net spin-splitting and reduction in critical temperature.[12] Any macroscopic spin-splitting in S/AF heterostructures is only expected via an uncompensated (non-zero) interface magnetization. Indeed, it was predicted that the uncompensated interface induces a spin-splitting field in thin-film S/AF bilayers,[13] which can result in some physical effects similar to thin-film S/F heterostructures,[5] for example, in the giant thermoelectric effect,[14] the anomalous phase shift[15] and anisotropy of the critical current in S/AF/S Josephson junctions with spin-orbit coupling.[16]

However, it was realized long ago that in fact antiferromagnetism influences superconductivity not only via the uncompensated interface magnetization. In particular, it was reported that in antiferromagnetic superconductors the staggered exchange field suppresses superconductivity due to changes in the density of states and due to atomic oscillations of electronic wave functions.[17] The atomic oscillations of the electronic wave functions in antiferromagnetic materials also lead to the fact that nonmagnetic impurities in antiferromagnetic superconductors behave like effectively magnetic and additionally suppress superconductivity.[17] Further the theory taking into account the suppression of superconductivity by magnetic impurities was also developed for S/AF heterostructures.[18,19] Several experiments have found that AFs lower the critical temperature of an S layer,[20–23] despite there is no net spin-splitting. In some cases, the effect has been comparable or even larger than that induced by a ferromagnet layer.[22] Of course, a number of physical reasons can contribute to this observation. First, an AF doubles the spatial period of the lattice due to its antiparallel spins on the two sublattices. This can open a bandgap in the adjacent conductor, which may reduce the normal-state density of states in S, and thus suppress superconductivity.[17,24] Second, partially the suppression can result from the uncompensated magnetization of the S/AF interface, which seems to be common in experiments[13,25–27] and induces a spin-splitting and spin-flipping disorder in the superconductor, just like a ferromagnet.[13] Furthermore, the nonmagnetic disorder in the S/AF system also suppresses superconductivity, as it was mentioned above. Although all these physical effects are likely present in real systems, they are not associated with a physics of proximity-induced triplet superconducting correlations, which are a cornerstone of the physics and applications of S/F hybrids. Therefore, an important question arises whether triplet correlations in S/AF hybrid systems can arise only due to uncompensated surface magnetization or the Néel magnetism itself is also capable to generate new types of superconducting proximity effect.

Some unconventional for S/N heterostructures physical effects in S/AF hybrids with compensated interfaces were reported in the literature. For example, unconventional Andreev reflection and bound states at such S/AF interfaces have been predicted.[28,29] The atomic-thickness $0-\pi$ transitions in S/AF/S Josephson junctions were investigated theoretically,[30–32] an analysis of a hybrid comprising a ferromagnet and a compensated AF interfaced with an S suggested the interface to be spin-active.[33] All these results indicated that a key piece of understanding of the physics of S/AF hybrids was missing.

Further it was found that in spite of the absence of a net magnetization, the Néel magnetic order of the AF induces spin-triplet correlations at S/AF interfaces, which penetrate both into the superconductor and into the metallic antiferromagnet.[34] Their amplitude flips sign from one lattice site to the next similar to the Néel magnetic order in the AF. These correlations were called Néel triplet Cooper pairs. The goal of this review is to discuss the current understanding of the fundamental physics of these Néel triplet correlations and their physical manifestations.

2 Néel triplet correlations at S/AF interfaces

2.1 Bogolubov-de Gennes visualization of the Néel triplets

Let us consider an antiferromagnetic insulator interfaced via a compensated interface to a thin conventional s-wave superconductor (figure 1a). The system can be described by the following tight-binding Hamiltonian:

$$\hat{H} = -t \sum_{\langle \boldsymbol{ij} \rangle, \sigma} \hat{c}^{\dagger}_{\boldsymbol{i}\sigma} \hat{c}_{\boldsymbol{j}\sigma} + \sum_{\boldsymbol{i}} (\Delta_{\boldsymbol{i}} \hat{c}^{\dagger}_{\boldsymbol{i}\uparrow} \hat{c}^{\dagger}_{\boldsymbol{i}\downarrow} + H.c.) - \mu \sum_{\boldsymbol{i},\sigma} \hat{n}_{\boldsymbol{i}\sigma} + \sum_{\boldsymbol{i},\alpha\beta} \hat{c}^{\dagger}_{\boldsymbol{i}\alpha} (\boldsymbol{h_i} \boldsymbol{\sigma})_{\alpha\beta} \hat{c}_{\boldsymbol{i}\beta}, \quad (1)$$

where $\boldsymbol{i} = (i_x, i_y)^T$ is the radius vector of the site and Greek letters correspond to the spin indices. $\langle \boldsymbol{ij} \rangle$ means summation over the nearest neighbors. Here, $\Delta_{\boldsymbol{i}}$ and $\boldsymbol{h_i}$ denote the on-site superconducting order parameter and the magnetic exchange field at site $\boldsymbol{i}$, respectively; $\hat{c}^{\dagger}_{\boldsymbol{i}\sigma}$ and $\hat{c}_{\boldsymbol{i}\sigma}$) are operators of creation and annihilation an electron with spin $\sigma = \uparrow, \downarrow$ on the site $\boldsymbol{i}$; t denotes the nearest-neighbor hopping integral; μ is the chemical potential; $\hat{n}_{\boldsymbol{i}\sigma} = \hat{c}^{\dagger}_{\boldsymbol{i}\sigma} \hat{c}_{\boldsymbol{i}\sigma}$ is the particle number operator at the site $\boldsymbol{i}$. We also define the vector of the Pauli matrices in spin space $\boldsymbol{\sigma} = (\sigma_x, \sigma_y, \sigma_z)^T$. We assume that the antiferromagnet is of G-type, therefore the exchange field inside the antiferomagnet can be written in the form $\boldsymbol{h_i} = (-1)^{i_x + i_y} \boldsymbol{h}$. Axes x and y are taken normal to the S/AF interface and parallel to it, respectively. Hereafter we use the system of units, in which the reduced Planck constant $\hbar$ and the Boltzmann constant k_B are equal to unity, for the sake of compactness.

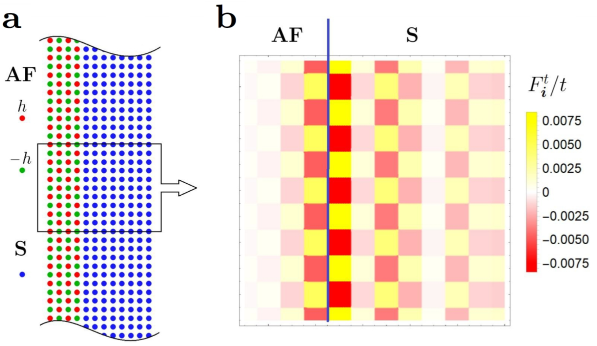

Figure 1. **a** – Sketch of the antiferromagnetic insulator with a compensated interface attached to the thin superconductor. **b** – Spatial variation of the amplitude $F^t_{\boldsymbol{i}}$ of the triplet correlations. Each colored square codes the value of $F^t_{\boldsymbol{i}}$ at a given site. An alternating sign of the correlations in S-layer commensurates with the Néel order in the AF-layer along the interface direction. The picture is adopted from Ref. [34].

The Hamiltonian (1) can be diagonalized by the Bogolubov transformation.[34] Further one can investigate the structure of the superconducting correlations at the S/AF interface using the solutions of the resulting Bogolubov-de Gennes equation. The anomalous Green's function in the Matsubara representation can be calculated as $F_{\boldsymbol{i},\alpha\beta} = -\langle \hat{c}_{\boldsymbol{i}\alpha}(\tau) \hat{c}_{\boldsymbol{i}\beta}(0) \rangle$, where τ is the imaginary time. The component of this anomalous Green's function for a given Matsubara frequency $\omega_m = \pi T(2m+1)$ is calculated as follows:

$$F_{\boldsymbol{i},\alpha\beta}(\omega_m) = \sum_n \left(\frac{u^{\boldsymbol{i}}_{n,\alpha} v^{\boldsymbol{i}*}_{n,\beta}}{i\omega_m - \varepsilon_n} + \frac{u^{\boldsymbol{i}}_{n,\beta} v^{\boldsymbol{i}*}_{n,\alpha}}{i\omega_m + \varepsilon_n} \right), \quad (2)$$

where $u^{\boldsymbol{i}}_{n,\alpha}$ and $v^{\boldsymbol{i}}_{n,\alpha}$ are electron and hole parts of the two-component eigenfunction of the Bogolubov-de Gennes equation, corresponding to the n-th eigenstate, ε_n is the eigenenergy of this state, and α, β are spin indices. Only off-diagonal in spin-space components, corresponding to opposite-spin pairs, are nonzero for the case under consideration. The singlet (triplet) correlations are described by $F^{s,t}_{\boldsymbol{i}}(\omega_m) = F_{\boldsymbol{i},\uparrow\downarrow}(\omega_m) \mp F_{\boldsymbol{i},\downarrow\uparrow}(\omega_m)$. The on-site triplet correlations are odd in Matsubara frequency, as it should be according to the general fermionic symmetry. The spin-triplet correlations amplitude $F^t_{\boldsymbol{i}}$ at each lattice site with the radius-vector $\boldsymbol{i}$ is evaluated by summing the anomalous Green's function over the positive Matsubara frequencies $F^t_{\boldsymbol{i}} = \sum_{\omega_m > 0} F^t_{\boldsymbol{i}}(\omega_m)$.

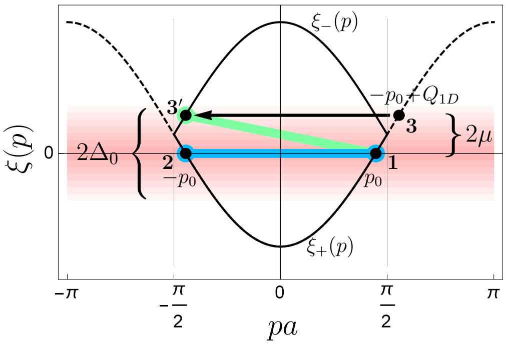

Figure 2. Electron dispersion $\xi_{\pm}(p) = \mp 2t \cos pa - \mu$ of the normal-state S in the reduced Brillouin zone (BZ) $pa \in [-\pi/2, \pi/2]$ considering a 1D system with two sites in the unit cell (solid curves). The electron energy defined by $\xi_{\pm}(p)$ is counted from the Fermi surface. The reciprocal lattice vector due to the periodicity enforced by the AF is $Q_{1D} = \pi/a$. The spectrum branches are doubled in the BZ due to the reduction of the BZ volume. The spectrum of the original 1D superconductor with one site in the unit cell in the BZ $pa \in [-\pi, \pi]$ is shown by dashed curves. The blue line indicates ordinary pairing between p_0 (state 1) and $-p_0$ (state 2) electrons corresponding to the zero total pair momentum. The green line indicates Néel pairing between p_0 (state 1) and $-p_0 + Q_{1D}$ (state 3) corresponding to the total pair momentum Q_{1D}. The picture is adopted from Ref. [34].

Figure 1b plots the spatially resolved spin-triplet pairing amplitude in the S/AF bilayer. A clear imprinting of the AF Néel ordering is seen on the triplet pairing amplitude in the direction parallel to the interface: an alternating sign of the correlations in the S layer is clearly visible. This perfect picture is disturbed in the direction perpendicular to the interface due to the absence of the translational invariance in this direction. We will get back to physical reasons of the disturbance in Section 4 of this review.

The physics related to the proximity-induced Néel triplet correlations can be also described in the framework of the two-sublattice quasiclassical theory in terms of the Eilenberger equation, which was developed in Ref. [34].

2.2 Qualitative physical picture of the Néel triplets' origin

What is the physical origin of the Néel Cooper pairs? The essential physics is captured already within a one-dimensional (1D) model[34] considering 1D AF covered by 1D superconductor. Therefore, the electron wavevector bears only one component which is along the interface.

In the absence of the antiferromagnet the normal-state electronic dispersion of S-metal can be depicted as in figure 2 with a Brillouin zone (BZ) $pa \in [-\pi, \pi]$, where a is the lattice constant. Within this single-sublattice dispersion the Néel magnetic order in AF causes scattering between electronic states that differ by the wavenumber $Q_{1D} = \pi/a$ (so-called Umklapp scattering[35–37]) at the S/AF interface. Thus, the AF converts conventional spin-singlet pairing between electrons with momenta $+p_0$ and $-p_0$ at the Fermi surface (blue line in figure 2) into the Néel spin-triplet pairing between, for example, $+p_0$ and $-p_0 + Q_{1D}$ (green line in figure 2). In real space such a pairing changes sign from a site to its nearest neighbor similar to the Néel order with the wavenumber Q_{1D}. The antiferromagnetic gap opening has been disregarded in the present simplified figure.

Strictly speaking, to describe the whole S/AF system, we should use a unit cell with two sites in it, corresponding to two sublattices of the antiferromagnet with opposite magnetizations. Within this two-sublattice picture, we now have two bands in the electronic dispersion. What appeared as pairing between $+p_0$ and $-p_0 + Q_{1D}$ states in the single-sublattice picture is actually pairing between the $+p_0$ state from one band with the $-p_0$ state from the other band, as depicted in figure 2. Therefore, we conclude that the Néel pairing is the interband pairing.

2.3 Dependence of the Néel triplet pairing on the chemical potential

Due to its interband origin the Néel triplet pairing is very sensitive to the value of the chemical potential in the material, where it is induced. It is in sharp contrast with the usual triplet pairing induced by the proximity effect at S/F interfaces, which is insensitive to the value of the chemical potential because of its intraband nature. To see the dependence of the Néel pairing on the chemical potential, let us have another look at figure 2. Taking into account that p_0 is defined from the condition $\xi_+(p) = -2t \cos p_0 a - \mu = 0$ one immediately obtains that $\xi_1 - \xi_{3'} = 2\mu$. That is, the energy difference between states 1 and $3'$ grows with μ, thus reducing the efficiency of pairing. This qualitative picture was supported in Ref. [34] by strict calculations performed in the framework of the two-sublattice quasiclassical theory.

Figure 3 represents the results of calculation of the Néel triplet amplitude F_A^t in a thin superconductor proximitized by an AF insulator. Such a thin-film superconductor with the thickness $d_S \ll \xi_S$, where ξ_S is the superconducting coherence length, can be considered as a homogeneous superconductor under the influence of an effective exchange field of the Néel type $\boldsymbol{h}_{\text{eff}}$,[13, 34] which accounts for the influence of the AF insulator on the superconducting film. In figure 3 the Néel triplet amplitude is plotted for different values of the chemical potential μ of the superconductor and different amplitudes of the effective exchange field $h_{\text{eff}} \equiv |\boldsymbol{h}_{\text{eff}}|$. It is clear that for a given value of h_{eff} the Néel triplet amplitude indeed weakens upon increase in μ. The amplitude of conventional triplet correlations induced in the same thin-film superconductor by proximity to a ferromagnetic insulator producing the effective exchange field of the same amplitude h_{eff} (homogeneous, not Néel) is also shown for comparison (see purple curve in figure 3).

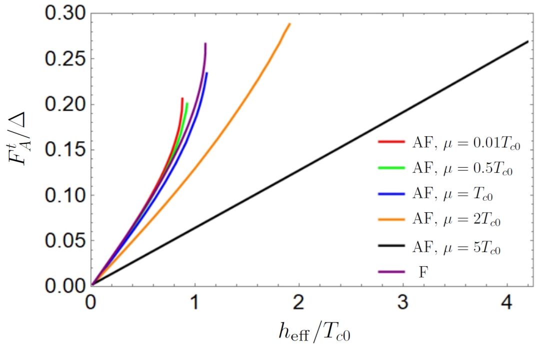

Figure 3. Anomalous Green's function of the Néel triplet correlations as a function of h_{eff} for different values of μ. Each line ends at the critical value of h_{eff} corresponding to the full suppression of superconductivity. T_{c0} is the critical temperature of the superconductor without proximity to a magnet. The picture is adopted from Ref. [34].

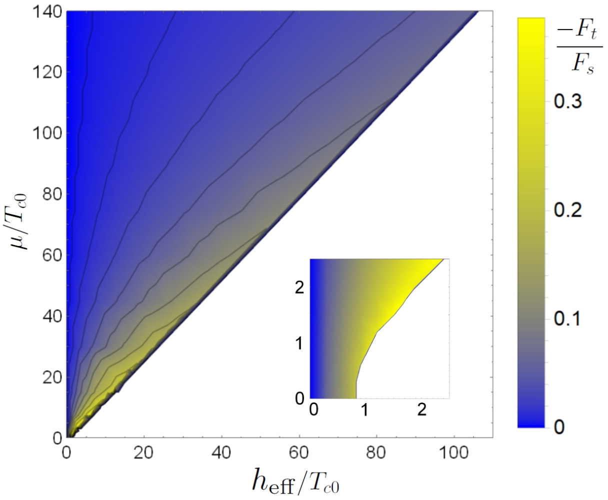

Figure 4. Amplitude of the triplet correlations relative to the singlet amplitude as function of h_{eff} and μ at $T \to T_c$. Inset: region $(h_{\text{eff}}, \mu) \sim T_{c0}$ on a larger scale. The picture is adopted from Ref. [38].

The weakening of the Néel triplet correlations with increasing chemical potential does not mean that they are completely suppressed at high values of the chemical potential ($\mu \gg T_{c0}$), when the filling factor in the superconductor is far from half filling of the conduction band. Here T_{c0} is the critical temperature of the superconductor in the absence of the proximity to the AF. The amplitude of the Néel triplet correlations increases with increasing effective exchange field h_{eff}, as it is seen from figure 3. It was shown in Ref. [38] that at $(h_{\text{eff}}, \mu) \gg T_{c0}$ the amplitude of the Néel triplet correlations is only determined by the ratio h_{eff}/μ and reaches its maximal value at the line $h_{\text{eff}}/\mu = \text{const} \approx 0.8$. This tendency is demonstrated in figure 4. For larger values of this parameter the superconductivity in the system is fully suppressed.

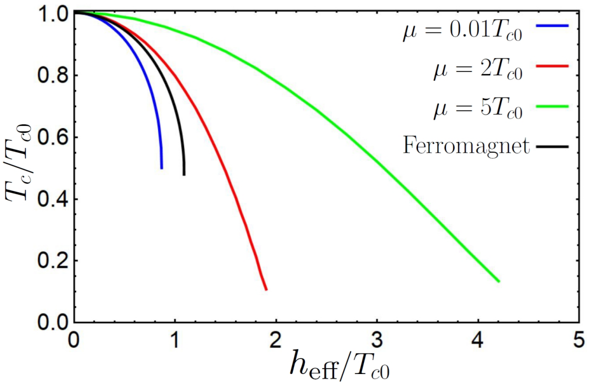

Figure 5. Critical temperature of the S/AF bilayer as a function of $h_{\rm eff}$ for different values of μ. Black line represents the dependence $T_c(h_{\rm eff})$ for an S/F interface with a ferromagnetic insulator producing the same value of the effective exchange field (but homogeneous, not staggered) in the superconductor. The picture is partially overlapped with an analogous picture from Ref. [34].

2.4 Suppression of the critical temperature of thin-film S/AF bilayers by the Néel triplets

Now we demonstrate that the Néel triplet correlations suppress the superconductivity at S/AF interfaces and, in particular, they suppress the superconducting critical temperature of thin-film superconductors proximitized by antiferromagnetic insulators. The effect is analogous to the well-known suppression of superconductivity by proximity-induced triplets at S/F interfaces.[4] Again we discuss a thin-film superconductor with $d_S \ll \xi_S$ in proximity to an antiferromagnetic insulator.

The dependence of the critical temperature of the S/AF bilayer on the effective exchange field is presented in figure 5 for different values of the chemical potential. The critical temperature is indeed suppressed by the staggered exchange field $h_{\rm eff}$. The efficiency of suppression by the staggered field is of the same order, and even higher, as the suppression by the ferromagnet with the same absolute value of the exchange field. The stronger suppression of the superconductivity by the staggered exchange as compared to the uniform ferromagnetic exchange field is explained by the presence of the antiferromagnetic gap at the Fermi surface, which prevents electronic states inside this gap from superconducting pairing. The superconductivity suppression for a given $h_{\rm eff}$ becomes weaker for larger values of the chemical potential, what is explained by weakening of the Néel triplet correlations upon increase of μ.

2.5 Proximity effect produced by canted antiferromagnets: mixture of Néel and conventional triplets

Following to Ref. [39] we would like to discuss, what happens with the proximity effect in heterostructures composed of superconductors and canted antiferromagnets. We consider a bilayer structure consisting of an insulating AF with canted sublattice magnetizations exchange coupled to an adjacent S. The sketch of the system is shown in figure 6. The canting angle is θ_t. For $\theta_t = 0$ the considered AF becomes a collinear antiferromagnet with the axis of magnetic moments along the x-direction. As we increase the value of θ_t, the canted-AF acquires a net magnetization along the y-direction. So the canted-AF can be decomposed into an antiferromagnetic component (along the x-axis) and a ferromagnetic component (along the y-axis).

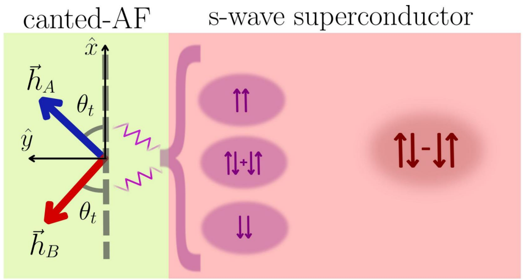

Figure 6. Sketch of the system and key physics of the proximity effect at S/canted AF interfaces. Equal-spin and zero-spin triplet correlations are generated in a conventional s-wave spin-singlet superconductor when it is interfaced with a canted antiferromagnet (canted-AF). The equal-spin triplet correlations result from the intrinsic noncollinearity between the two AF sublattice magnetizations. The canting angle θ_t allows one to vary the magnet from being a collinear AF ($\theta_t = 0$) to a ferromagnet ($\theta_t = \pi/2$). The picture is redrawn after Ref. [39].

Chourasia *et al.* [39] investigated the spin-triplet correlations and calculated the critical temperature of the S as functions of the canting angle in the AF, which allows us to continuously tune the AF from its collinear antiparallel state to that effectively becoming in F. In general, the vector amplitude of the triplet superconducting correlations induced in the S-layer by proximity to the AF can be written as $\mathbf{F}_j^t = F_j^{t,x}\mathbf{e}_x + F_j^{t,y}\mathbf{e}_y + F_j^{t,z}\mathbf{e}_z$. It always has a component aligning with the local exchange field whether the magnetization of a magnet (either ferromagnet or antiferromagnet) is homogeneous or inhomogeneous. If the magnetization is inhomogeneous, other components, not coinciding with the direction of the local exchange field, appear.[3] In the considered case the magnetization is obviously inhomogeneous due to canting. For this reason all three components of the triplet vector are nonzero.

The dependence of these spin-triplets on the canting angle is presented in figure 7. At $\theta_t = 0$ only $F^{t,x}$ component is nonzero. It corresponds to the pure Néel triplet order discussed above. The Néel structure of this component was demonstrated explicitly.[39] This component decreases as θ_t goes from 0 to $\pi/2$ (figure 7b) and vanishes at $\theta_t = \pi/2$ because the Néel triplets are absent in the purely ferromagnetic state. It is also seen that the amplitude of this component decreases as μ increases in agreement with the general dependence of the Néel triplets on the chemical potential, discussed above. Here the chemical potential is determined via the filling factor f, which is the fraction of filled electronic states in the system: $f = 0.5$ (half-filled band) corresponds to $\mu = 0$.

The component $F^{t,y}$ increases with the canting angle and it appears to be caused primarily by the net magnetization (figure 7c). It was directly checked that it is

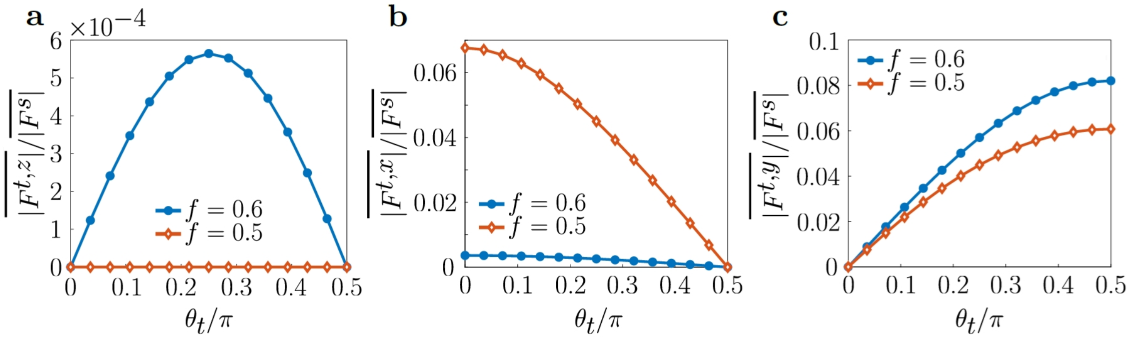

Figure 7. **a**, **b**, **c** – Variations of the triplet correlations with the canting angle θ_t for different filling factors $f = 0.5$ ($\mu = 0$) and $f = 0.6$ ($\mu/T_{c0} \approx 65$). These panels show the average magnitudes of the normalized spin-triplet correlation $F^{t,z}$ (panel a), $F^{t,x}$ (panel b), and $F^{t,y}$ (panel c). The averages are taken over all superconducting sites and they are denoted via an overhead bar. The picture is adopted from Ref. [39].

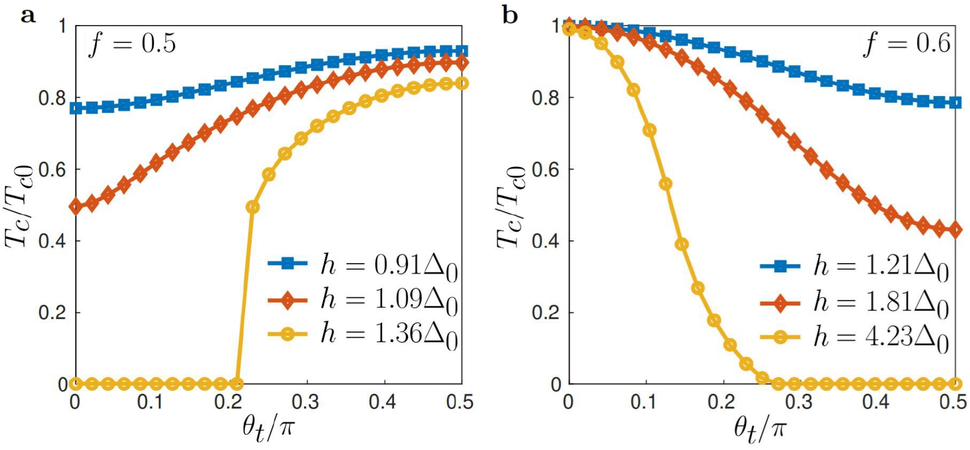

Figure 8. **a**, **b** – Normalized critical temperature T_c vs. canting angle θ_t for the filling factors $f = 0.5$ (panel a) and $f = 0.6$ (panel b) considering different values of the antiferromagnetic exchange field h. Δ_0 is the zero-temperature superconducting order parameter of the same superconductor without the AF-layer. The picture is adopted from Ref. [39].

a conventional triplet component without the Néel structure. It is maximal in the purely ferromagnetic state. $F^{t,z}$ is also found to be of the Néel type (figure 7a). It appears due to the noncollinearity of two sublattices. Its Néel character can be understood in terms of this noncollinearity. Hopping from one lattice site to the next, the angle between the spin-splitting at the site and its direct neighbors changes its sign. It is interesting that it vanishes at $\mu = 0$ ($f = 0.5$) for all canting angles. The physical reason is that for $\mu \approx 0$ the antiferromagnetic gap opens in the superconductor in the vicinity of the normal state Fermi surface. In this case the most important contribution to the pairing correlations is given by the electronic states at the edge of the gap. They correspond to $\xi_\pm \approx 0$, what means that the electrons are practically fully localized at one of the sublattices. Consequently, they only feel the magnetization of the corresponding sublattice, which is homogeneous. As a result, the noncollinearity does not affect the z-component or the triplet correlations. However, for non-zero μ (away from the half-filling case) $F^{t,z}$ increases from zero to a finite value as we go from a collinear antiferromagnetic alignment to the maximal noncollinearity between the sublattice magnetic moments, and then it decreases back to zero for the ferromagnetic alignment (figure 7a).

As it was already discussed, the critical temperature of superconductor/magnet heterostructures is suppressed by triplet correlations, both of conventional type and the Néel type. Therefore, it is natural to expect that the critical temperature of the S/AF bilayers with canted antiferromagnets is always suppressed with respect to the critical temperature of the isolated superconductor T_{c0}. It was found [39] that it is indeed the case. However, the physics of the suppression is very interesting. In the framework of our review here we encounter the first manifestation of the crucial dependence of the Néel triplets on the chemical potential and its physical consequence. It was obtained that the dependence of the critical temperature on the canting angle θ_t is opposite near half-filling and far from half-filling. It is demonstrated by figure 8 composed for $f = 0.5$ and $\mu = 0$ (panel a), and for $f = 0.6$ and $\mu \approx 65T_{c0}$ (panel b). It is found that for $\mu = 0$ the T_c value increases with θ_t while it manifests the opposite dependence for $\mu \neq 0$.

For the case $\mu = 0$ presented in figure 8a, a strong generation of the Néel triplets due to the interband pairing leads to the maximal T_c suppression at $\theta_t = 0$. Since the T_c suppression is stronger for the pure AF case ($\theta_t = 0$) than for the pure F case ($\theta_t = \pi/2$), the T_c value increases with θ_t. For the case of $f = 0.6$ ($\mu \gg T_{c0}$) and $h \sim T_{c0}$ ($h \equiv |\boldsymbol{h}|$), the Néel triplets generation by the antiferromagnetic order is much weaker. On the other hand, the ordinary spin-triplets generation by a ferromagnet remain of the same order of magnitude as for $f = 0.5$. Thus, T_c is the largest for $\theta_t = 0$ and it decreases with θ_t.

3 Influence of impurities on the Néel triplets and on superconductivity in S/AF heterostructures

In this section we discuss how the superconductivity in S/AF heterostructures is influenced by conventional nonmagnetic impurities and what is the role of the Néel triplets in this physics. Here we will have the second example of the crucial influence of the chemical potential on the physics of S/AF heterostructures.

3.1 Néel triplets and impurities

First of all, we discuss how the Néel triplets behave in the presence of impurities. It was shown [34] that near half-filling state nonmagnetic disorder destroys the Néel spin-triplet correlations. The physical reason of the suppression of the Néel triplets by the nonmagnetic disorder is their interband nature. At the same time, at $\mu \gg T_{c0}$ the interband Néel triplet pairing is suppressed. However, the Néel triplet correlations can be essential even at large values of μ, as it was demonstrated in Refs. [38, 39] and was discussed above in this review. In this case all pairing correlations are completely intraband, as it is shown in figure 9a. It should be noted that the normal state eigenvectors of the electronic band crossed by the Fermi level represent a mixture of sign-preserving and sign-flipping components between the A and B sites of the same unit cell:

$$\begin{pmatrix} \hat{\psi}^A_{\boldsymbol{i}\sigma} \\ \hat{\psi}^B_{\boldsymbol{i}\sigma} \end{pmatrix} (\boldsymbol{p}) = \left[C_{p\sigma} \begin{pmatrix} 1 \\ 1 \end{pmatrix} + C_{f\sigma} \begin{pmatrix} 1 \\ -1 \end{pmatrix} \right] e^{\boldsymbol{i}\boldsymbol{p}\boldsymbol{i}}, \quad (3)$$

where

$$C_{p(f)\sigma} = \frac{1}{2} \left(\sqrt{1 + \frac{\sigma h_{\mathrm{eff}}}{\mu}} \pm \sqrt{1 - \frac{\sigma h_{\mathrm{eff}}}{\mu}} \right) \quad (4)$$

are the sign-preserving (flipping) amplitudes of the eigenvectors. Due to the presence of the sign-flipping component of the eigenvectors and its spin sensitivity, the singlet homogeneous pairing between $\boldsymbol{p}$ and $-\boldsymbol{p}$ states at the Fermi level (see figure 9a) is inevitably accompanied by the Néel sign-flipping triplet component. As it can be seen from Eq. (4) the amplitude of the sign-flipping mixture is controlled by the ratio h_{eff}/μ and it is suppressed as μ increases, what is in agreement with the dependence of the Néel triplets on the chemical potential, presented in Section 2.3.

It is natural to expect that the s-wave intraband triplets are not sensitive to the influence of nonmagnetic impurities. Our calculations, performed in the framework of the non-quasiclassical Green's functions approach, originally presented in Ref. [38] confirm these expectations. The dependencies of the Néel triplet amplitudes on the nonmagnetic impurity inverse scattering time τ_s^{-1} are demonstrated in figure 10. It is seen that at $\mu = 0$ the amplitude of the Néel triplet correlations is suppressed by impurities, as it was found in Ref. [34]. At rather large parameter $\mu = 7.5 T_{c0}$ we clearly see no suppression. Instead, a weak increase of the Néel triplet amplitude is observed. We cannot definitely say what is the reason for this weak increase. Probably it is related to the influence of impurities on the normal-state density of states (DOS).

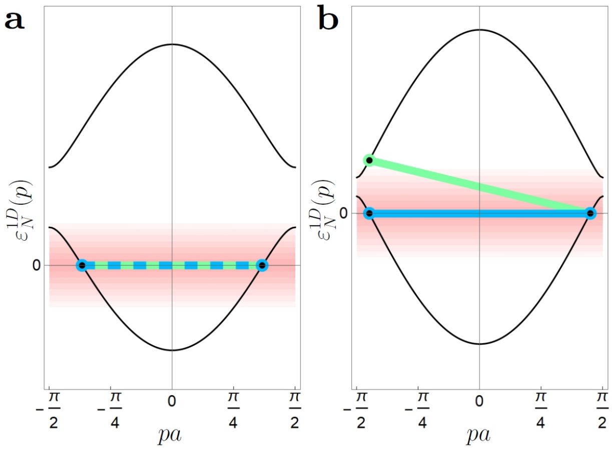

Figure 9. **a**, **b** – Electron dispersion of the normal-state in the reduced Brillouin zone (BZ) $pa \in [-\pi/2, \pi/2]$. For simplicity of visualization a 1D system dispersion $\varepsilon_N^{1D} = \mp\sqrt{\xi^2(p) + h_{\mathrm{eff}}^2} - \mu$ is demonstrated instead of a real dispersion ε_N^{3D}. Here we take into account the opening of the antiferromagnetic gap due to h_{eff}. **a** – Case of large μ. The electronic states in the vicinity of the Fermi surface $\varepsilon_N^{1D} = 0$ allowed for pairing (pink region) do not involve the second electronic branch. Only $(\boldsymbol{p}, -\boldsymbol{p})$ intraband singlet and intraband Néel triplet pairs are present (dashed blue-green). **b** – Case of small μ for comparison. Electronic states belonging to the both branches are present in the vicinity of the Fermi surface and are allowed for pairing. Both intraband singlet (blue) and interband Néel triplet pairs (green) exist. The picture is adopted from Ref. [38].

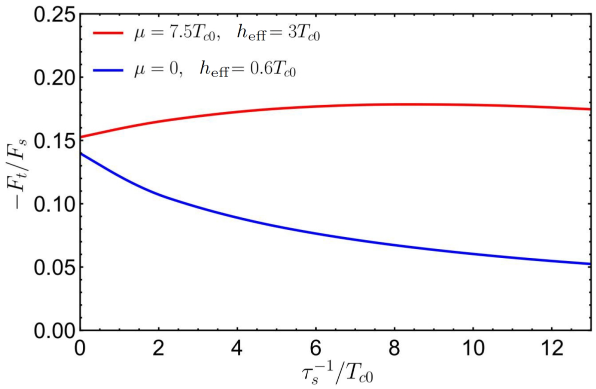

Figure 10. Amplitude of the triplet correlations relative to the singlet amplitude as a function of the inverse impurity scattering time for a superconductor in the presence of the Néel-type effective exchange field h_{eff}. Different curves correspond to different values of the chemical potential μ.

3.2 Depairing effect of nonmagnetic impurities in S/AF heterostructures at large chemical potentials

What happens with the critical temperature of thin-film S/AF bilayers in the presence of impurities? Based on the results discussed in the previous subsection one can conclude that T_c should be enhanced with impurity scattering strength at small chemical potentials because of weakening the triplets, which are generated at the expense of singlets. It is indeed the case, as it is shown in the next subsection. But what we can expect at large μ? Is the critical temperature only negligibly sensitive to impurities? The answer is that at large chemical potentials the critical temperature is suppressed by nonmagnetic impurities quite strongly. The mechanism of the suppression is not related to the Néel triplets. The amplitude of the wave functions of electrons is different for A and B sublattices [see Eq. (3)]. Physically it is because of the fact that for an electron with spin up it is energetically favorable to be localized on the B sublattice and for an electron with spin down — on the A sublattice. Thus, this sublattice-spin coupling in the presence of the Néel-type exchange field gives an effective magnetic component to the non-magnetic impurities. And it is well-known that magnetic impurities do suppress superconductivity.[40] This mechanism of superconductivity suppression by nonmagnetic impurities was originally discussed for antiferromagnetic superconductors.[17] Then it was realized that it also works for S/AF heterostructures,[18, 19] where an appropriate quasiclassical theoretical formalism taking into account the destroying action of nonmagnetic impurities was developed[18] and the suppression of the critical temperature of S/AF bilayers with metallic antiferromagnets due to the nonmagnetic impurities was found.[19]

3.3 Dependence of the critical temperature of S/AF heterostructures on impurities: enhancement vs suppression

The influence of nonmagnetic impurities on the critical temperature of thin-film S/AF bilayers, which can be effectively modelled as superconductors in a homogeneous effective Néel exchange field h_{eff}, in the full range of parameters of the bilayer was considered in Ref. [38].

We start with the discussion of two limiting cases. Figures 11 and 12 demonstrate the critical temperature of the S/AF bilayer as a function of the inverse impurity scattering time τ_s^{-1}. The results shown in figure 11 are calculated at $\mu = 0$ and represent a typical example of the dependence in the regime when the interband Néel triplets are strong and play the role of the main depairing mechanism, and the impurities do not really work as effectively magnetic. It can be seen that at $h_{\text{eff}} \neq 0$ the critical temperature grows with the disorder strength or even appears at some nonzero τ_s^{-1}. This behavior is explained by the presence of the Néel triplets, which suppress the critical temperature of the singlet superconductivity. In the clean limit $\tau_s^{-1} = 0$ their amplitude is the maximal. Due to the interband nature of the Néel pairing they are gradually reduced with impurity strength and, consequently, the critical temperature grows.

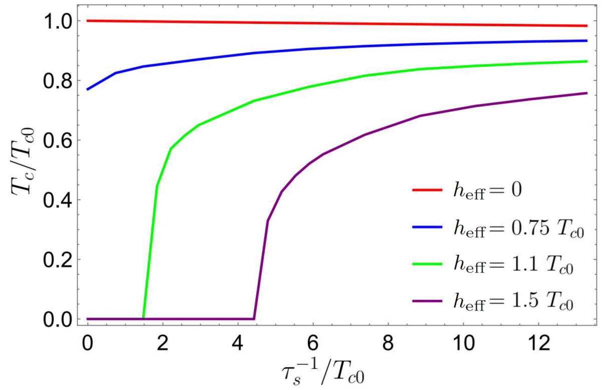

Figure 11. Dependence of T_c on τ_s^{-1} at $\mu = 0$ for different effective exchange fields h_{eff}. T_c is normalized to the value of the critical temperature T_{c0} of the isolated S-film. The picture is adopted from Ref. [38].

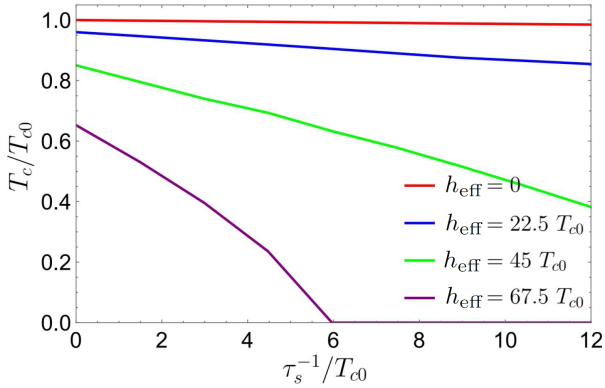

Figure 12. Dependence of T_c on τ_s^{-1} at $\mu = 150\,T_{c0}$ for different effective exchange fields h_{eff}. The picture is adopted from Ref. [38].

Figure 12 corresponds to $\mu = 150\,T_{c0}$. It represents the opposite limit when the interband Néel triplets are suppressed. Intraband Néel triplets are still there and they suppress superconductivity of the bilayer with respect to the case of an isolated superconductor, especially at large values of h_{eff}, as it is seen at $\tau_s^{-1} = 0$. However, the intraband Néel triplets are not sensitive to nonmagnetic impurities. The dependence $T_c(\tau_s^{-1})$ is dominated by the impurity suppression.

Now, after considering the limiting cases we discuss the effect of nonmagnetic impurities on the superconductivity of the S/AF hybrids in the entire range of parameters. Figure 13 represents the behavior of the critical temperature in the $\tau_s^{-1} - \mu$ plane for a given $h_{\text{eff}} = 2.25 T_{c0}$. Front and back sides of the image correspond to the considered opposite limits. The front side is the limit of small μ, where Néel triplets dominate and, consequently, superconductivity is restored with increase in impurity strength. The back side corresponding to large μ, represents the suppression of superconductivity by nonmagnetic impurities. For intermediate μ values there is a crossover between them. In particular, for a certain range of μ a nonmonotonic dependence $T_c(\tau_s^{-1})$ is ob-

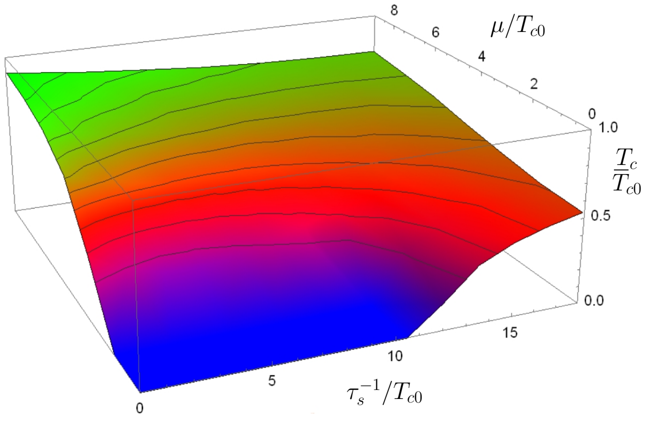

Figure 13. Dependence of the critical temperature T_c on τ_s^{-1} and μ at $h_{\text{eff}} = 2.25T_{c0}$. The picture is adopted from Ref. [38].

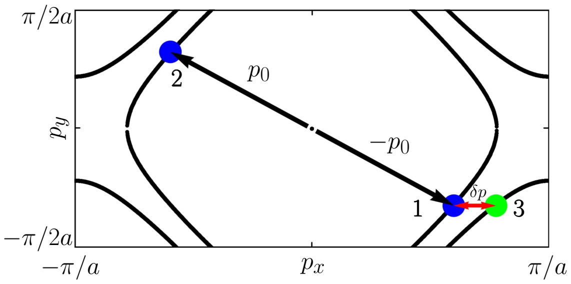

Figure 14. Brillouin zone and Fermi surface (black curves) of the AF layer. Zero-momentum Cooper pair between electrons 1 and 2 is schematically shown by black arrows. There is also Néel-type finite-momentum triplet pairing between electrons 2 and 3, which is produced from electron 1 due to the Umklapp reflection process from the S/AF interface. The total momentum δp of the pair (2 and 3) is shown by the red arrow. The picture is adopted from Ref. [76].

served. The initial suppression of T_c is changed by some growth. This is because the singlet superconductivity is suppressed by the impurities more rapidly than the Néel triplets. This behavior is in sharp contrast with the behavior of a F/S bilayer, where the critical temperature is not sensitive to the *nonmagnetic* impurity concentration, and the *magnetic* impurities suppress the superconductivity.[40] Moreover, the properties of S/F bilayers is mainly not sensitive to the deviation from half-filling of the electronic spectrum unlike from S/AF hybrids.

It is worth noting that all the results discussed above are valid for the case of relatively weak disorder, which can be considered in the Born approximation. The issue about the influence of the strong disorder on superconductivity in S/AF heterostructures is yet to be explored. For the case of conventional s-wave superconductors it is known that a strong disorder can lead to a metal–insulator transition in the normal state, to the appearance of a pseudogap in spectrum and larger spatial fluctuations of superconductive pairing, what results in increased Δ/T_c ratio.[41–45] Furthermore, Anderson localization and phase fluctuations, are more pronounced in low-dimensional structures, leading to the suppression of superconductivity. At the same time, the disorder can also result in a remarkable enhancement of superconductivity.[46–52] The stronger disorder increases spatial inhomogeneity, which enhances the local pairing correlations and superconducting gap, comparing with the clean system. Disorder-related effects are assumed to be responsible for a large increase of the critical temperature in the recently discovered superconducting NbSe_2 monolayers. Theoretical analysis attributes the enhancement to the disorder-induced multi-fractal structure of the electronic wave functions. Which of the listed possibilities are relevant to S/AF heterostructures is to be studied. This prospect for future work is especially interesting in view of the opposite effects of the weak disorder on superconductivity near half-filling and away from half-filling, what can make the physical picture of the effect of the strong disorder even richer.

4 Finite-momentum Néel triplets

Triplet pairs, originated from the singlet-triplet conversion in homogeneous superconductors under the action of a Zeeman field, are usually zero-momentum pairs,[9] what means that their wave functions are uniform in real space. However, in some narrow regions of parameters an inhomogeneous superconducting state produced by singlet and triplet pairs with finite momentum of the pair, the so-called Fulde-Ferrel-Larkin-Ovchinnikov (FFLO) state, was predicted.[53,54] One of the important properties of the triplet pairs generated at F/S interfaces, where the translational invariance is lost, is that the zero-momentum pairs, entering the ferromagnetic region from the superconductor, inevitably acquire a finite momentum of the pair[55,56] due to the fact that the spin-up and spin-down electrons forming a pair have opposite potential energies in the macroscopic exchange field of the ferromagnet. Thus, the electrons residing at the same energy (at the Fermi surface) have not strictly opposite momenta in the ferromagnet (the absolute values of their momenta are different) and the pair as a whole has nonzero total momentum. The finite momentum is acquired both by singlet and triplet pairs, what allows us to refer to such state as a mesoscopic analogue of the FFLO superconducting state.[53,54] The finite momentum, which the Cooper pair acquires in the exchange field of the ferromagnet, makes the pairing wave function oscillating. The resulting phase change across the ferromagnetic layer is responsible for the π-junction effects,[4,55,57–61] which are widely used now in the superconducting electronics.[62–64] The interference of the incident and reflected oscillating wave functions determines the oscillatory phenomena of the critical temperature T_c versus the F-layer thickness in bilayers and multilayers, which have been widely studied both theoretically[65–70] and experimentally.[71–75]

Naively, one does not expect that a Cooper pair penetrating into the antiferromagnet from the superconductor possesses a finite total momentum because (i) the average value of the exchange field in the antiferromagnet is zero, (ii) the quasiparticles spectrum is spin-degenerate and, therefore, (iii) spin-up and spin-down electrons, forming the pair, should have opposite momenta with equal absolute values $\boldsymbol{p}_\uparrow = -\boldsymbol{p}_\downarrow$. In its turn, that means zero total momentum of the pair and, as a result, absence of the oscillations of the pair amplitude. However, it was shown that in the absence of the translational invariance in S/AF heterostructures (*i. e.*, at S/AF interfaces or single impurities) the finite-momentum Néel triplet pairing occurs.[76,77] It was demonstrated theoretically that the finite-momentum Néel triplet correlations at S/AF interfaces result in the oscillating dependence of the critical temperature on the thickness of AF-film.[76] There are a number of experimental works, where the critical temperature of S/AF bilayers with metallic antiferromagnets has been measured as a function of the AF thickness and the oscillating behavior was observed.[20–22] At the same time, in the regime, when the Néel triplets can be disregarded, this dependence has been calculated and no oscillations were reported.[19] Thus, oscillations of the critical temperature of S/AF bilayers can be viewed as a signature of the presence of finite-momentum Néel-type triplet correlations in the hetero-structure. In two following subsections we consider the physical nature of the finite-momentum Néel triplet pairing and discuss how it manifests in the critical temperature of S/AF bilayers with metallic antiferromagnets.

4.1 Physical mechanism of the finite-momentum Néel triplet pairing

In Section 2.2 we discussed the qualitative mechanism of the Néel triplet pairing. It was shown that the Néel pairing is pairing of electrons having the momenta $\boldsymbol{p}$ and $-\boldsymbol{p} + \boldsymbol{Q}$, where $\boldsymbol{Q}$ is the reciprocal lattice vector due to the periodicity enforced by the AF ordering. In the 2D case it is $\boldsymbol{Q} = (\pi/a, \pi/a)$. In real space this pairing manifests itself as the atomic-scale oscillations of the pair amplitude: it flips its sign from one site to its nearest neighbor. But if we only monitor on-site Néel triplet pairs for one of the sublattices, we see that the amplitude is homogeneous. Now let us consider a situation with broken translational invariance in the system. The simplest case is a plane S/AF interface. Previously we discussed mainly effectively homogeneous systems such as thin-film superconductors proximitized by AF insulators, which can be considered as homogeneous superconductors under the action of the Néel effective exchange field h_{eff}. The spatial dependence of the proximity effect in the direction perpendicular to the interface was neglected due to the small thickness of the S-film in the transverse direction. The only exception is figure 1 of this review, where this simplification was not used. It is clear that the perfect Néel structure, which we see along the interface, is violated in the direction perpendicular to the interface. Even if we monitor the on-site Néel pairing at one of the sublattices, the corresponding amplitude has some oscillations. It is a signature of the formation of finite-momentum Néel triplet pairs due to scattering events at the interface. Now let us explain the mechanism of such pairing in more details.

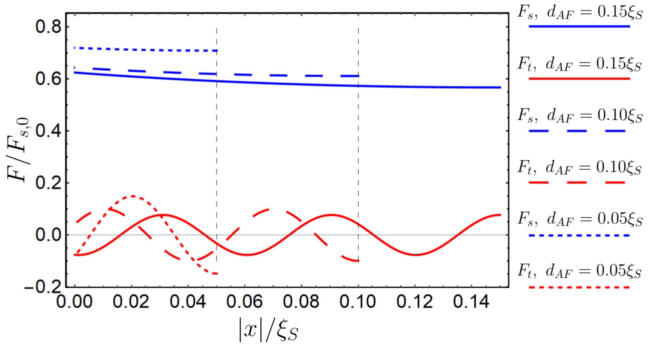

Figure 15. Dependence of the A-sublattice triplet correlations amplitude F_t (red curves) and the singlet amplitude F_s (blue curves) for the normal to the S/AF interface trajectory $v > 0$ on the distance from the S/AF interface inside the AF layer. Different curves correspond to different thicknesses d_{AF} of the AF layer. Each of the curves ends at the distance corresponding to the impenetrable edge of the AF layer. $F_{s,0}$ is the singlet amplitude in the absence of the AF layer. The picture is adopted from Ref. [76].

If we consider a plane interface, which breaks the translational invariance along the x-direction, then it is convenient to choose the Brillouin zone (BZ) as shown in figure 14. Due to the doubling of the unit cell BZ is compressed twice in the lateral direction along the y-axis. As a result, additional branches of the Fermi surface appear in the reduced BZ. Please note that such additional branches of the Fermi surface do not occur in the 1D case, considered in Section 2.2. Let us consider an electron (p_{x1}, p_y) incoming to the S/AF interface from the AF side (marked by 1 in figure 14). Because of Umklapp scattering at the the S/AF interface this electron can be reflected as electron 3 from another branch, corresponding to the momentum (p_{x3}, p_y) (for the plane interface the component of the electron momentum p_y along the interface is conserved). That is why the electron 2 with momentum $(-p_{x1}, p_y)$ can form not only a singlet zero-momentum Cooper pair with the electron 1, but also a Néel-type triplet pair with the electron 3, which has a finite total momentum $\delta p = |p_{x3} - p_{x1}|$. The normal-state electron dispersion in the reduced BZ takes the form

$$\varepsilon = -\mu_{AF} + \sqrt{h^2 + 4t^2(\cos p_x a + \cos p_y a + \cos p_z a)^2}.$$

From this dispersion relation and the condition that $\varepsilon = 0$ at the Fermi surface we obtain

$$\delta p = \frac{\sqrt{\mu_{AF}^2 - h^2}}{ta\,\sin p_x a}.$$

The last expression can be rewritten in terms of the electron Fermi velocity $v_{F,x} \equiv v = \partial\varepsilon/\partial p_x = 2ta\sin(p_x a)$ at $\mu_{AF} = h = 0$ as $\delta p = 2\sqrt{\mu_{AF}^2 - h^2}/v$. The main contribution to the oscillations of the critical temperature is given by the normal trajectories with $v_{F,x} \approx v_F$ and then the oscillation period takes the form

$$L_{\text{osc}} = \frac{\pi v_F}{\sqrt{\mu_{AF}^2 - h^2}}. \tag{5}$$

Figure 15 shows some typical examples of the spatial distribution of the on-site singlet and triplet correlations inside the AF layer at the A-sublattice. We see that

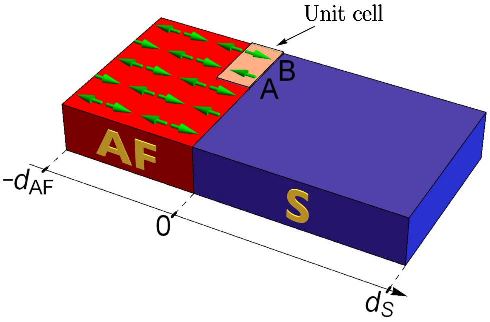

Figure 16. S/AF bilayer with a finite-width metallic AF. Staggered magnetization of the AF layer is schematically depicted by arrows. The unit cell containing two sites belonging to A and B sublattices is also shown. The picture is adopted from Ref. [76].

the triplet correlations oscillate inside the antiferromagnet [the period of these oscillations is in agreement with Eq. (5)], while the singlet correlations just decay without oscillations, unlike the case of S/F heterostructures, where both singlet and triplet correlations manifest oscillations with the same period inside the ferromagnet. The reason is that according to our qualitative consideration only Néel pairs can have finite momentum of the described physical origin.

4.2 Oscillations of the critical temperature of S/AF bilayers

Now we will discuss the effect which oscillations of the Néel triplet correlations have on the critical temperature of S/AF bilayers with metallic antiferromagnets. The sketch of the system is presented in figure 16. In systems with finite-width layers these oscillating correlations can experience constructive or destructive interference due to the reflections from the impenetrable edge of the AF layer. This leads to the oscillating dependence of the Néel triplet correlations amplitude on the width d_{AF} of AF-layer, what, in its turn, makes the critical temperature of the bilayer also an oscillating function of d_{AF}.

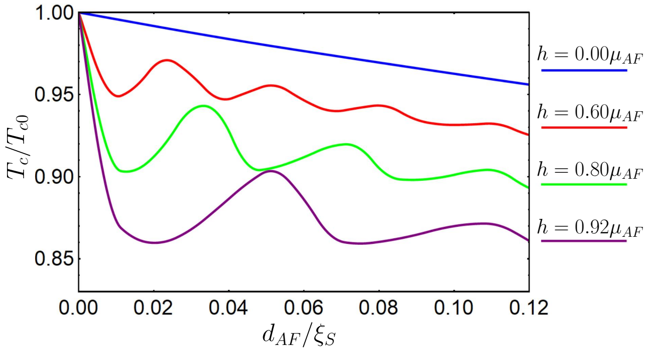

Figure 17. Critical temperature of the S/AF bilayer as a function of the AF layer thickness d_{AF}, calculated for $d_S = 1.5\xi_S$. The picture is adopted from Ref. [76].

Such behavior of the critical temperature was investigated in Ref. [76]. Figures 17-19 show the critical temperature as a function of d_{AF} for different values of the thickness d_S of the S layer. Different curves in each figure correspond to the different exchange fields h of the AF layer. In all three figures we can see the superconductivity suppression is accompanied by the oscillations of the critical temperature. The amplitude of the oscillations grows with the value of the exchange field, and its period is described well by Eq. (5) regardless of the thickness of the superconductor. As the S layer gets thinner, the influence of the proximity effect on the superconductor increases, which leads to a stronger suppression of the critical temperature and a larger amplitude of the oscillations. To see this we can compare figures 17 and 18. In figure 18 corresponding to smaller d_S the amplitude of the oscillations is higher. This is because of larger amplitude of the triplet wave function reflected from the impenetrable edge of the AF. However, for the thinnest S layer (figure 19) the T_c oscillations are weakly pronounced. This is explained by the fact that the amplitude of the oscillating Néel triplets inside the AF layer (and, consequently, the amplitude of the T_c oscillations) is greatly suppressed in this case together with superconductivity.

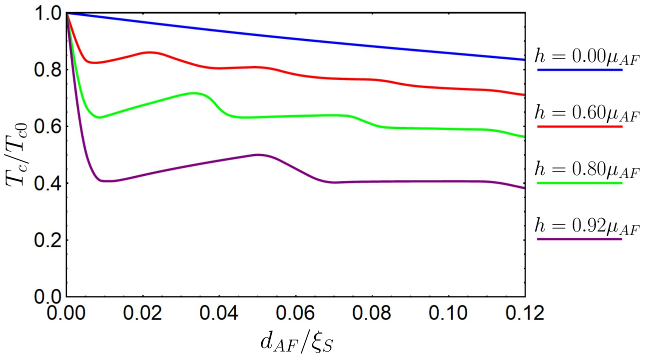

Figure 18. The same as figure 17 but calculated for $d_S = 0.75\xi_S$. The picture is adopted from Ref. [76].

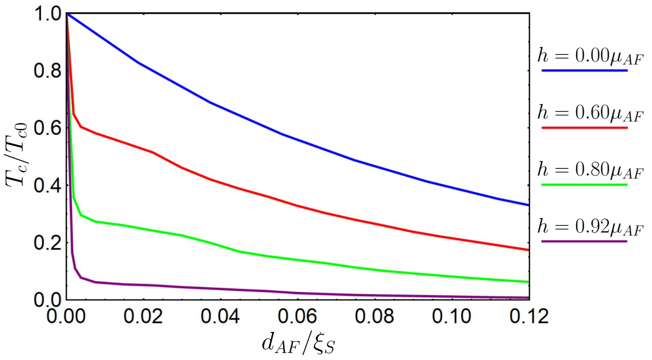

Figure 19. The same as figure 17 but calculated for $d_S = 0.225\xi_S$. The picture is adopted from Ref. [76].

5 Spin-valve effect in AF/S/AF heterostructures

In this section we will discuss how Néel triplet correlations manifest themselves in AF/S/AF trilayers, following Ref. [78]. First of all, we need to define what the spin-valve effect is. Let us consider a heterostructure constructed of a superconductor and two magnetic layers. If the superconducting critical temperature of the hybrid structure is sensitive to the mutual orientation of the magnetizations of the magnetic layers, we call it a spin-valve effect and the structure can be referred as a spin valve. Switching between the superconducting and the normal states by changing the mutual orientation of the magnetizations is called the absolute spin-valve effect.

Spin-valve effect in heterostructures with ferromagnets has been widely studied theoretically[79–84] and experimentally,[85–97] and its origin is intuitively clear. Indeed, let us introduce the misorientation angle ϕ between the magnetizations of the F-layers. Then in the parallel (P) configuration, corresponding to $\phi = 0$, the exchange fields of the two F-layers strengthen each other, while in the antiparallel (AP) case with $\phi = \pi$ they compensate each other. Therefore, we can expect that the critical temperature in the P case to be lower than in the AP case. However, is not always true because the interference of superconducting correlations makes the situation more complicated.

What happens with the spin-valve effect in AF/S/AF structure with fully compensated S/AF interfaces (*i. e.* with zero interface magnetization)? It may seem that such a system is invariant with respect to reversal of the direction of the Néel vector in one of the AF-layers. Then there would be no physical difference between parallel and antiparallel configurations and, consequently, no spin-valve effect. However, it was theoretically shown [98] that the superconducting spin-valve effect can be realized in AF/S/AF structures with insulating antiferromagnets and fully compensated S/AF interfaces despite the absence of macroscopic magnetization in the AF layers. The explanation is connected with the Néel triplet correlations generated by the two S/AF interfaces. Reversing the direction of the Néel vector in one of the AF-layers means reversing signs of the amplitudes of the Néel correlations generated by the corresponding S/AF interface. Therefore, these correlations, analogously to the exchange fields in spin valves with F-layers, can be added (subtracted) inside the superconducting layer depending on the misorientation angle between the Néel vectors, thus suppressing superconductivity more (less) strongly.

For describing the spin-valve effect in AF/S/AF systems with fully compensated interfaces it is convenient to define the misorientation angle ϕ as it is shown in figure 20. We perform a unified division of the entire AF/S/AF structure into two sublattices and define the misorientation angle as the angle between the magnetizations of two antiferromagnets at the same sublattice. Two following subsections are devoted to the influence of the chemical potential and impurities on the spin-valve effect in AF/S/AF structures with insulating antiferromagnets.

5.1 Dependence of spin-valve effect in AF/S/AF heterostructures on chemical potential

In this subsection we discuss the influence of the chemical potential μ_S in the superconducting layer on the dependence $T_c(\phi)$ in the clean case with no impurities in S.

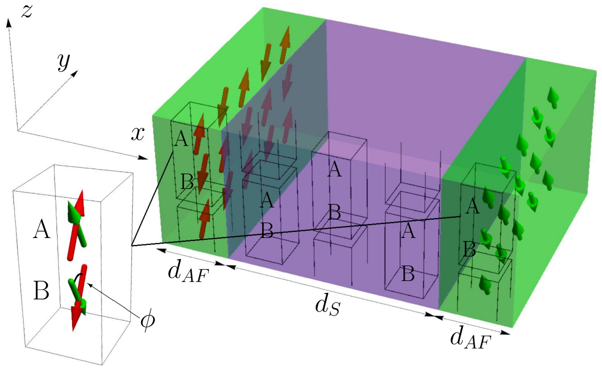

Figure 20. Sketch of the AF/S/AF system. Red and green arrows show Néel-type magnetizations of the AF-layers. The unified division into two sublattices with unit cells containing two sites belonging to A and B sublattices is also shown. The misorientation angle ϕ is defined as the angle between the magnetizations of two antiferromagnets at the same sublattice. The picture is adopted from Ref. [78].

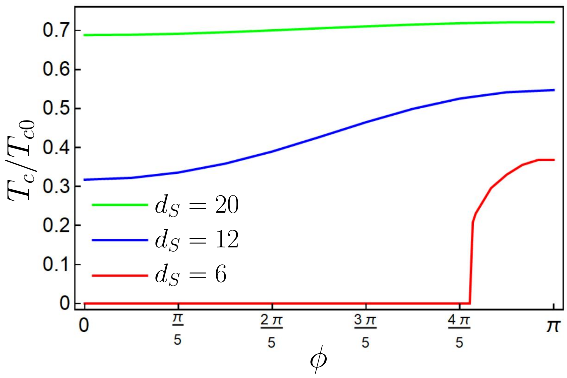

Figure 21. Dependence of T_c on the misorientation angle ϕ for the AF/S/AF structure at half-filling ($\mu_S = 0$). Different curves correspond to the different d_S values (all widths are measured in the number of monolayers). All calculations were performed for the following parameters: $d_{AF} = 4$, $\mu_{AF} = 0$, $h = 0.5t$, and $T_{c0} = 0.07t$. The picture is adopted from Ref. [78].

According to our definition of the misorientation angle, it seems reasonable to expect fulfillment of the relationship $T_c^P < T_c^{AP}$ [here $T_c^P \equiv T_c(\phi = 0)$ and $T_c^{AP} \equiv T_c(\phi = \pi)$], since in the parallel case the Néel triplets generated by the both S/AF interfaces are effectively summed up and strengthen each other inside the S-layer. However, as it will be clear from the following, away from half-filling ($\mu_S = 0$) the opposite result $T_c^P > T_c^{AP}$ can be realized depending on the width d_S of the S-layer.

At first we consider the $T_c(\phi)$ dependence calculated in the case $\mu_S = 0$ (figure 21). We can observe that the spin-valve effect is well-pronounced and the relation $T_c^P < T_c^{AP}$ is fulfilled for all considered d_S values. For larger width of the S-layer the valve effect is reduced, which follows from physical considerations: in the limit $d_S \gg \xi_S$ ($\xi_S \approx 6$ monolayers for the data presented in this subsection) the valve effect should disappear because the two S/AF interfaces do not feel each other and the superconductivity suppression at each of them does not depend on the direction of the Néel vector. The curve cor-

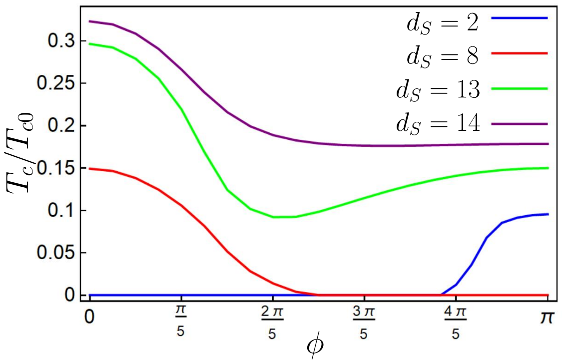

Figure 22. The same as figure 21 but calculated for $\mu_S = 0.2t$. The picture is adopted from Ref. [78].

responding to $d_S = 6$ monolayers demonstrates that for the system under consideration the absolute spin-valve effect, corresponding to the full suppression of superconducting state for a range of misorientation angles, can be realized.

Figure 22 corresponds to $\mu_S = 0.2t$ and demonstrates that the relation between T_c^P and T_c^{AP} can depend on the d_S value. The reason is the finite-momentum Néel triplet correlations, discussed in Section 4. The amplitude of such correlations oscillates in the S layer with the period $L_{\text{osc}} = \pi v_F/|\mu_S|$. Depending on the width of the S layer the Néel triplets generated by the opposite S/AF interfaces can interfere constructively or destructively in the superconductor, which manifests itself in the oscillating behavior of the resulting Néel triplet amplitude for a given ϕ upon varying d_S. This physical picture is further supported by the demonstration of the dependence of $T_c(0, \pi)$ on d_S presented in figure 23. The oscillations of the difference $T_c(\pi) - T_c(0)$ with the period L_{osc}, accompanied by changing sign of the spin-valve effect (*i. e.* the sign of $T_c(\pi) - T_c(0)$), are clearly visible.

Another interesting feature is the non-monotonous behavior of the $T_c(\phi)$ dependence (figure 22). The dip in the critical temperature at ϕ close to $\pi/2$ can be explained by generating of so-called cross product correlations with the amplitude maximal at $\phi \approx \pi/2$. These are triplet correlations determined by $\boldsymbol{h}_l \times \boldsymbol{h}_r$, where $\boldsymbol{h}_{l,r}$ are the Néel vectors of the sublattice A of the left and right AF-layers, respectively, $|\boldsymbol{h}_l| = |\boldsymbol{h}_r| = h$. These correlations are not of sign-changing Néel type and are usual equal-spin triplet correlations. Its amplitude is equal to zero at $\mu_S = 0$, what explains an absense of the dips in figure 21. In figure 22 the dip can be clearly seen only for $d_S = 13$ monolayers. For lower values of the S width the cross product correlations are too weak to result in the pronounced dip-like feature, as its amplitude is proportional to d_S/ξ_S. For higher d_S values the influence of the cross product correlations is weakened due to a smaller overlap of the Néel triplet correlations generated by the opposite S/AF interfaces.

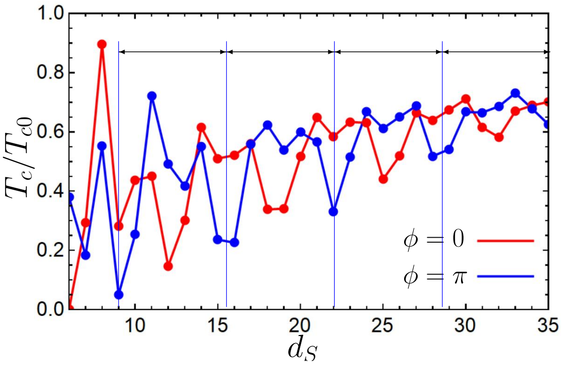

Figure 23. Dependences $T_c(0)$ and $T_c(\pi)$ as functions of d_S at $\mu_S = 0.9t$. The calculations were performed for the following parameters: $d_{AF} = 4$, $\mu_{AF} = 0$, $h = t$, and $T_{c0} = 0.03t$. The period of the oscillations is $L_{\text{ocs}} = \pi v_F/\mu_S \approx 7$. Four periods (minima $T_c(d_S)$ for $\phi = \pi$) are shown on the plot by vertical blue lines. The picture is adopted from Ref. [78].

5.2 Dependence of spin-valve effect in AF/S/AF heterostructures on impurities

It was shown [78, 98] that at $h_{\text{eff}} \equiv ha/d_S \ll T_c$ (here a is the lattice constant of the superconductor in the x-direction) the dependence $T_c(\phi)$ takes the form

$$T_c = T_{c,\parallel} + \Delta T_{c,\parallel}\cos\phi + \Delta T_{c,\perp}\sin^2\phi,$$

where $T_{c,\parallel} = (T_c(0)+T_c(\pi))/2$, $\Delta T_{c,\parallel} = (T_c(0)-T_c(\pi))/2$ is the "$0-\pi$" spin-valve effect and $\Delta T_{c,\perp} = T_c(\pi/2)-T_{c,\parallel}$ is the "perpendicular" spin-valve effect, corresponding to the dips at the $T_c(\phi)$ dependences at $\phi = \pi/2$. In this subsection we discuss the influence of impurities in the S layer on both "$0-\pi$" and "perpendicular" spin-valve effects. The impurities are modelled as random changes of the chemical potential μ_S at each site of the superconductor: $\mu_i = \mu_S + \delta\mu_i$, $\delta\mu_i \in [-\delta\mu, \delta\mu]$, therefore the impurity strength is defined as $\delta\mu$.

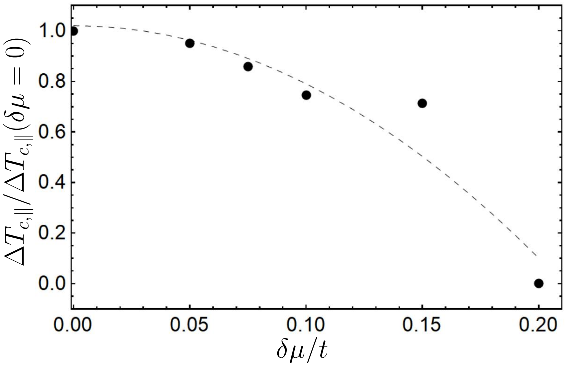

Figure 24. Suppression of the spin-valve effect by impurities. The difference $\Delta T_{c,\parallel}$ is plotted as a function of the impurity strength $\delta\mu$. The difference is normalized to its value at $\delta\mu = 0$. The dashed line is a guide for the eye. All calculations were performed for the following parameters: $\mu_S = 0.9\,t$, $\mu_{AF} = 0$, $h = t$, $d_{AF} = 4$ and $d_S = 20$ monolayers, and $T_{c0} = 0.03\,t$. The picture is adopted from Ref. [78].

Figure 24 demonstrates the gradual disappearing of the "$0-\pi$" valve effect $\Delta T_{c,\parallel}$ under the influence of im-

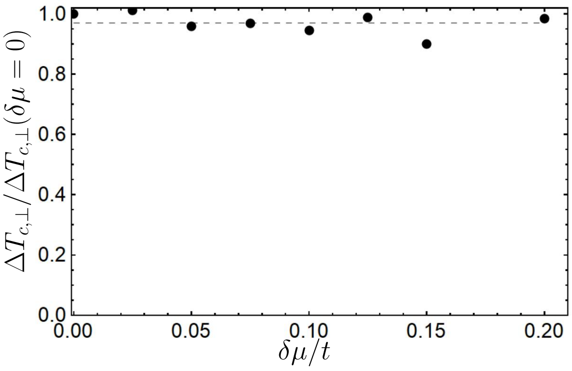

Figure 25. The difference $\Delta T_{c,\perp}$, normalized to its value at $\delta\mu = 0$ as a function of the impurity strength $\delta\mu$. All parameters are the same as in figure 24. The picture is adopted from Ref. [78].

purities. This is explained by the fact that the spin-valve effect of this type is produced by the Néel triplets, which appear due to interband electron pairing[34] and therefore are suppressed by impurities.

Figure 25 presents the dependence of the "perpendicular" spin-valve effect $\Delta T_{c,\perp}$ on the impurity strength. We see that this effect tends to be insensitive to the presence of impurities. This can be considered as a proof of its origin from equal-spin cross product triplet correlations, which should be insensitive to impurities as they are conventional (not Néel) triplets and correspond to the intraband s-wave odd-frequency triplet electron pairing, which is not suppressed by nonmagnetic impurities.

6 Andreev bound states at single impurities in S/AF heterostructures

It is well-known that the Andreev bound states can occur at single impurities in superconductors if the impurities suppress superconductivity for a given system.[99] In particular, magnetic impurities break the time-reversal symmetry and for this reason they are pair-breaking even for conventional s-wave superconductors. Well-known spin-split Yu-Shiba-Rusinov states occur at magnetic impurities.[100–102] They attracted much attention over the last several decades,[99] primarily due to the fact that on chains of magnetic impurities they can form topological bands due to overlapping of bound states at separate impurities.[103–105]

It was recently demonstrated [77] that *spin-splitted* impurity-induced Andreev bound states can also occur in S/AF heterostructures with conventional intraband s-wave pairing at *nonmagnetic* impurities. The system considered in Ref. [77] is sketched in figure 26 and represents a thin-film bilayer composed of a superconductor and a two-sublattice antiferromagnet. The general physical argument allowing for the bound state at a nonmagnetic impurity in such a system is that the impurity can be viewed as effectively magnetic, as it was already discussed in Section 3.2. The spin of a particular bound state is determined by the sublattice to which the impurity belongs, see figure 26 for illustration.

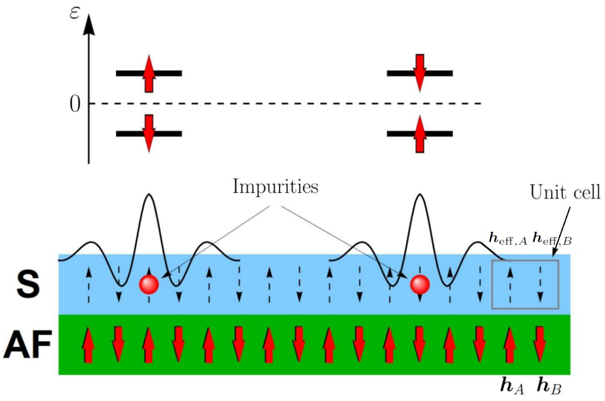

Figure 26. Sketch of the S/AF bilayer with non-interacting impurities. Insulating two-sublattice antiferromagnet (AF) with staggered exchange field $\boldsymbol{h}_A = -\boldsymbol{h}_B$ induces an effective staggered exchange field $\boldsymbol{h}_{\mathrm{eff},A} = -\boldsymbol{h}_{\mathrm{eff},B} \equiv \boldsymbol{h}_{\mathrm{eff}}$ via the proximity effect in the adjacent thin superconductor (S). An impurity can occupy sites A or B in the S layer. Both possible variants are shown by red balls. LDOS of the Andreev bound states localized at the corresponding impurity is shown schematically. The energy spectrum of the bound states with the appropriate spin structure (red arrows) is also shown above the corresponding impurity. The picture is adopted from Ref. [77].

As it was shown in Ref. [77], the presence or absence of the Andreev bound states at single nonmagnetic impurities in S/AF bilayers is also very sensitive to the value of the chemical potential μ of the superconductor. It is the third example of the remarkable sensitivity of the physics of S/AF heterostructures to the value of the chemical potential. For large values $\mu \gg T_{c0}$, when the impurities can be viewed as effectively magnetic, the bound states exist. Energies of the bound states as functions of the impurity strength are plotted in figure 27. It is seen that at stronger staggered effective exchange field h_{eff} the bound state is shifted deeper inside the superconducting gap region. For comparison the energies of the Yu-Shiba-Rusinov bound states at a magnetic impurity with the same strength in a conventional s-wave superconducting host are plotted by the dashed lines. Unlike the case of magnetic impurity the nonmagnetic impurities in S/AF bilayers are not able to support low and zero-energy bound states. In this sense one can say that they are weaker pair-breakers as compared to the magnetic impurities. For small $\mu \lesssim T_{c0}$ the bound states do not appear because the impurities are not effectively magnetic.[77]

The spatial region occupied by the bound state has a scale of the order of the superconducting coherence length ξ_S. The exponential decay is superimposed by a power-law suppression analogously to the case of magnetic impurities in conventional superconductors.[99] However, unlike the magnetic impurities in conventional superconductors here the local density of states (LDOS) has a "staggered" component, which oscillates between the sublattices. If the impurity is localized at A-site, the bound state LDOS is mainly concentrated at the B-sublattice everywhere except for the atomic-scale region near the impurity site. The spatial structure of the LDOS is shown in figure 28.

An interesting feature of the spatial structure of the

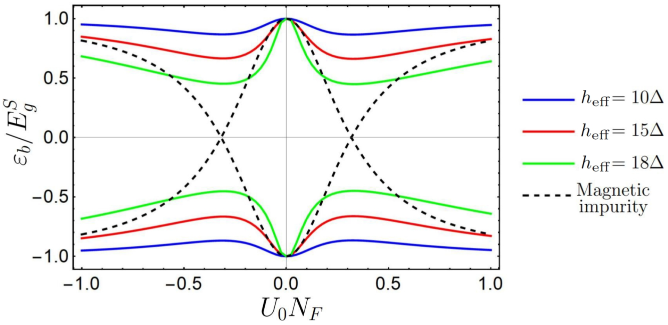

Figure 27. Dependence of the energies of the bound states as a function of the impurity strength U_0 normalized to the density of states N_F at the Fermi surface. Here $\mu = 20\Delta$ and Δ is the value of the order parameter of the superconductor. The energy of the bound state ε_b is normalized to the value of the superconducting gap E_g^S. Different colors correspond to the different $h_{\rm eff}$ values. Dashed lines represent bound state energies at a magnetic impurity with the same strength in a conventional s-wave superconductor. The picture is adopted from Ref. [77].

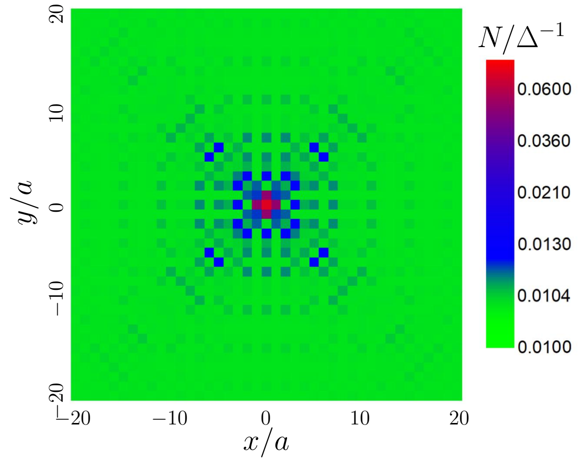

Figure 28. Local density of states N at the energy corresponding to one of the bound states $\varepsilon = -|\varepsilon_b|$ as a function of coordinates. The impurity is at A-site in the centre of the presented spatial region. The picture is adopted from Ref. [77].

bound state LDOS is that the overall decay of the LDOS and the "staggered" oscillations associated with the sublattice structure are also superimposed by oscillations of a larger spatial scale compared to the atomic one, which is nevertheless significantly smaller than the superconducting coherence length scale. These oscillations are due to the generation of finite-momentum Néel-type triplet correlations, which were discussed in Section 4. Here they are produced due to the Umklapp electron scattering processes at the impurities. The period of these oscillations is $L_{\rm osc} = \pi v_F/\sqrt{\mu^2 - h^2}$. Data presented in figure 28 are calculated at $h = 1.5t$ and $\mu = 2t$, giving us $L_{\rm osc} \approx 4a$, what is in agreement with the additional oscillation period seen in the figure.

The presence of the Andreev bound states at single nonmagnetic impurity in S/AF bilayers is in agreement with the behavior of the superconducting critical temperature of such systems in the presence of random disorder, which has already been studied[38] and discussed in Section 3. At $\mu \lesssim T_{c0}$ the nonmagnetic impurities are not pair-breaking and they enhance superconductivity of S/AF bilayers due to the suppression of the Néel triplet correlations.[34, 38] On the contrary, if $\mu \gg T_{c0}$ the superconductivity is suppressed by random nonmagnetic disorder.[17–19, 38] The same sensitivity to the value of the chemical potential occurs in the problem of a single impurity: the bound states only exist at $\mu \gg T_{c0}$, when superconductivity is suppressed by impurities.

7 Néel triplets in the presence of spin-orbit interaction

Many studies are devoted to the interplay of conventional correlations and spin-orbit coupling (SOC) in S/F hybrid structures.[10, 106–112] It was predicted and observed that SOC in S/F bilayers can produce an anisotropic depairing effect on triplets. One of the manifestations of the anisotropic depairing is that the critical temperature T_c of the bilayer depends on the orientation of the F layer magnetization with respect to the S/F interface.[112–115] This behavior is interesting not only from a fundamental point of view, but also for spintronics applications because there is a possibility for a reciprocal effect: reorientation of the F-layer magnetization due to superconductivity.[116–118] The possibility to control magnetic anisotropy using superconductivity is a key point in designing cryogenic magnetic memory and spintronics applications in near future.

In this section we discuss anisotropic effect of the Rashba SOC on the Néel triplets in S/AF thin-film bilayers. The key feature is that in addition to the anisotropic depairing of the triplet correlations known in S/F hybrids, a unique effect of anisotropic enhancement of the triplets by the SOC occurs in the S/AF case. We discuss the physical mechanism of the effect and demonstrate that it can manifest itself in opposite trend in the anisotropy of the superconducting transition as compared to S/F heterostructures. The SOC results in the depairing or enhancement of the Néel triplets depending on the value of the chemical potential of the superconductor and it is the fourth physical manifestation of the strong sensitivity of the physics of S/AF hybrid structures to the value of the chemical potential.

7.1 Anisotropy of the Néel triplets and T_c

The anisotropic effect of the Rashba SOC was considered in Ref. [119] by an example of a thin-film S/AF bilayer, where the antiferromagnet is assumed to be an insulator (figure 29). The SOC is induced in the S layer by proximity to a heavy metal layer like Pt (shown as the SO layer in figure 29). The SOC can also be due to the inversion-symmetry breaking in the S film by itself. The magnetism is staggered. The S/AF interfaces were assumed fully compensated (*i. e.*, the interface magnetization has zero average value). The influence of the antiferromagnetic insulator on the superconductor was described by the exchange field $\boldsymbol{h}_{{\rm eff},\boldsymbol{i}} = (-1)^{i_x+i_z}\boldsymbol{h}_{\rm eff}$.

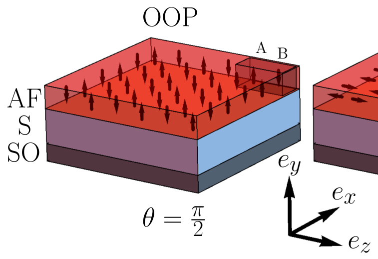

Figure 29. Sketch of the thin-film S/AF bilayer with SOC. The Néel vector of the AF makes angle θ with the plane of the structure. $\theta = 0$ corresponds to the in-plane (IP) and $\theta = \pi/2$ accounts for the out-of-plane (OOP) orientations. Unit cell with two sites A and B is also shown. The picture is adopted from Ref.[119]

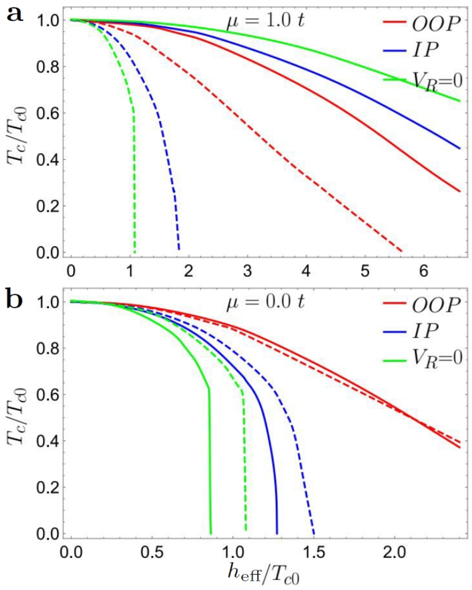

Figure 30. **a**, **b** – Critical temperature of S/AF (solid curves) and S/F bilayers (dashed) as a function of the effective exchange field $h_{\rm eff}$. Panels a and b correspond to $\mu = 12T_{c0}$ and $\mu = 0$, respectively. Green curves represent the results with no SOC, red and blue curves are for out-of-plane (OOP) and in-plane (IP) orientations, respectively, and $V_R = 0.4t$ is the Rashba SOC strength. The picture is adopted from Ref. [119].

Figure 30 shows the dependences $T_c(h_{\rm eff})$ for S/AF structures with in-plane (IP) and out-of-plane (OOP) orientations of the Néel vector. They have been compared to $T_c(h_{\rm eff})$ of the S/F system with the same absolute value of the effective exchange field $h_{\rm eff}$ (conventional, not staggered). First, it is seen that while for S/F heterostructures T_c is always higher in the presence of SOC (dashed curves), for S/AF heterostructures the trends are opposite for large $\mu \gg T_{c0}$ and small $\mu \lesssim T_{c0}$. At small μ the behavior of T_c is qualitatively similar to the case of S/F bilayers, and at large μ it is opposite: the presence of SOC *suppresses* T_c.

Furthermore, in the presence of SOC T_c becomes anisotropic and it depends on the angle θ between the magnetization and the interface plane. For S/F heterostructures T_c is always higher for the OOP orientation (dashed curves).[112–115] At the same time for S/AF heterostructures the ratio between the values of T_c for both IP and OOP orientations is again opposite for large $\mu \gg T_{c0}$ and small $\mu \lesssim T_{c0}$. At $\mu \lesssim T_{c0}$ for S/AF heterostructures the ratio between T_c for both IP and OPP orientations is the same as for the S/F case. At $\mu \gg T_{c0}$ the anisotropy of the critical temperature (in the other words, the difference between T_c for the IP and OOP orientations) is opposite.

7.2 Physical mechanism of the T_c anisotropy

Here we discuss the physical reasons of the numerical findings described in the previous subsection. First of all, as it was already discussed in Section 2.5, if $\mu \lesssim \pi T_{c0}$, then the most important contribution to the pairing correlations is given by the electronic states corresponding to $\xi_\pm \approx 0$. This means that the electrons are at the edge of the antiferromagnetic gap and, therefore, practically fully localized at one of the sublattices. Consequently, they only feel the magnetization of the corresponding sublattice and behave in the same way as in the ferromagnet. For this reason our results at $\mu \lesssim \pi T_c$ demonstrate the same trends as the corresponding results for S/F structures. It is well-known that in S/F heterostructures the critical temperature is higher for OOP magnetization orientation than for the IP magnetization[115] due to the fact that SOC suppresses triplets oriented OOP more than triplets oriented IP. The same is observed in figure 30b for S/AF bilayers with $\mu = 0$. Moreover, the SOC always suppresses triplets and, correspondingly, enhances T_c. The same is seen in figure 30b for S/AF heterostructures.

The opposite trend at $\mu \gg T_{c0}$ is due to the existence of a unique mechanism of generation of the Néel triplet correlations in S/AF heterostructures, which differs from the mechanism of the direct singlet-triplet conversion known in S/F heterostructures. The Néel triplets are generated via the normal state Néel-type spin polarization of the DOS.[119] Up to the leading order in $h_{\rm eff}/|\mu|$ and $h_R/|\mu|$ the Néel-type polarization of the normal state DOS along $\boldsymbol{h}_{\rm eff}$ and at the Fermi surface takes the form

$$P^A_{\boldsymbol{h}} = -P^B_{\boldsymbol{h}} = 2N_F\left(\frac{h_{\rm eff}}{\mu} + \frac{h_{\rm eff} h_R^2 \sin^2\phi}{\mu^3}\right), \qquad (6)$$

where N_F is the normal-state DOS at the Fermi surface of the isolated superconductor, $\boldsymbol{h}_R \propto V_R(\boldsymbol{e}_y \times \boldsymbol{v}_F)$ is the effective Rashba pseudomagnetic field acting on an electron moving along the trajectory determined by the Fermi velocity $\boldsymbol{v}_F$ and ϕ is the angle between $\boldsymbol{h}_{\rm eff}$ and $\boldsymbol{h}_R$. It is seen that (i) the absolute value of the polarization is always enhanced by the SOC and (ii) the enhancement is anisotropic. It reaches maximal possible value for all the trajectories for out-of-plane orientation of $\boldsymbol{h}_{\rm eff}$ because $\boldsymbol{h}_R$ is always in-plane. The reason for the described above enhancement is the specific reconstruction of normal state electron spectra under the influence of the SOC.[119]

In S/F heterostructures the effective exchange field $\boldsymbol{h}_{\rm eff}$ is also generated in the superconductor due to proximity with a ferromagnetic insulator. It results in the occurrence of the normal state polarization of the DOS of conventional type $P \sim N_F(h_{\rm eff}/\varepsilon_F) \ll N_F$. However, this polarization is always very small, because the effective exchange induced in the superconductor cannot be higher than the superconducting order parameter,[9] otherwise it completely suppresses superconductivity. Therefore, in S/F bilayers this quantity does not play a significant role in the generation of triplets. At the same time, the Néel type polarization, described by Eq. (6) is not necessary small and provides a generator for the Néel triplets. The enhancement of the Néel type polarization of the normal state by SOC leads to the *enhancement* of the Néel-type triplet correlations in S/AF structures. It was obtained in Ref. [119] that at $\mu \gg T_{c0}$ up to the leading order in $h_{\rm eff}/|\mu|$ and $h_R/|\mu|$ the anomalous Green's function of the Néel-type triplet correlations takes the form:

$$\boldsymbol{f}^y = \operatorname{sgn}\omega \cdot \left(\frac{i\Delta \boldsymbol{h}_{\rm eff}}{\mu^2} + \frac{3i\Delta[\boldsymbol{h}_R \times (\boldsymbol{h}_{\rm eff} \times \boldsymbol{h}_R)]}{\mu^4} \right), \quad (7)$$

where ω is the Matsubara frequency. The component of $\boldsymbol{f}^y$ along the effective exchange field $\boldsymbol{h}_{\rm eff}$, which accounts for the suppression of the critical temperature by the triplets, takes the form:

$$\boldsymbol{f}^y_{\boldsymbol{h}} = \operatorname{sgn}\omega \cdot \frac{\boldsymbol{h}_{\rm eff}}{\mu} \left(\frac{i\Delta}{\mu} + \frac{3i\Delta h_R^2 \sin^2\phi}{\mu^3} \right). \quad (8)$$

Thus, the amplitude of the Néel triplet correlations qualitatively follows the normal state Néel polarization and it is also enhanced by the SOC. The effect of the enhancement is the strongest for the OOP orientation corresponding to $\phi = \pi/2$.

8 Conclusions

In this review we discussed the physics of Néel triplet proximity effect in S/AF heterostructures, which was studied in a number of recent papers. The main findings can be summarized as follows:

- At S/AF interfaces unconventional triplet correlations are generated. The amplitude of the corresponding pair wave function flips sign from one site of the materials to the nearest one following the Néel structure of the antiferromagnetic order parameter. The correlations can occur in superconductors due to proximity to the antiferromagnetic insulators and metals and penetrate into antiferromagnetic metals from superconductors. They are generated even at fully compensated S/AF interfaces with zero net magnetization of the interface. These triplet correlations were called the Néel triplet correlations.
- The Néel triplets suppress superconductivity. The efficiency of the suppression is of the same order and frequently a bit stronger than the suppression by the conventional proximity-induced triplet correlations in S/F heterostructures.
- The mechanism of the Néel triplets generation differs from the well-known direct singlet-triplet conversion in S/F heterostructures. They are produced via the effect caused on the singlet superconducting correlations by the Néel-type normal state electron polarization, induced in the superconductor by proximity to the AF. This mechanism results in the opposite as compared to S/F heterostructures trends in the anisotropy of the critical temperature of S/AF heterostructures in the presence of SOC.
- The higher the Néel exchange field of the AF or proximity-induced effective exchange field in the S the stronger the amplitude of the Néel triplets, is. At the same time, unlike S/F heterostuctures the amplitude of the Néel triplet correlations is very sensitive to the value of the chemical potential in the material, where they are induced. Deviation from half filling suppresses the amplitude of the Néel triplets for a given value of the Néel exchange field.
- Near half-filling the Néel triplets are interband, and far from half-filling they are intraband. It results in very different response of the Néel triplet correlations on the nonmagnetic impurities: near half-filling the Néel triplets are suppressed by impurities and far from half-filling they are immune to impurities.
- The above behavior of the Néel triplets in the presence of nonmagnetic impurities leads to very different dependencies of the critical temperature of S/AF bilayers on the impurity strength: near half-filling the impurities enhance the critical temperature, and far from half-filling they suppress it. The second tendency is caused by an additional mechanism: far from half-filling the nonmagnetic impurities in S/AF heterostructures behave like effectively magnetic and suppress singlet superconductivity by themselves.
- The effective magnetic character of the nonmagnetic impurities in S/AF heterostructures leads to the occurrence of the spin-split Andreev bound states at single impurities, which are reminiscent of well-known Yu-Shiba-Rusinov bound states at magnetic impurities in superconducting materials, but occurring at *nonmagnetic* impurities.
- The Néel triplet correlations provide a possibility to realize a spin-valve effect in AF/S/AF trilayers even with fully compensated interfaces.
- Due to the lost of the translational invariance at S/AF interfaces and/or at single nonmagnetic impurity a finite-momentum Néel triplet pairing can occur. It results in (i) the oscillations of the critical temperature of S/AF bilayers with metallic antiferromagnets as a function of the thickness of the AF layer, (ii) peculiar oscillations of the impurity-induced DOS around nonmagnetic impurities, and (iii) sign inversion of the spin-valve effect in AF/S/AF trilayers upon varying the width of the S layer.
- Unlike S/F heterostructures the physics of S/AF heterostructures is crucially sensitive to the value

of the chemical potential. Two physically very different regimes can be identified near half-filling and far from half-filling. In particular, the dependence of the critical temperature of S/AF heterostructures on impurity concentration is opposite in these regimes, the dependence of the critical temperature of heterostructures with canted AFs on the canting angle is also opposite, the same applies to the magnetic anisotropy in S/AF heterostructures with SOC and to the formation of the Andreev bound states at single nonmagnetic impurities.

It could be especially interesting to study the described effects in heterostructures composed of antiferromagnets and 2D superconductors because of possibility of external control of the chemical potential.

Acknowledgements

We are grateful to A. A. Golubov for the discussion of the obtained results. The work was supported by Russian Science Foundation (project No. 23-72-30004.)

Contact information

Corresponding author: Irina V. Bobkova, orcid.org/ 0000-0003-1469-1861, e-mail ivbobkova@mail.ru.

Competing Interests

The authors declare no competing financial or non-financial interests.

References

[1] Cooper L. N. *Bound Electron Pairs in a Degenerate Fermi Gas.* Phys. Rev., vol. **104**, 1189-1190 (1956).

[2] Bardeen J., Cooper L. N., Schrieffer J. R. *Microscopic Theory of Superconductivity.* Phys. Rev., vol. **106**, 162-164 (1957).

[3] Bergeret F. S., Volkov A. F., Efetov K. B. *Odd triplet superconductivity and related phenomena in superconductor-ferromagnet structures.* Rev. Mod. Phys., vol. **77**, 1321-1373 (2005).

[4] Buzdin A. I. *Proximity effects in superconductor-ferromagnet heterostructures.* Rev. Mod. Phys., vol. **77**, 935-976 (2005).

[5] Bergeret F. S., Silaev M., Virtanen P., Heikkilä T. T. *Colloquium: Nonequilibrium effects in superconductors with a spin-splitting field.* Rev. Mod. Phys., vol. **90**, 041001 (2018).

[6] Eschrig M., Cottet A., Belzig W., Linder J. *General boundary conditions for quasiclassical theory of superconductivity in the diffusive limit: application to strongly spin-polarized systems.* New J. Phys., vol. **17**, 083037 (2015).

[7] Chandrasekhar B. S. *A note on the maximun critical critical field of high-field superconductors.* Appl. Phys. Lett., vol. **1**, 7-8 (1962).

[8] Clogston A. M. *Upper Limit for the Critical Field in Hard Superconductors.* Phys. Rev. Lett., vol. **9**, 266-267 (1962).

[9] Sarma G. *On the influence of a uniform exchange field acting on the spins of the conduction electrons in a superconductor.* J. Phys. Chem. Solids, vol. **24**, 1029-1032 (1963).

[10] Linder J., Robinson J. W. A. *Superconducting spintronics.* Nat. Phys., vol. **11**, 307-315 (2015).

[11] Eschrig M. *Spin-polarized supercurrents for spintronics: a review of current progress.* Rep. Prog. Phys., vol. **78**, 104501 (2015).

[12] Hauser J. J., Theuerer H. C., Werthamer N. R. *Proximity Effects between Superconducting and Magnetic Films.* Phys. Rev., vol. **142**, 118-126 (1966).

[13] Kamra A., Rezaei A., Belzig W. *Spin Splitting Induced in a Superconductor by an Antiferromagnetic Insulator.* Phys. Rev. Lett., vol. **121**, 118-126 (2018).

[14] Bobkov G. A., Bobkova I. V., Bobkov A. M., Kamra A. *Thermally induced spin torque and domain-wall motion in superconductor/antiferromagnetic-insulator bilayers.* Phys. Rev. B, vol. **103**, 094506 (2021).

[15] Rabinovich D. S., Bobkova I. V., Bobkov A. M. *Anomalous phase shift in a Josephson junction via an antiferromagnetic interlayer.* Phys. Rev. Res., vol. **1**, 033095 (2019).

[16] Falch V., Linder J. *Giant magnetoanisotropy in the Josephson effect and switching of staggered order in antiferromagnets.* Phys. Rev. B, vol. **106**, 214511 (2022).

[17] Buzdin A. I., Bulaevskiĭ L. N. *Antiferromagnetic superconductors.* Sov. Phys. Uspekhi, vol. **29**, 412-425 (1986).

[18] Fyhn E. H., Brataas A., Qaiumzadeh A., Linder J. *Quasiclassical theory for antiferromagnetic metals.* Phys. Rev. B, vol. **107**, 174503 (2023).

[19] Fyhn E. H., Brataas A., Qaiumzadeh A., Linder J. *Superconducting Proximity Effect and Long-Ranged Triplets in Dirty Metallic Antiferromagnets.* Phys. Rev. Lett., vol. **131**, 076001 (2023).

[20] Bell C., Tarte E. J., Burnell G., Leung C. W., Kang D.-J., Blamire, M. G. *Proximity and Josephson effects in superconductor/antiferromagnetic* $\mathrm{Nb}/\gamma-\mathrm{Fe}_{50}\mathrm{Mn}_{50}$ *heterostructures.* Phys. Rev. B, vol. **68**, 144517 (2003).

[21] Hübener M., Tikhonov D., Garifullin I. A., Westerholt K., Zabel H. *The antiferromagnet/superconductor proximity effect in Cr/V/Cr trilayers.* J. Phys.: Condens. Matt., vol. **14**, 8687-8696 (2002).

[22] Wu B. L., Yang Y. M., Guo Z. B., Wu Y. H., Qiu J. J. *Suppression of superconductivity in Nb by IrMn in IrMn/Nb bilayers.* Appl. Phys. Lett., vol. **103**, 152602 (2013).

[23] Seeger R. L., Forestier G., Gladii O., Leiviskä M., Auffret S., Joumard I., Gomez C., Rubio-Roy M., Buzdin A. I., Houzet M., Baltz V. *Penetration depth of Cooper pairs in the IrMn antiferromagnet.* Phys. Rev. B, vol. **104**, 054413 (2021).

[24] Krivoruchko V. N. *Upper critical fields of the superconducting state of a superconductor-antiferromagnetic metal superlattice.* Sov. Phys. JETP, vol. **109**, 649 (1996).

[25] Belashchenko K. D. *Equilibrium Magnetization at the Boundary of a Magnetoelectric Antiferromagnet.* Phys. Rev. Lett., vol. **105**, 147204 (2010).

[26] He X., Wang Y., Wu N., Caruso A. N., Vescovo E., Belashchenko K. D., Dowben P. A., Binek C. *Robust isothermal electric control of exchange bias at room temperature.* Nat. Mater., vol. **9**, 579 (2010).

[27] Manna P. K., Yusuf S. M. *Two interface effects: Exchange bias and magnetic proximity.* Phys. Rep., vol. **535**, 61-99 (2014).

[28] Bobkova I. V., Hirschfeld P. J., Barash Yu. S. *Spin-Dependent Quasiparticle Reflection and Bound States at Interfaces with Itinerant Antiferromagnets.* Phys. Rev. Lett., vol. **94**, 037005 (2005).

[29] Andersen B. M., Bobkova I. V., Hirschfeld P. J., Barash, Yu. S. *Bound states at the interface between antiferromagnets and superconductors.* Phys. Rev. B, vol. **72**, 184510 (2005).

[30] Andersen B. M., Bobkova I. V., Hirschfeld P. J., Barash Yu. S. *$0-\pi$ Transitions in Josephson Junctions with Antiferromagnetic Interlayers.* Phys. Rev. Lett., vol. **96**, 117005 (2006).

[31] Enoksen H., Linder J., Sudbø A. *Pressure-induced 0-π transitions and supercurrent crossover in antiferromagnetic weak links.* Phys. Rev. B, vol. **88**, 214512 (2013).

[32] Bulaevskii L., Eneias R., Ferraz A. *Superconductor-antiferromagnet-superconductor π Josephson junction based on an antiferromagnetic barrier.* Phys. Rev. B, vol. **95**, 104513 (2017).

[33] Johnsen L. G., Jacobsen S. H., Linder J. *Magnetic control of superconducting heterostructures using compensated antiferromagnets.* Phys. Rev. B, vol. **103**, L060505 (2021).

[34] Bobkov G. A., Bobkova I. V., Bobkov A. M., Kamra A. *Néel proximity effect at antiferromagnet/superconductor interfaces.* Phys. Rev. B, vol. **106**, 144512 (2022).

[35] Cheng R., Xiao J., Niu Q., Brataas A. *Spin Pumping and Spin-Transfer Torques in Antiferromagnets.* Phys. Rev. Lett., vol. **113**, 057601 (2014).

[36] Takei S., Halperin B. I., Yacoby A., Tserkovnyak Y. *Superfluid spin transport through antiferromagnetic insulators.* Phys. Rev. B, vol. **90**, 094408 (2014).

[37] Baltz V., Manchon A., Tsoi M., Moriyama T., Ono T., Tserkovnyak Y. *Antiferromagnetic spintronics.* Rev. Mod. Phys., vol. **90**, 015005 (2018).

[38] Bobkov G. A., Bobkova I. V., Bobkov A. M. *Proximity effect in superconductor/antiferromagnet hybrids: Néel triplets and impurity suppression of superconductivity.* Phys. Rev. B, vol. **108**, 054510 (2023).

[39] Chourasia S., Kamra L. J., Bobkova I. V., Kamra A. *Generation of spin-triplet Cooper pairs via a canted antiferromagnet.* Phys. Rev. B, vol. **108**, 064515 (2023).

[40] Abrikosov A. A., Gor'kov L. P. *Contribution to the theory of superconducting alloys with paramagnetic impurities.* Sov. Phys. JETP, vol. **12**, 1243 (1961).

[41] Goldman A. M., Marković N. *Superconductor-Insulator Transitions in the Two-Dimensional Limit.* Phys. Today, vol. **51**, 39-44 (1998).

[42] Sadovskii M. V. *Superconductivity and localization.* Phys. Rep., vol. **282**, 225-348 (1997).

[43] Gantmakher V. F., Dolgopolov V. T. *Superconductor-insulator quantum phase transition.* Sov. Phys. Uspekhi, vol. **53**, 1 (2010).

[44] Sacépé B., Chapelier C., Baturina T. I., Vinokur V. M., Baklanov M. R., Sanquer M. *Disorder-Induced Inhomogeneities of the Superconducting State Close to the Superconductor-Insulator Transition.* Phys. Rev. Lett., vol. **101**, 157006 (2008).

[45] Sacépé B., Chapelier C., Baturina T. I., Vinokur V. M., Baklanov M. R., Sanquer M. *Superconductor-insulator quantum phase transition.* Nat. Comm., vol. **1**, 140 (2010).

[46] Arrigoni E., Kivelson S. A. *Optimal inhomogeneity for superconductivity.* Phys. Rev. B, vol. **68**, 180503 (2003).

[47] Gastiasoro M. N., Andersen B. M. *Enhancing superconductivity by disorder.* Phys. Rev. B, vol. **98**, 184510 (2018).

[48] Martin I., Podolsky D., Kivelson S. A. *Enhancement of superconductivity by local inhomogeneities.* Phys. Rev. B, vol. **72**, 060502 (2005).

[49] Zhao K., Lin H., Xiao X., Huang W., Yao W., Yan M., Xing Y., Zhang Q., Li Z.-X., Hoshino S., Wang J., Zhou S., Gu L., Bahramy M. S., Yao H., Nagaosa N., Xue Q.-K., Law K. T., Chen X., Ji S.-H. *Disorder-induced multifractal superconductivity in monolayer niobium dichalcogenides.* Nat. Comm., vol. **15**, 904-910 (2019).

[50] Petrović A. P., Ansermet D., Chernyshov D., Hoesch M., Salloum D., Gougeon P., Potel M., Boeri L., Panagopoulos C. *Disorder-induced multifractal superconductivity in monolayer niobium dichalcogenides.* Nat. Comm., vol. **7**, 12262 (2016).

[51] Peng J., Yu Z., Wu J., Zhou Y., Guo Y., Li Z., Zhao J., Wu C., Xie Y., *Disorder Enhanced Superconductivity toward TaS_2 Monolayer.* ACS Nano, vol. **12**, 9461-9466 (2018).

[52] Neverov V. D., Lukyanov A. E., Krasavin A. V., Vagov A., Croitoru M. D. *Correlated disorder as a way towards robust superconductivity.* Comm. Phys., vol. **5**, 177 (2022).

[53] Larkin A. I., Ovchinnikov Y. N. *Nonuniform state of superconductors.* Sov Phys. JETP, vol. **47**, 1136-1146 (1964).

[54] Fulde P., Ferrell R. A. *Superconductivity in a Strong Spin-Exchange Field.* Phys. Rev., vol. **135**, A550-A563 (1964).

[55] Buzdin A. I., Bulaevskii L. N., Panyukov S. V. *Critical-current oscillations as a function of the exchange field and thickness of the ferromagnetic metal (F) in an S-F-S Josephson junction.* JETP Lett., vol. **135**, 178-180 (1982).

[56] Demler E. A., Arnold G. B., Beasley M. R. *Superconducting proximity effects in magnetic metals.* Phys. Rev. B, vol. **55**, 15174-15182 (1997).

[57] Kontos T., Aprili M., Lesueur J., Genêt F., Stephanidis B., Boursier R. *Josephson Junction through a Thin Ferromagnetic Layer: Negative Coupling.* Phys. Rev. Lett., vol. **89**, 137007 (2002).

[58] Ryazanov V. V., Oboznov V. A., Rusanov A. Yu., Veretennikov A. V., Golubov A. A., Aarts J. *Coupling of Two Superconductors through a Ferromagnet: Evidence for a π Junction.* Phys. Rev. Lett., vol. **86**, 2427-2430 (2001).

[59] Oboznov V. A., Bol'ginov V. V., Feofanov A. K., Ryazanov V. V., Buzdin, A. I. *Thickness Dependence of the Josephson Ground States of Superconductor-Ferromagnet-Superconductor Junctions.* Phys. Rev. Lett., vol. **96**, 197003 (2006).

[60] Bannykh A. A., Pfeiffer J., Stolyarov V. S., Batov I. E., Ryazanov V. V., Weides M. *Josephson tunnel junctions with a strong ferromagnetic interlayer.* Phys. Rev. B, vol. **79**, 054501 (2009).

[61] Robinson J. W. A., Piano S., Burnell G., Bell C., Blamire M. G. *Critical current oscillations in strong ferromagnetic π junctions.* Phys. Rev. B, vol. **97**, 177003 (2006).

[62] Yamashita T., Tanikawa K., Takahashi S., Maekawa S. *Superconducting π Qubit with a Ferromagnetic Josephson Junction.* Phys. Rev. Lett., vol. **95**, 097001 (2005).

[63] Feofanov A. K., Oboznov V. A., Bol'ginov V. V., Lisenfeld J., Poletto S., Ryazanov V. V., Rossolenko A. N., Khabipov M., Balashov D., Zorin A. B., Dmitriev P. N., Koshelets V. P., Ustinov A. V. *Implementation of superconductor/ferromagnet/ superconductor π-shifters in superconducting digital and quantum circuits.* Nat. Phys., vol. **6**, 593-597 (2010).

[64] Shcherbakova A. V., Fedorov K. G., Shulga K. V., Ryazanov V. V., Bolginov V. V., Oboznov V. A., Egorov S. V., Shkolnikov V. O., Wolf M. J., Beckmann D., Ustinov A. V. *Fabrication and measurements of hybrid Nb/Al Josephson junctions and flux qubits with π-shifters.* Supercond. Sci. Technol., vol. **28**, 025009 (2015).

[65] Fominov Ya. V., Chtchelkatchev N. M., Golubov A. A. *Nonmonotonic critical temperature in superconductor/ferromagnet bilayers.* Phys. Rev. B, vol. **66**, 014507 (2002).

[66] Radović Z., Ledvij M., Dobrosavljević-Grujić, L., Buzdin A. I., Clem J. R. *Nonmonotonic critical temperature in superconductor/ferromagnet bilayers.* Phys. Rev. B, vol. **44**, 759-764 (1991).

[67] Vodopyanov B. P., Tagirov L. R. *Oscillations of superconducting transition temperature in strong ferromagnet-superconductor bilayers.* JETP Lett., vol. **78**, 555-559 (2003).

[68] Lazar L., Westerholt K., Zabel H., Tagirov L. R., Goryunov Yu. V., Garif'yanov N. N., Garifullin I. A. *Superconductor/ferromagnet proximity effect in Fe/Pb/Fe trilayers.* Phys. Rev. B, vol. **61**, 3711-3722 (2000).

[69] Buzdin A. *Density of states oscillations in a ferromagnetic metal in contact with a superconductor.* Phys. Rev. B, vol. **62**, 11377-11379 (2000).

[70] Zareyan M., Belzig W., Nazarov Yu. V. *Oscillations of Andreev States in Clean Ferromagnetic Films.* Phys. Rev. Lett., vol. **86**, 308-311 (2001).

[71] Jiang J. S., Davidović D., Reich D. H., Chien C. L. *Oscillatory Superconducting Transition Temperature in Nb/Gd Multilayers.* Phys. Rev. Lett., vol. **74**, 314-317 (1995).

[72] Mercaldo L. V., Attanasio C., Coccorese C., Maritato L., Prischepa S. L., Salvato, M. *Superconducting-critical-temperature oscillations in Nb/CuMn multilayers.* Phys. Rev. B, vol. **53**, 14040-14042 (1996).

[73] Mühge Th., Garif'yanov N. N., Goryunov Yu. V., Khaliullin G. G., Tagirov L. R., Westerholt K., Garifullin I. A., Zabel H. *Possible Origin for Oscillatory Superconducting Transition Temperature in Superconductor/Ferromagnet Multilayers.* Phys. Rev. Lett., vol. **77**, 1857-1860 (1996).

[74] Zdravkov V., Sidorenko A., Obermeier G., Gsell S., Schreck M., Müller C., Horn S., Tideck R., Tagirov L. R. *Reentrant Superconductivity in* $\mathrm{Nb/Cu_{1-x}Ni_x}$ *Bilayers.* Phys. Rev. Lett., vol. **97**, 057004 (2006).

[75] Zdravkov V. I., Kehrle J., Obermeier G., Gsell S., Schreck M., Müller C., Krug von Nidda H.-A., Lindner J., Moosburger-Will J., Nold E., Morari R., Ryazanov V. V., Sidorenko A. S., Horn S., Tidecks R., Tagirov L. R. *Reentrant superconductivity in superconductor/ferromagnetic-alloy bilayers.* Phys. Rev. B, vol. **82**, 054517 (2010).

[76] Bobkov G. A., Gordeeva V. M., Bobkov A. M., Bobkova I. V. *Oscillatory superconducting transition temperature in superconductor/antiferromagnet heterostructures.* Phys. Rev. B, vol. **108**, 184509 (2023).

[77] Bobkov G. A., Bobkova I. V., Bobkov A. M. *Andreev bound states at nonmagnetic impurities in superconductor/antiferromagnet heterostructures.* Phys. Rev. B, v. **109**, 214508 (2024).

[78] Bobkov G. A., Gordeeva V. M., Kamra L. J., Chourasia S., Bobkov A. M., Kamra A., Bobkova I. V. *Superconducting spin valves based on antiferromagnet/superconductor/antiferromagnet heterostructures.* Phys. Rev. B, vol. **109**, 184504 (2024).

[79] De Gennes P. G. *Coupling between ferromagnets through a superconducting layer.* Phys. Lett., vol. **23**, 10-11 (1966).

[80] Oh S., Youm D., Beasley M. R. *A superconductive magnetoresistive memory element using controlled exchange interaction.* Appl. Phys. Lett., vol. **71**, 2376 (1997).

[81] Tagirov, L. R. *Low-Field Superconducting Spin Switch Based on a Superconductor/Ferromagnet Multilayer.* Phys. Rev. Lett., vol. **83**, 2058-2061 (1999).

[82] Fominov Ya. V., Golubov A. A., Kupriyanov M. Yu. *Triplet proximity effect in FSF trilayers.* JETP Lett., vol. **77**, 510 (2003).

[83] Fominov Ya. V., Golubov A. A., Karminskaya T. Yu., Kupriyanov M. Yu., Deminov R. G., Tagirov, L. R. *Superconducting triplet spin valve.* JETP Lett., vol. **91**, 308 (2010).

[84] Wu C.-T., Valls O. T. *Superconducting Proximity Effects in Ferromagnet/Superconductor Heterostructures.* J. Supercond. Nov. Magn., vol. **25**, 2173 (2012).

[85] Li B., Roschewsky N., Assaf B. A., Eich M., Epstein-Martin M., Heiman D., Münzenberg M., Moodera J. S. *Superconducting Spin Switch with Infinite Magnetoresistance Induced by an Internal Exchange Field.* Phys. Rev. Lett., vol. **110**, 097001 (2013).

[86] Moraru I. C., Pratt W. P., Birge N. O. *Magnetization-Dependent T_c Shift in Ferromagnet/Superconductor/Ferromagnet Trilayers with a Strong Ferromagnet.* Phys. Rev. Lett., vol. **96**, 037004 (2006).

[87] Singh A., Sürgers C., Löhneysen, H. v. *Superconducting spin switch with perpendicular magnetic anisotropy.* Phys. Rev. B, vol. **75**, 024513 (2007).

[88] Zhu J., Krivorotov I. N., Halterman K., Valls O. T. *Angular Dependence of the Superconducting Transition Temperature in Ferromagnet-Superconductor-Ferromagnet Trilayers.* Phys. Rev. Lett., vol. **105**, 207002 (2010).

[89] Leksin P. V., Garif'yanov N. N., Garifullin I. A., Fominov Ya. V., Schumann J., Krupskaya Y., Kataev V., Schmidt O. G., Büchner B. *Evidence for Triplet Superconductivity in a Superconductor-Ferromagnet Spin Valve.* Phys. Rev. Lett., vol. **109**, 057005 (2012).

[90] Banerjee N., Smiet C. B., Smits R. G. J., Ozaeta A., Bergeret F. S., Blamire M. G., Robinson J. W. A. *Evidence for spin selectivity of triplet pairs in superconducting spin valves.* Nat. Comm., vol. **5**, 3048 (2014).

[91] Jara A. A., Safranski C., Krivorotov I. N., Wu C.-T., Malmi-Kakkada A. N., Valls O. T., Halterman K. *Angular dependence of superconductivity in superconductor/spin-valve heterostructures.* Phys. Rev. B, vol. **89**, 184502 (2014).

[92] Singh A., Voltan S., Lahabi K., Aarts J. *Colossal Proximity Effect in a Superconducting Triplet Spin Valve Based on the Half-Metallic Ferromagnet* CrO_2. Phys. Rev. X, vol. **5**, 021019 (2015).

[93] Kamashev A. A., Garif'yanov N. N., Validov A. A., Schumann J., Kataev V., Büchner B., Fominov Ya. V., Garifullin I. A. *Superconducting spin-valve effect in heterostructures with ferromagnetic Heusler alloy layers.* Phys. Rev. B, vol. **100**, 134511 (2019).

[94] Westerholt K., Sprungmann D., Zabel H., Brucas R., Hjörvarsson B., Tikhonov D. A., Garifullin I. A. *Superconducting Spin Valve Effect of a V Layer Coupled to an Antiferromagnetic* [Fe/V] *Superlattice.* Phys. Rev. Lett., vol. **95**, 097003 (2005).

[95] Deutscher G., Meunier F. *Coupling Between Ferromagnetic Layers Through a Superconductor.* Phys. Rev. Lett., vol. **22**, 395-396 (1969).

[96] Gu J. Y., You C.-Y., Jiang J. S., Pearson J., Bazaliy Ya. B., Bader S. D. *Magnetization-Orientation Dependence of the Superconducting Transition Temperature in the Ferromagnet-Superconductor-Ferromagnet System:* CuNi/Nb/CuNi. Phys. Rev. Lett., vol. **89**, 267001 (2002).

[97] Gu Y., Halász G. B., Robinson J. W. A., Blamire M. G. *Large Superconducting Spin Valve Effect and Ultrasmall Exchange Splitting in Epitaxial Rare-Earth-Niobium Trilayers.* Phys. Rev. Lett., vol. **115**, 067201 (2015).

[98] Kamra L. J., Chourasia S., Bobkov G. A., Gordeeva V. M., Bobkova I. V., Kamra A. *Complete* T_c *suppression and Néel triplets mediated exchange in antiferromagnet-superconductor-antiferromagnet trilayers.* Phys. Rev. B, vol. **108**, 144506 (2023).

[99] Balatsky A. V., Vekhter I., Zhu Jian-Xin *Impurity-induced states in conventional and unconventional superconductors.* Rev. Mod. Phys., vol. **78**, 373-433 (2006).

[100] Yu L. *Bound state in superconductors with paramagnetic impurities.* Acta Phys. Sinica, vol. **21**, 75-91 (1965).

[101] Shiba H. *Classical Spins in Superconductors.* Prog. Theor. Phys., vol. **40**, 435-451 (1968).

[102] Rusinov A. I. *On the Theory of Gapless Superconductivity in Alloys Containing Paramagnetic Impurities.* Sov. Phys. JETP, vol. **29**, 1101 (1969).

[103] Nadj-Perge S., Drozdov I. K., Li J., Chen H., Jeon S., Seo J., MacDonald A. H., Bernevig B. A., Yazdani A. *Observation of Majorana fermions in ferromagnetic atomic chains on a superconductor.* Science, vol. **346**, 602-607 (2014).

[104] Pawlak R., Kisiel M., Klinovaja J., Meier T., Kawai S., Glatzel T., Loss D., Meyer E. *Probing atomic structure and Majorana wavefunctions in mono-atomic Fe chains on superconducting Pb surface.* npj Quant. Inform., vol. **2**, 16035 (2016).

[105] Schneider L., Beck P., Posske T., Crawford D., Mascot E., Rachel S., Wiesendanger R., Wiebe J. *Topological Shiba bands in artificial spin chains on superconductors.* Nat. Phys., vol. **17**, 943-948 (2021).

[106] Gor'kov L. P., Rashba E. I. *Superconducting 2D System with Lifted Spin Degeneracy: Mixed Singlet-Triplet State.* Phys. Rev. Lett., vol. **87**, 037004 (2001).

[107] Annunziata G., Manske D., Linder J. *Proximity effect with noncentrosymmetric superconductors.* Phys. Rev. B, vol. **89**, 174514 (2012).

[108] Bergeret F. S., Tokatly I. V. *Singlet-Triplet Conversion and the Long-Range Proximity Effect in Superconductor-Ferromagnet Structures with Generic Spin Dependent Fields.* Phys. Rev. Lett., vol. **110**, 117003 (2013).

[109] Bergeret F. S., Tokatly I. V. *Spin-orbit coupling as a source of long-range triplet proximity effect in superconductor-ferromagnet hybrid structures.* Phys. Rev. B, vol. **89**, 134517 (2014).

[110] Edelstein V. M. *Triplet superconductivity and magnetoelectric effect near the s-wave-superconductor – normal-metal interface caused by local breaking of mirror symmetry.* Phys. Rev. B, vol. **67**, 020505 (2003).

[111] Edelstein V. M. *Influence of an interface double electric layer on the superconducting proximity effect in ferromagnetic metals.* JETP Lett., vol. **77**, 182-186 (2003).

[112] Jacobsen S. H., Ouassou J. A., Linder J. *Critical temperature and tunneling spectroscopy of superconductor-ferromagnet hybrids with intrinsic Rashba-Dresselhaus spin-orbit coupling.* Phys. Rev. B, vol. **92**, 024510 (2015).

[113] Ouassou J. A., Di Bernardo A., Robinson J. W. A., Linder J. *Electric control of superconducting transition through a spin-orbit coupled interface.* Sci. Rep., vol. **6**, 29312 (2016).

[114] Simensen H. T., Linder J. *Tunable superconducting critical temperature in ballistic hybrid structures with strong spin-orbit coupling.* Phys. Rev. B, vol. **97**, 054518 (2018).

[115] Banerjee N., Ouassou J. A., Zhu Y., Stelmashenko N. A., Linder J., Blamire M. G. *Controlling the superconducting transition by spin-orbit coupling.* Phys. Rev. B, vol. **97**, 184521 (2018).

[116] Johnsen L. G., Banerjee N., Linder J. *Magnetization reorientation due to the superconducting transition in heavy-metal heterostructures.* Phys. Rev. B, vol. **99**, 134516 (2019).

[117] González-Ruano C., Johnsen L. G., Caso D., Tiusan C., Hehn M., Banerjee N., Linder J., Aliev F. G. *Superconductivity-induced change in magnetic anisotropy in epitaxial ferromagnet-superconductor hybrids with spin-orbit interaction.* Phys. Rev. B, vol. **102**, 020405 (2020).

[118] González-Ruano C., Caso D., Johnsen L. G., Tiusan C., Hehn M., Banerjee N., Linder J., Aliev F. G. *Superconductivity assisted change of the perpendicular magnetic anisotropy in V/MgO/Fe junctions.* Sci. Rep., vol. **11**, 19041 (2021).

[119] Bobkov G. A., Bobkova I. V., Golubov A. A. *Magnetic anisotropy of the superconducting transition in superconductor/antiferromagnet heterostructures with spin-orbit coupling.* Phys. Rev. B, vol. **108**, L060507 (2023).

Editor's note: We invite readers to explore the philosophy of the Journal [V. Stolyarov, Mesosci. Nanotechnol., vol. 1, 01001 (2023)] and consider the possibility of submitting their contributions for publication in our Journal.

DOI: 10.64214/jmsn.01.01005 Review

Contemporary implementations of spiking bio-inspired neural networks

Andrey E. Schegolev,[1 2] Marina V. Bastrakova,[3] Michael A. Sergeev,[3] Anastasia A. Maksimovskaya[1,5]
Nikolay V. Klenov,[4,5] Igor I. Soloviev[1,5]

[1] *Skobeltsyn Institute of Nuclear Physics, Lomonosov Moscow State University, 119991 Moscow, Russia*
[2] *Moscow Technical University of Communication and Informatics (MTUCI), 111024 Moscow, Russia*
[3] *Faculty of Physics, Lobachevsky State University of Nizhny Novgorod, 603950 Nizhny Novgorod, Russia*
[4] *Faculty of Physics, Lomonosov Moscow State University, 119991 Moscow, Russia*
[5] *Dukhov All-Russia Research Institute of Automatics, Moscow 101000, Russia*

submitted 02 May 2024, accepted 13 October 2024, published 5 December 2024

The extensive development of the field of spiking neural networks has led to many areas of research that have a direct impact on people's lives. As the most bio-similar of all neural networks, spiking neural networks not only allow for the solution of recognition and clustering problems (including dynamics), but they also contribute to the growing understanding of the human nervous system. Our analysis has shown that hardware implementation is of great importance, since the specifics of the physical processes in the network cells affect their ability to simulate the neural activity of living neural tissue, the efficiency of certain stages of information processing, storage and transmission. This survey reviews existing hardware neuromorphic implementations of bio-inspired spiking networks in the "semiconductor", "superconductor", and "optical" domains. Special attention is given to the potentials for effective "hybrids" of different approaches.

List of main acronyms

AI: artificial intelligence; ANN: artificial neural network; CNN: convolutional neural network; CMOS: complementary metal-oxide semiconductor; DFB-SL: distributed feedback semiconductor laser; HH: Hodgkin-Huxley; ISI: inter-spike interval; JJ: Josephson junction; LIF: leaky integrate-and-fire; NIST: National Institute of Standards and Technology; ONN: optical neural network; PCM: phase change materials; QPSJ: quantum phase-slip junction; RFF: receptive fields filter; RSFQ: rapid single-flux-quantum; SFQ: single-flux quantum; SNN: spiking neural networks; STDP: spike-timing dependent plasticity; SQUID: superconducting quantum interference device; VCSEL: vertical-cavity surface-emitting laser; XOR: exclusive OR logical operator.

1 Introduction

The last decade has demonstrated a significant increase in interdisciplinary research in neuroscience and neurobiology (this was reflected even in the decisions of the Nobel Committee[1,2] in 2024). The convergence of mathematics, physics, biology, neuroscience and computer science has led to the hardware realisation of numerous models that mimic the behaviour of living nervous tissue and reproduce characteristic neural patterns. Spiking neural networks (SNNs) have played a crucial role in these fields of knowledge. In these networks, neurons exchange short pulses (about 1-2 ms for bio-systems) of the same amplitude (about 100 mV for bio-systems).[3,4] SNNs come closest to mimic the activity of living nervous tissue (capable of solving surprisingly complex tasks with limiting resources) and have the greatest biosimilarity and bioinspirability.

Spiking neural networks use a completely distinct method of information transfer between neurons: they encode input data as a series of discrete-time spikes that resemble the action potential of biological neurons. In fact, the fundamental idea of SNNs is to achieve the closest possible biosimilarity and use it to solve specific tasks. These problems can be roughly divided into two groups: the first group is focused on solving traditional neural network challenges, with more emphasis on dynamic information recognition (speech, video), while the second group is aimed at imitating the nervous activity of living beings, reproducing characteristic activity patterns, recreating the work of the human brain. Currently, there is an ambitious project that aims to create a full-fledged artificial mouse brain.[5] Moreover, the second group includes such tasks as: using motor biorhythms for neural control in robotics,[6–8] controlling human movements (bioprosthetics, functional restoration of mobility),[9] understanding learning processes and memory effects,[10–12] creating brain-computer interfaces,[13–17] etc.

Therefore, hardware development of bio-inspired SNN is very vital and promising. For this reason, it is crucial to recognise the current progress and conditions for the development of this field, taking into account the immense amount of information that is growing every day. Moreover, in terms of signalling, SNN is better suited to hardware implementation than artificial neural network (ANN), since neurons are only active at the time when a voltage spike is generated, which reduces the overall power consumption of the network and simplifies computation.

Figure 1 illustrates the intensification of work on the topic over the last decades. This is the period with a significant increase in publication activity. Here we show the analysis of publication activity (indexed in Dimensions and OpenAlex databases) on the topic of spiking neural networks and on the topic of spiking neural networks filtered by the keywords 'bio-inspired'. Since around 2016, there has been a significant increase in interest in the topic of spiking neural networks as well as in the topic of bio-inspired networks. All studies presented in these publications have been carried out for different implementations of SNNs: software, CMOS (especially memristor-based), superconducting, optical, and hybrid ones.

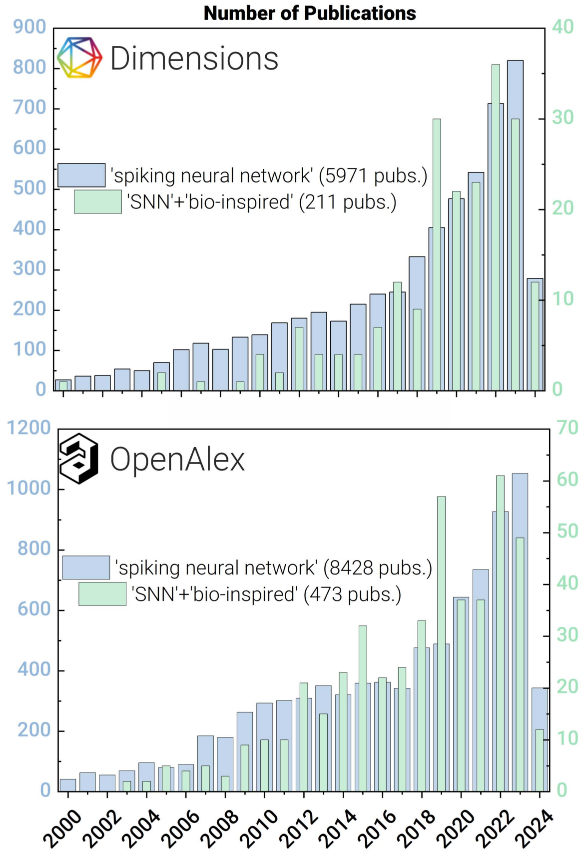

Figure 1. The histograms illustrating the number of the publications based on data from Dimensions and OpenAlex databases from a search on the topic ”spiking neural network” (light-blue histogram) and a search filtered by the keyword “bio-inspired” (light-green histogram), presented retrospectively from the year 2000.

In this paper we review the advances in different hardware directions of bio-inspired spiking neural network evolution and provide a brief summary of the future of the field, its advantages, challenges, and drawbacks. Furthermore we have reviewed the basic software implementations of SNNs.

The first part of this review is devoted to the mathematical foundations of bio-inspired spiking neural networks, their idea and software realisation. The second part is dedicated to the CMOS-based bio-inspired neuromorphic circuits, where we have talked about semiconducting and memristive realisations. The third part is devoted to superconducting realisations, not of the whole network, but of its elements and some of its functional parts. Finally, we have considered bio-inspired elements for optical neuromorphic systems and provide a brief discussion of each area of activity as well as a general conclusion on the evolution of bio-inspired neuromorphic systems.

The brief conclusion is that there is no single approach that has overwhelming advantages at the current moment, and it is quite likely that the necessary direction of development of the field has not yet been found. However, we can already say with certainty that the hybrid approach can provide some success in the formation of complex deep spiking neuromorphic networks.

2 Mathematical fundamentals of bio-inspired spiking neural networks

A spiking neural network is fundamentally different from the second generation of neural networks: instead of continuously changing values over time, such a network works with discrete events (chains of events) that occur at specific points in time. Discrete events are encoded by impulses (spikes) received at the input of the neural network and processed by it in a specific way, as shown in figure 2. The output of such a network is also a sequence of spikes, encoding the result of the network's activity. In a real neuron, the transmission of impulses is described by differential equations that correspond to the physical and chemical processes of action potential formation. When the action potential reaches its threshold, the neuron generates a spike and the membrane potential returns to its initial level, see figure 2a. An accurate representation of neuronal activity and its response to various input signals requires a general mathematical model that describes all the necessary processes associated with its spike activity and action potential formation, while remaining sufficiently simple for its successful use in various applications.

2.1 Mathematical models of bio-inspired neurons and networks

Hodgkin-Huxley model

The discussion of applications begins with the simplest and most studied software implementations of SNNs: the most popular way to describe the initiation and propagation of action potentials in neurons is the Hodgkin-Huxley (HH) model.[18]

The HH model is treated as a conductance-based system where each neuron is a circuit of parallel capacitors and resistors[19] and describes how action potential in nerve cells (neurons) is emerged and propagated. Basically, the HH model contains[20] four components of the current flowing through the neuron membrane, formed by lipid bilayer and possessing of potential V_m: the current flowing through the lipid bilayer (I_c), currents flowing through the ion channels (I_{Na} and I_{K}), and the leakage current (I_l). The lipid bilayer – nerve cell membrane – is introduced in the form of the capacitance C_m, ion-gated channel – by the conductance g_i (where i is a corresponding ion) per unit area and leakage current introduced by the conductance g_l per unit area. Thus, for a cell model that contains only sodium and potassium ion channels, the total current flowing through the membrane is described by the following equation

$$I = C_m \frac{dV_m}{dt} + g_{\mathrm{K}}(V_m - V_{\mathrm{K}}) + g_{\mathrm{Na}}(V_m - V_{\mathrm{Na}}) + g_l(V_m - V_l). \quad (1)$$

Of course, the biochemical processes in the living nerve cell are more complicated and therefore the HH model could be modified by adding extra terms for other ions (Cl^- or Ca^{++}, for example) or by using non-linear conductance models ($g_i = f(t, V)$) instead of constant values.

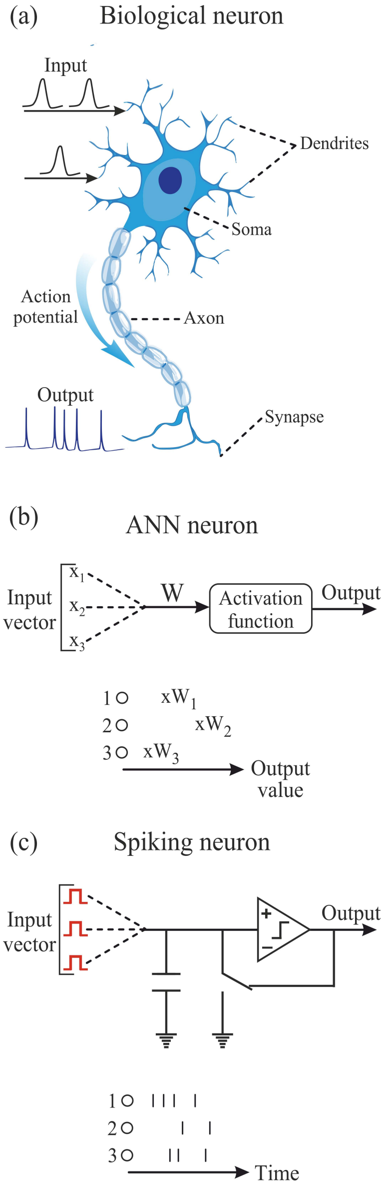

Figure 2. **a** – Illustration of a biological neuron and its operating principles. **b** – Conventional ANN operating principle (top) and output representation (bottom). The input vector is processed by multiplying the input vector by the corresponding weight vector (denoted W) and then passing it to the activation function. Output values are represented in floating-point numbers that can be processed at the software level. **c** – Operating principle of a spiking neural network (top) and output representation (bottom). The input signal is processed by the hardware implementation of the neuron. Output values are represented in spike trains, which differ in the emission time of each spike and the overall density, and also serve as inherent memory. These images were adapted from Ref. [21] and recomposed by authors.

Izhikevich model

One of the most computation-efficient and simultaneously accurately representative for neurons' activity is the Izhikevich model. According to Ref. [23], bifurcation methodologies[24] enable us to reduce many biophysically accurate Hodgkin-Huxley-type neuronal models to two-dimensional (2D) system of ordinary differential equa-

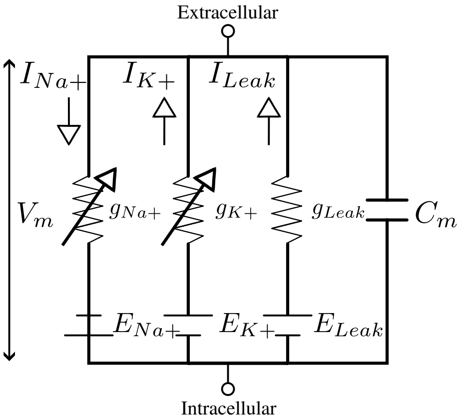

Figure 3. Electrical analog of the Hodgkin-Huxley model (this figure is adapted from Ref. [22]). The capacitance C_m represents a lipid bilayer – neuron membrane with potential V_m. Non-linear electrical conductances resemble voltage-gated ion channels $g_{\mathrm{K}+}$ and $g_{\mathrm{Na}+}$, while g_{Leak} corresponds to the leakage channel. Parameters $E_{\mathrm{Na}+}$, $E_{\mathrm{K}+}$, and E_{Leak} correspond to the reversal ions potentials and leak reversal potential, respectively.

tions

$$\begin{cases} \dot{v} = 0.04v^2 + 5v + 104 - u + I, \\ \dot{u} = a\,(bv - u), \end{cases} \tag{2}$$

with the auxiliary after-spike resetting

$$\text{if} \quad v \geq 30 \text{ mV}, \quad \text{then} \quad \begin{cases} v \leftarrow c, \\ u \leftarrow u + d. \end{cases} \tag{3}$$

Here, v and u are variables, a, b, c, and d are parameters, and dot notation is time derivative. Neuron's membrane potential and recovery are described by v and u, and when v reaches its maximum value of $+30\,\mathrm{mV}$, u is restored, see Eq. (3). They are affected by the parameter b which describes recovery variable sensitivity to sub-threshold fluctuations of v, promoting possible low-threshold oscillations when increased. The case $b < a$ $(b > a)$ corresponds to saddle-node (Andronov-Hopf) bifurcation of the resting state.[25] Variable u is also affected by the parameter a which stands for the time scale of the variable, speeding up or slowing down recovery, and the parameter d, which is responsible for after-spike reset of u caused by slow high-threshold Na^+ and K^+ conductances. Fast high-threshold K^+ conductances affect on v is expressed in the remaining parameter c, that describes the after-spike reset value of v.

The combination $0.04v^2 + 5v + 140$ provides scaling for membrane potential v to mV and ms scales and was derived from fitting the initiation dynamics of the spike. The resting potential in the model[23] is between -70 and $-60\,\mathrm{mV}$ depending on the b parameter. But in real practice, the model does not have a fixed threshold, depending from the value of v before the spike formation.

Leaky Integrate-and-Fire Neuron Model

The really frequently used hardware model is implemented on principles of so-called Leaky Integrate-and-Fire (LIF) neurons. Such neurons, whose membrane potentials $\mathbf{V}$ evolve at time step t according to some variation of the following dynamics, described in following manner:[26]

$$\mathbf{V}[t] = \lambda \mathbf{V}[t-1] + \mathbf{W}\mathbf{X}[t] - \mathbf{S}[t]V_{th}, \tag{4}$$

where $\lambda \in [0, 1)$ is a membrane leakage constant, $\mathbf{X}$ is an input (*i.e.*, an external stimuli to the network or the spiking activity from another neuron), $\mathbf{W}$ is a weight matrix, and the binary spiking function

$$\mathbf{S}[t] = \begin{cases} 1, & \text{if} \quad \mathbf{V}[t] > V_{th} \\ 0, & \text{otherwise.} \end{cases} \tag{5}$$

is a function of the threshold voltage V_{th}.

2.2 Coding information in SNN

The brain of a living being processes a wide variety of information, which can come from different sensory organs as well as signals from the nervous system of different internal organs. How does the brain understand which signal comes from the optic nerve and which from the auditory nerve, for example? There are different ways of encoding incoming information, processing it by a specially trained neural network (a specific area in the brain) and interpreting the results of the processing. In other words, there are ways of encoding input and output signals. And both are very important: in the first case, the information is encoded so that the system can work with it, and in the second case, so that the general decision-making centre (the brain) can perceive or *handle* the processed information. Two types of coding are generally used in artificial SNNs: rate coding and temporal (or latency) coding, although there are others.[27]

Rate coding converts input information intensity into a "firing" rate or spike count. For example, a pixel in some image, that has a specific RGB code and brightness, can be converted or *coded* into a Poisson train – a sequence of spikes, based on this information (information of its intensity). There are several types of rate coding: count rate coding, density rate coding and population rate coding. In terms of output interpretation, the processing centre will select the one that has the highest "firing" rate or spike count at a particular point in time.

Another natural principle of information coding is a temporal (or latency) coding. One converts input intensity to a spike time, referring to spike timing and paying attention to time moment when the spike has occurred. The spike weighting ensures that different "firing" times lead to different amount of information. The earlier a spike arrives, the larger weight it carries, and the more information it transmits to the post-synaptic neurons. In terms of output interpretation, the processing centre selects the signal that, by a certain point in time, came first (selects the signal from that output neuron among other output neurons that fused first).

There is also another type of information coding called delta modulation. This type of coding consists of converting the incoming analogue information signal into a spike train of temporal changes in signal intensity (magnitude). For example, if the input signal is increasing, the network input will receive spikes at a certain frequency, which depends on the rate of increase of the signal (its derivative): the faster the signal increases in time, the more frequent the spikes is. Conversely, the signal decreasing will be accompanied by the absence of spikes.

2.3 SNN learning techniques

The complex dynamics of spike propagation over SNNs makes it difficult to design a learning algorithm that gives the best result. Currently, there are three main types of methods for training spiking neural networks, as referred in Ref. [27]: shadow training, backpropagation on spikes training and training based on local learning rules.

Shadow training

The idea of this shadow training technique is to use the training algorithms of a conventional ANN to build a spiking network by converting a trained ANN into a trained SNN. This process takes place as follows: first, the conventional ANN is trained, then the activation function of each neuron in the ANN is replaced by a separate operator that non-linearly transforms the signal incoming to the neuron by the spike frequency or by the delay between spikes. For example, conversion process from convolutional neural network to SNN can be done by manually reprogramming convolution kernel for spike train inputs in order to make the SNN produce the same output as the trained convolutional neural network (CNN).[28] At the same time, the net weights remain the same.

The main advantage of this training process is that the most of the time we deal with an ANN, with all of its benefits of training conventional neural networks. Such approach is used in tasks related to that of ANNs that aimed to image classification. Despite that, the process of converting activation functions into spike trains usually requires a large number of simulations time steps which may deteriorate the initial idea of spiking neuron energy efficiency. And, the most important one, is that conversion process is doing an approximation of activation, negatively affecting the performance of a SNN. The last further confirms the fact that other learning algorithms need to be developed to train SNNs, till then SNNs will remain just a shadow of ANNs.

Backpropagation training

Backpropagation training algorithm for ANNs can also be implemented for SNNs by calculating gradients of weight change for every neuron. Implementations of this algorithm for SNNs may vary since, according to original ANNs backpropagation the learning requires to calculate the derivative of the loss function. And as we know, the uses of derivative over spikes is not the best idea, because spikes generation depends on membrane threshold potential as a step-function and the derivative becomes infinite. To avoid this, backpropagation techniques for SNN take other neuron output signal parameters into account, *i.e.* backpropagation method using spikes utilises changes of spike timing rate according to the network weights change.

Backpropagation method has several advantages, such as the high performance on data-driven tasks, low energy consumption, and high degree of similarity with recurrent neural networks in terms of training process. Despite the similarity with well-established ANN backpropagation method, the drawbacks of backpropagation for SNNs method consist of several subjects. First of all, this method can not fully replicate effectiveness of optimising a loss function, meaning that there is still an accuracy gap between SNNs and ANNs, which remains to be closed up for today. Additionally, once neurons become inactive during the training process, their weights become frozen.

In some cases, there are alternative interpretations of this algorithm, for example, such as the forward propagation through time[29] (FPTT) which is used for recurrent SNN training. This algorithm is devoid of many drawbacks that follow conventional backpropagation algorithm, removing the dependence on partial gradients sum during the gradient calculation. The most peculiar feature of this algorithm is that along with regular loss it computes dynamic regularisation penalty, which is calculated on previously encountered loss value, transforming recurrent nertwork training to resemble feed-forward network training.

Local learning rules

Neurons are trained locally, treating local spatially and temporary signal as an input for a single neuron's weight update function. Namely, backpropagation technique deals only with finite sequences of data, restricting the temporal dependencies that can be learned. This algorithm also tries to compute gradients as it is done in backpropagation, but does it through the computations that make these gradient calculations temporally local. However, this algorithm demands significantly more computations in comparison with backpropagation, which rejects the possibility of this algorithm to replace conventional backpropagation despite being more biologically plausible.

The constraint imposed on brain-inspired learning algorithms is that the calculation of a gradient should, like the forward pass, be temporally local, *i.e.* that they only depend on values available at either present time. To address this, learning algorithms turn to their online counterparts that adhere to temporal locality. Real-time recurrent learning[30] (RTRL) proposed back in 1989 is one prominent example.

2.4 Towards hardware implementations of SNN

To extend the understanding of the concept of how spiking neural networks work, in this section we will review a schematic process of solving the problem of exclusive OR (XOR) logical operator with a SNN on an example presented in Ref. [31]. Since XOR is considered a fairly simple logic gate, it will serve as an excellent demonstration of SNN training and operation. In fact, operating with SNNs has almost the same challenges as in training ANNs: for example, which data representation to choose to effectively describe the problem, what structure should the network have, how to interpret the network output and so on. That is, we should guide our approach to a certain problem in the same way as it is done in ANNs on the general scope, including the XOR problem.

The training process for the chosen task can be separated into several steps:

- Neuron model
  Due to low complexity of this task, it is most efficient to use a simple neuron model as well. In that case, the LIF model suits this problem the best because its easy to control and does not produce unwanted complexity.

- Data representation
  Since we test the possibility of creating a network of spiking neurons to perform logic gate operations, the input data can be simply labeled in two inputs. Each input has to carry its own representative frequency in order to be separable for the network. Taking these statements into account, we can (for example) define the frequency input values as 25 Hz for the Boolean Zero ("0") and 51 Hz for the Boolean One ("1"). These values are chosen as they are decisively different from each other and can be clearly represented visually.

- Structure
  The neural network structure represents the logic gate as follows: two input neurons that encode any combination of "0" and "1", hidden layer neurons represent any possible combination of 0's and 1's, and output layer produces the predicted output, as shown in figure 4.

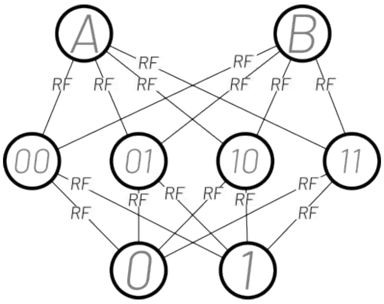

Figure 4. SNN architecture for the XOR problem solving (this figure was adapted from Ref. [31]). Input neurons A and B can receive any combination of "0" and "1". Each RF block demonstrates Receptive Field application to neuron input/output. The number on hidden neurons layer represent the combination of "0" and "1" they implied to respond to.

- Receptive fields filter (RFF)
  To strengthen the response for designated frequencies for the corresponding neurons, RFF is added to every hidden layer neurons' connections. Adding the RFF helps neurons to detect particular frequencies, filtering the ones that are outside their response range. The RFF formula[31] is $k_{ij} = \exp(-(x_m - y_0)^2/d_m^2)$ where k_{ij} is a scalar variable which will modify the output spike train frequency of the related neuron, x_m is the operating frequency of the RFF, y_0 is the input spike train frequency to the RFF and d_m denotes the width of the RFF, allowing the filter to distinguish more frequencies.

- Input encoding
  The input frequencies are encoded into linear spike trains, i.e. the value of the distance between the action potentials, known as the inter-spike interval (ISI), is treated to be a constant. The network was designed to take advantage of the precise timing between action potentials. If the ISIs on input A are synchronised with the ISIs on input B, it means that both inputs have identical frequency.

- Training
  Usage of RFF is an effective and biologically plausible way to reduce complexity and fault vulnerability in this problem. Because of that, as well as small number of neurons, manual fine-tuning of thresholds and weights will be enough to train the network to produce accurate results, successfully recognising all possible XOR combinations. However, upon increasing the size of the network, implementing one of network training algorithms will be inevitable.

For conclusion to this example it is important to highlight that one should pay attention to training process workflow and investigate the problem deeply to be able to recognise all the obstacles that may be encountered during training (*i.e.* in the XOR problem proper signal frequency interpretation would not be possible without RFF). Considering the training workflow, the most important parts of this are the neuron model and input/output coding, since it can determine crucial aspects of problem interpretation from network implementation's point of view. Conversely, network training algorithms for weights optimisation play lesser role in this process, because they can only affect computational complexity to be performed and their influence on results accuracy becomes noticeable only if the task implies implementing state-of-art network or results close to it.

3 CMOS-based bio-inspired neuromorphic circuits

The last decades of electronics and electrical engineering are clearly associated with the development of the conventional complementary metal-oxide-semiconductor (CMOS) technology.[32, 33] Semiconductors are well established in many devices that we use 7 days a week, all year round. It is therefore not surprising to see variations in the hardware implementation of SNNs based on semiconductor elements. Globally, all CMOS SNN implementation options can be divided into two parts, with the focus on either transistors or memristors. Examples of semiconductor implementations of neuron circuits are shown in figure 5. Two CMOS solutions for implementing the functions of the single neuron model developed by

IBM (for TrueNorth) and Stanford University (for Neurogrid) are presented here. In both cases, the realisation of the functions of even a single neuron (more precisely, the neuron soma) requires the involvement of a large number of elements.

3.1 Silicon-based neuron: operation

As might be expected, the realisation of spike sequence generation in CMOS technology differs from the way it is done in software models. Since semiconductor circuits operate with voltage levels, generating a spike as a nonlinear voltage response requires some tricks. To better understand how SNNs work at the hardware level and how spike formation occurs, let us briefly review the operation of the basic elements of such networks, which are isomorphic to ion-gated channels.[32, 36]

Realisation of ion-gated mechanisms

The goal of creating semiconductor models of neuromorphic spiking neural networks is to reproduce the biochemical dynamics of ionic processes in living cells. The first step is to reproduce the ion-gated channels responsible for the different voltage response patterns. The HH neuron model discussed above is essentially a thermodynamic model of ion channels. The channel model consists of a number of independent gating particles that can adopt two states (open or closed) which determine the permeability of the channel. The HH variable represents the probability that a particle is in the open state or, in population terms, the fraction of particles in the open state.

In a steady state, the total number of opening particles (the opening flux, which depends on the number of closed channels and the opening rate) is balanced by the total number of closing particles (the closing flux). A change in the membrane voltage (or potential) causes an increase in the rate of one of the transitions, which in turn causes an increase in the corresponding flux of particles, thereby modifying the overall state of the system. The system will then reach a new steady state with a new ratio of open to closed channels, thus ensuring that the fluxes are once again in equilibrium.

This situation becomes even clearer if we consider it from the perspective of energy balance. Indeed, a change in the voltage on the membrane is equivalent to a change in the electric field across it. Then the equilibrium state of the system depends on the energy difference between the particles in the different states: if this difference is zero and the transition rates are the same, the particles are equally distributed between the two states. Otherwise, the state with lower energy will be preferred and the system will tend to move to it. Note that in the HH model, the change in the population of energy states is exponential in time. A similar situation is with the density of charge carriers at the source and drain of the transistor channel, the value of which also depends exponentially on the size of the energy barriers. These energy barriers exist due to the inherent potential difference (electric field) between the channel and the source or drain. Varying the source or drain voltage changes the energy level of the charge carriers.

The similarity of the physics underlying the operation of neuronal ion channels and transistors allows us to use transistors as thermodynamic imitators of ion channels. In both cases, there is a direct relationship between the energy barrier and the control voltage. In an ion channel, isolated charges must overcome the electric field generated by the voltage across the membrane. For a transistor, electrons or holes must overcome the electric field created by the voltage difference between the source, or drain, and the transistor channel. In both of these cases, the charge transfer across the energy barrier is governed by the Boltzmann distribution, resulting in an exponential voltage dependence.[37] To model the closing and opening fluxes, we need to use at least two transistors, the difference of signals from which must be integrated to model the state of the system as a whole. A capacitor (C_u) does the integration, assuming that the charge represents the number of particles and the current represents the flux. The voltage on this capacitor is linearly proportional to its charge gives the result. In 2007 Hynna and Boahen suggested the following circuit (figure 6 to simulate a voltage-driven ion channel. Each transistor defines an energy barrier for one of the transition rates: transistor $N1$ uses its source and gate voltages (u_L and V_{CLOSE}, respectively) to define the closing rate, and transistor $N2$ uses its drain and gate voltages (u_H and V_{OPEN}) to define the opening rate (where $u_H > u_L$). The difference in transistors currents is collected on the capacitor C_u. The magnitude of the energy barriers is independent of the capacitor voltage u_V, so the value of u_V indicates the fraction of open channels and increases as the particles switch more and more to the open state. The variable's steady-state value changes sigmoidally with membrane voltage, dictated by the ratio of the opening and closing rates.

Integrate-and-fire neuron realisation

Now we are ready to understand the membrane voltage and spike formation. The explanation of these processes will be conducted based on a model of an integrate-and-fire neuron realised using MOSFETs ($M1$, $M2$, $M3$), capacitance (C_{mem}) and $p-n-p-n$ diode ($D0$),[38] shown in figure 7a. The designated components perform the following roles: C_{mem} contributes to the increase in the membrane voltage (V_{mem}); $D0$ generates spike voltages (V_{SPIKE}); $M1$ acts as a resistor and the resistance contributes to the determination of the V_{SPIKE} value; $M2$ and $M3$ are responsible for resetting the spiking and membrane voltages, respectively.

The presented neuron circuit operation begins with the flow of synaptic current pulses (step 1) from presynaptic devices into the neuron circuit. Charges carried by the input current are integrated into C_{mem}. The temporal integration of charges increases V_{mem} which is the anode voltage of $D0$ (step 2). V_{SPIKE} is abruptly generated when V_{mem} reaches a triggering threshold voltage for the latch-up of the anode current of the diode (step 3).

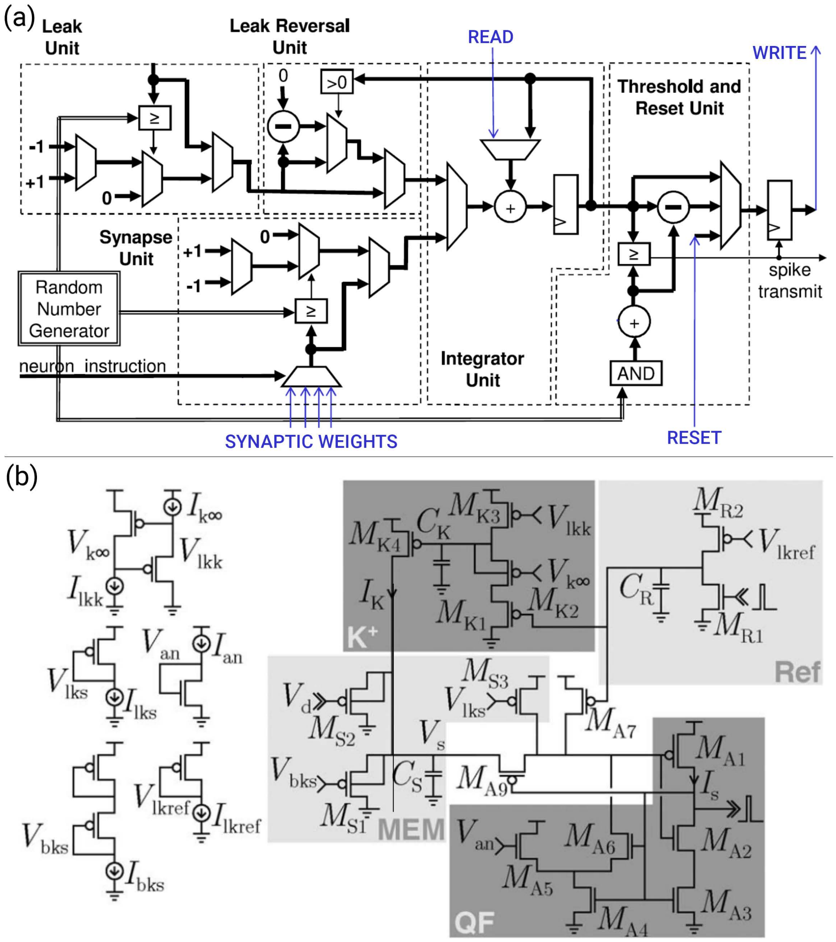

Figure 5. Semiconductor solutions for realising bio-inspired neuron functions: **a** – TrueNorth neuron circuit, **b** – Neurogrid neuron's soma circuit. These images were adapted from Refs. [34] and [35].

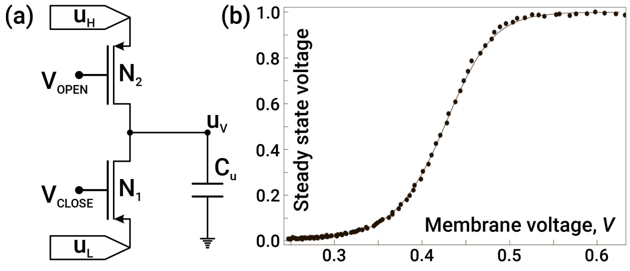

Figure 6. **a** – Voltage-dependent silicon ion channel model based on two transistors. **b** – Simulation of steady state voltage level (u_V) versus the membrane voltage (V). Note that V_{OPEN} and V_{CLOSE} are proportional to V and $-V$ respectively. These images were adapted and modified from Ref. [37].

The V_{SPIKE} value is determined by the voltage division of the diode and $M1$. The generation of V_{SPIKE} supplies the gate voltages to $M2$ and $M3$ and opens the channels of these transistors (step 4). The discharge current flows from C_{mem} to the ground through the M3 channel (step 5), and this flow rapidly decreases V_{mem} (step 6). Simultaneously, the reset current flows from the cathode of $D0$ to the ground through the $M2$ channel (step 5). Eventually, the opening of the $M2$ and $M3$ channels resets the anode and cathode voltages to zero (step 6), and accordingly V_{SPIKE} becomes zero. Thus, the latch-up of $D0$ and the subsequent opening of the $M2$ and $M3$ channels cause the presented neuron circuit to fire V_{SPIKE} pulses toward post-synaptic devices.[38]

Figure 7b illustrates the manner in which the membrane current changes with the membrane voltage during the charging and discharging of C_{mem}. We can see that the neuron circuit mimics the (1) temporal integration, (2) trigger threshold, (3) depolarisation, (4) repolarisation and (5) refractory period of a biological neuron. The membrane current does not flow during the temporal integration of charges in C_{mem} (step 1 in figure 7). When the temporal integration reaches the threshold voltage (steps 2 and 4), the membrane current increases abruptly (step 3). This moment corresponds to the depolarisation of the electrical action potential in a biological neuron. Discharging C_{mem} after depolarisation (step 5) results in a rapid and then gradual decrease in membrane current (step 6), which corresponds to the repolarisation of the electrical action potential in a biological neuron. As the membrane current becomes negligible, the presented neuron circuit remains in the refractory period.[38]

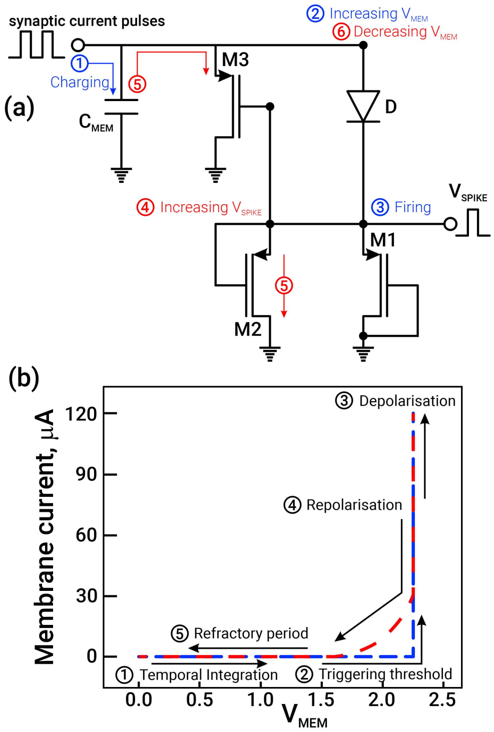

Figure 7. **a** – Integrate-and-fire neuron circuit with the illustration of the operation mechanism. **b** – The dependence of membrane current on membrane voltage. These images were adapted and modified from Ref. [38].

Izhikevich neuron model with silicon-based realisation

In 2008 Wijekoon and Dudek [39] suggested the circuit that implements the cortical neuron (figure 8), inspired by the mathematical neuron model proposed by Izhikevich in 2003. The circuit contains 14 MOSFETs, based on which three blocks are operating: membrane potential circuitry (transistors $M1$ – $M5$ and the capacitance C_v), slow variable circuitry (transistors $M1$, $M2$ and $M6$ – $M8$) and comparator circuitry ($M9$ – $M14$). C_v integrates a positive feedback current that generate spikes (generated by $M3$ and flowing from one to C_v), leakage current (generated by $M4$) and post-synaptic input current (excitatory or inhibitory). If a spike is generated, it is detected by the comparator circuit which provides a reset pulse on the gate of $M5$ that rapidly hyperpolarises the membrane potential (V on C_v) to a value determined by the voltage at node c. The transistor $M5$ size is designed so that the capacitor C_v is fully discharge during the voltage pulse coming from the comparator circuit by feedback loop (to the gate of $M5$).

The slow variable circuit works as follows. The magnitude of the current supplied by $M7$ is determined by the membrane potential (voltage at C_v), in a manner analogous to that observed in the membrane circuit. The scaling of transistors $M3$ and $M7$ ensures that the drain current of $M7$ is less than that of $M3$, while the capacitance value of C_u is selected to be greater than that of C_v. This guarantees that the potential at C_u varies more slowly than at C_v. The sum of these currents is integrated across the slow variable capacitor, designated as C_u. Additionally, following a membrane potential spike, the comparator (right part of figure 8) generates a voltage pulse (arriving at the base of $M8$) that opens the transistor, identified as $M8$. The modest dimensions of $M8$ and the brief duration of the voltage pulse that opens it guarantee that the capacitance C_u is not entirely reset to $V(dd)$. Instead, an additional quantity of charge, regulated by V_{dd}, is transferred to C_u. It can be demonstrated that each membrane spike results in a rapid increase in the slow variable potential. This, in turn, gives rise to an increase in the leakage current of the membrane potential, which in turn causes a slowing down of the depolarisation following the spike.

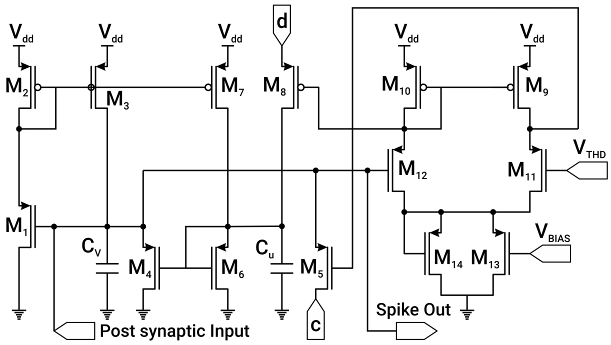

Figure 8. Illustration of the cortical neuron circuit, based on 14 MOSFETs and emulated Izhikevich neuron model. This figure was adapted and modified from Ref. [39].

In the comparator circuit, the voltage V_{THD} is responsible for detecting the membrane potential threshold when a spike is coming. The voltage V_{BIAS} controls the bias current in the comparator. When the membrane potential rises above V_{THD}, the voltage at the $M8$ gate is decreased and the voltage at the $M5$ gate is increased, generating reset signals. The reset signal is delayed, so the membrane potential V (in the membrane potential circuit at C_v) continues to rise beyond V_{THD}, up to V_{dd}, but as soon as the voltage at $M5$ gate is increased, the membrane potential is reset to V_c, which is lower than V_{THD}. Next, the voltages at the $M5$ and $M8$ gates return to their resting voltage levels, completing the reset pulses. Transistor $M14$ increases the comparator current during the spike, providing the required amplitude and duration of the reset pulse of the voltage at gate $M8$.[39]

The basic circuit comprises 202 neurons with different circuit parameters, including transistor and capacitance sizes. Fabrication was conducted using 0.35 μm CMOS technology. Since the transistors in this circuit operate mainly in strong inversion mode, the excitation patterns are on an ”accelerated” time scale, about 10^4 faster than biological real time. The power consumption of the circuit is less than 10 pJ per spike.[32, 39] Main types of characteristic firing patterns of suggested circuit are demonstrated in figure 9.

3.2 Transistor-based realisations

This section is devoted to reviewing such significant projects as SpiNNaker, Neurogrid, TrueNorth, NorthPole and Loihi.

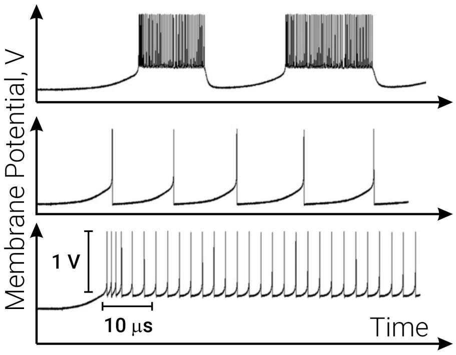

Figure 9. Experimental firing patterns obtained from the fabricated chip containing 202 neurons using 0.35 μm CMOS technology. Demonstrated patterns are responses to the input current step for various parameters of bias voltages at nodes c and d. This figure was adapted and modified from Ref. [39].

And despite the fact that at the moment of IBM's chip creation there were already such projects as SpiNNaker[40] (2012) and Neurogrid[35] (2014), we will start with the review of the TrueNorth neuromorphic processor, since in our opinion it was the first hardware implementation of the idea of neuromorphic computing.

TrueNorth

The field of brain-inspired technologies was marked in 2015 by the release of the first neuromorphic chip: IBM TrueNorth (figure 10a), a neuromorphic CMOS integrated circuit. The TrueNorth chip architecture is based on an organic neurobiological structure, but with the limitations of inorganic silicon technology. The main purpose of this platform was to reproduce the work of existing neural network algorithms of speech and image recognition in real time with minimal energy consumption.[34] This neuromorphic chip contains 4096 neurosynaptic nuclei combined into a two-dimensional array, and contains a total of 1 million neurons and 256 million synapses. The chip has a peak computing performance of 58 GSOPS with a power consumption of 400 GSOPS/W (here GSOPS means Giga-synaptic operations per second).

The use of the term "neuromorphic" itself implies that the chip is based on an architecture that differs from the familiar von Neumann architecture. Unlike von Neumann machines, the TrueNorth chip does not use sequential programs that map instructions into linear memory. The chip consists of spiking neurons, which are connected in a network and communicate with each other via spikes (voltage pulses). Communication between neurons is tunable, and the data transmitted can be encoded by the frequency, temporal and spatial distribution of the spikes. TrueNorth is designed for a specific set of tasks: sensory processing, machine learning and cognitive computing. However, just as in the early days of the computer age and the emergence of the first computer chips, the challenges of creating efficient neurosynaptic systems and optimising them in terms of programming models, algorithms and architectural features are still being solved. Currently, the IBM Truenorth chip is being used by DARPA (Defense Advanced Research Projects Agency) for gesture and speech recognition.

An IBM Research blog post on TrueNorth's performance notes that the classification accuracy demonstrated by the system is approaching the performance of 2016 state-of-art implementations, not only for image recognition but also for speech recognition. The[41] reports performance data for five digital computing architectures running deep neural networks. A single TrueNorth chip processes 1200-2600 32 × 32 colour images per second, consuming 170-275 mW, yielding an energy efficiency of 6100-7350 FPS (here FPS means frames per second). TrueNorth multi-chip implementations on a single board process 32×32 color images at 430-1330 per second and consume 0.89-1.5 W, yielding an energy efficiency of 360-1420 FPS/W. SpiNNaker delivers 167 FPS/W while processing 28×28 grayscale images (in a configuration of 48 chips on one board).[42] Tegra K1 GPU, Titan X Graphics processing unit (GPU) and Core i7 CPU deliver 45, 14.2 and 3.9 FPS/W, respectively, while processing 224×224 color images.[41,43]

SpiNNaker

The SpiNNaker (Spiking Neural Network Architecture) project, the brainchild of the University of Manchester, was unveiled in January 2012. It is a real-time microprocessor-based system optimised for the simulation of neural networks, and in particular spiking neural networks. Its main purpose is to improve the performance of software simulations.[40,44] SpiNNaker uses a custom chip based on ARM cores that integrates 18 microprocessors in 102 mm^2 using a 130 nm process. The all-digital architecture uses an asynchronous message-passing network (2D torus) for inter-chip communication, allowing the whole system to scale almost infinitely. In experiments[42,45,46] a 48-chip board (see figure 10d) was used, which can simulate hundreds of thousands of neurons and tens of millions of synapses, and consumes about 27-37 W in real time (for different neuron models a network configuration). On average, 2000 spikes formed into a Poisson train were used to encode a digit character from the MNIST dataset, with a classification latency of 20 ms.

In summary, SpiNNaker is a high-performance, application-specific architecture optimised for tasks from neurobiology and neuroscience in general. It is claimed that the system can also be used for other distributed computing applications such as ray tracing and protein folding.[45] The experimental studies performed suggest that for parallel modelling of deep neural networks, a dedicated multi-core architecture can indeed be energy efficient (compared to competitors and general purpose systems) while maintaining the flexibility of software-implementable models of neurons and synapses.

In 2021 the second generation of neuromorphic chip by the collaboration of Technische University of Dresden and University of Manchester was released – SpiNNaker2. Its development was conducted within the European Union flagship project "Human Brain Project". The overall approach utilised in the creation of SpiNNaker2 has the following parts: keep the processor-based flexibility of SpiNNaker1, don't do everything in software in the processors, use the latest technologies and features for energy efficiency and allow workload adaptivity on all levels.[44] One SpiNNaker2 chip consists of 152 advanced RISC machines (ARM) processors (processing elements) arranged in groups of four to quad-processing-elements which are connected by a Network-on-Chip (NoC) to allow scaling towards a large neuromorphic System-on-Chip (SoC). The full-scale SpiNNaker2 will consist of 10 million ARM cores distributed across 70000 chips in 10 server racks. We'd also highlight that the second generation is designed on a different technical process. Specifically, SpiNNaker1 was realised on 130 nm CMOS, while SpiNNaker2 was realised on 22 nm fully depleted silicon on insulator (FDSOI) CMOS,[47] which allowed not only to increase the performance of a single chip as a whole, but also to improve power efficiency. It is stated that SpiNNaker2 enabling a 10× increase in neural simulation capacity per watt over SpiNNaker1. Among the potential applications for the SpiNNaker2 the following stand out: naturally, brain research and whole-brain modeling, biological neural simulations with complex plasticity rules (with spike-timing-dependent plasticity (STDP), for example), low-power inferencing for robotics and embedded artificial intelligence (AI), large-scale execution of hybrid AI models, autonomous vehicles, and other real-time machine learning applications.

Neurogrid

The Neurogrid project, carried out at Stanford University in December 2013,[48] is a mixed analogue-digital neuromorphic system based on a 180 nm CMOS process. The project has two main components: software for interactive visualisation and hardware for real-time simulation. The main application of Neurogrid is the real-time simulation of large-scale neural models to realise the function of biological neural systems by emulating their structure.[35]

The hardware part of Neurogrid contains 16 Neurocores connected in a binary tree: microelectronic chips with a 12×14 mm^2 die containing 23 million transistors and 180 pads; a Cypress Semiconductor EZ-USB FX2LP chip that handles USB communication with the host; a Lattice ispMACH CPLD. This makes it possible to establish a link between the data transmitted via USB and the data driven by Neurogrid, and to interleave timestamps with the outgoing data (host binding). A daughter board is responsible for primary axonal branching and is implemented using a field-programmable gate array (FPGA). The Neurogrid board is shown in figure 10c. Each Neurocore implements a 256×256 silicon neuron array, and also contains a transmitter, a receiver, a router, and two RAMs. A neuron has one soma, one dendrite, four gating variables and four synapse populations for shared synaptic and dendritic circuits.[35]

The Neurogrid's architecture enables to simulate cortical models emulating axonal arbors and dendritic trees: a cortical area is modeled by a group of Neurocores mentioned above and an off-chip random-access memory is programmed to replicate the neocortex's function-specific intercolumn connectivity.[49] Therefore, it is indeed simulate the behaviour of large neural structures, including conductance-based synapses, active membrane conductances, multiple dendritic compartments, spike backpropagation, and cortical cell types. No data is available on the power consumption of image recognition, as in the case of TrueNorth or SpiNNaker, but that's understandable: the main purpose of the project is to model the neural activity of living tissues, and that's what it does. One thing we can say for sure is that the neurogrid consumes less power than the GPU for the same simulation: 120 pJ versus 210 nJ per synaptic activation.[50] This confirms the thesis that digital simulation (on CPUs or GPUs), even though it allows solving such problems, but the time and power consumption will be significant compared to specialised architectures.

NorthPole

A striking example of a hardware implementation of a semiconductor bio-inspired neural network is the recently (2023) introduced NorthPole chip from IBM[51] (figure 10b). NorthPole is an extension of TrueNorth, and it's not surprising that it inherits some of the technology used there. The NorthPole architecture is designed for low-precision, common-sense computing while achieving state-of-the-art inference accuracy for neural networks. It is optimised for 8-, 4- and 2-bit precision, eliminating the need for high precision during training. The NorthPole system consists of a distributed modular array of cores, with each core capable of massive parallelism, performing 8192 2-bit operations per cycle. Memory is distributed between and within the cores, placing it in close proximity to the computation. This proximity allows each core to take advantage of data locality, resulting in improved energy efficiency. NorthPole also incorporates a large on-chip memory area that is neither centralised nor hierarchically organised, further enhancing its efficiency.

Potentially, the NorthPole chip opens up new ways for the development of intelligent data processing for tasks such as optimisation (of systems, algorithms, scalability, etc.), for image processing for digital machine vision, and data recognition for autopilots, medical applications, etc. Also the chip was run in such well-known tests as ResNet-50 image recognition and YOLOv4 object detection models, where it showed outstanding results: higher energy and space efficiency, and lower latency than any other chip available on the market today, and is roughly 4000 times faster than TrueNorth (since the requirements to the accuracy of calculations in the chip are reduced, it is not possible to correctly estimate the specific performance). Ref.[51] provides the following data: NorthPole based on 12 nm node processing technology delivers 5 times more frames per joule than GPU NVIDIA H100 based on 4 nm technological process (571 vs. 116 frames/J) and 1.5 times more than the specialised for neural network use Qualcomm Cloud AI 100 based on 7 nm technological process. The reason for this is the local-

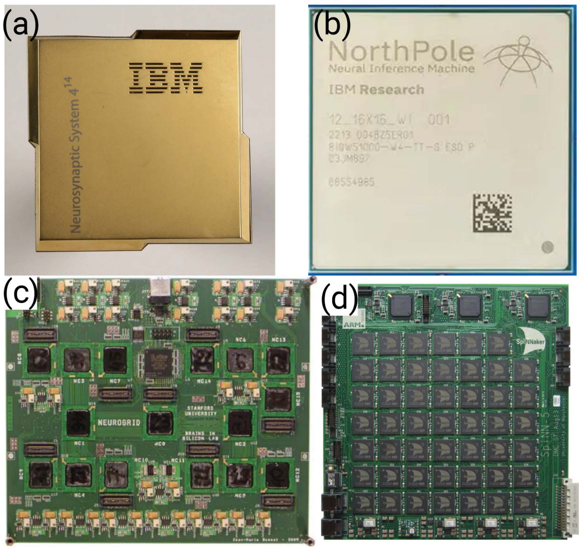

Figure 10. Images of some CMOS spiking neural network realisations: **a** – IBM TrueNorth chip,[34] **b** – IBM NorthPole chip,[51] **c** – Neurogrid board,[48] **d** – SpiNNaker (spiking neural network architecture), a massively parallel, manycore supercomputer architecture.[46]

ity of the computation – by eliminating off-chip memory and intertwining on-chip memory with compute memory, the locality of spatial computation is ensured and, as a result, energy efficiency is increased. Also low-precision operations further increase NorthPole's lead over its competitors.

Modha *et al.* [51] tested NorthPole only for use in computer vision. However, with this sort of potential, this chip can also be used for image segmentation and video classification. According to the information on the IBM's blog it was also tested in other areas, such as natural language processing (on the encoder-only BERT model) and speech recognition (on the DeepSpeech2 model).

Loihi and Loihi2

In 2018, Intel Labs unveiled the first neuromorphic manycore processor that enables on-chip learning and aims to model spiking neural networks in silicon. The name of this processor is Loihi (figure 11a). Technologically, Loihi is a 60 mm^2 chip manufactured in Intel's FinFET 14 nm process. The chip instantiates a total of 2.07 billion transistors and 33 MB of static random access memory (SRAM) across its 128 neuromorphic cores and three x86 cores to manage the neuro cores and control spike traffic in and out of the chip. It supports asynchronous spiking neural network models for up to 130000 synthetic compartmental neurons and 130 million synapses. Loihi's architecture is designed to enable the mapping of deep convolutional networks optimised for vision and audio recognition tasks. Loihi was the first of its kind to feature on-chip learning via a microcode-based learning rule engine within each neural core, with fully programmable learning rules based on spike timing. Intel's chip allows the SNN to incorporate: 1) stochastic noise, 2) configurable and adaptable synaptic, axonal and refractory delays, 3) configurable dendritic tree processing, 4) neuron threshold adaptation to support intrinsic excitability homeostasis, and 5) scaling and saturation of synaptic weights to support "permanence" levels beyond the range of weights used during inference.[52, 53]

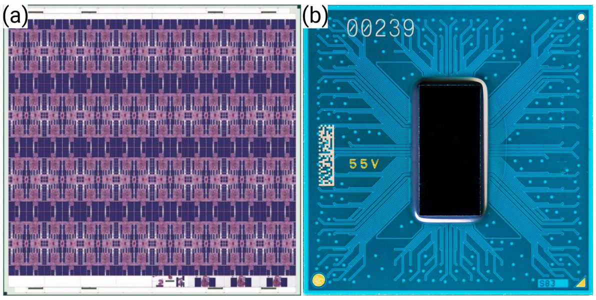

Figure 11. **a, b** – Loihi chip plot (a) and Intel's the second-generation neuromorphic research chip Loihi 2 (b) (pictures from the Intel's official website from the News about "Intel Advances Neuromorphic with Loihi 2, New Lava Software Framework and New Partners").

The on-chip learning is organised in such a way that the minimum of the loss function over a set of training samples is achieved during the training process. Also, learning rules satisfies the locality constraint: each weight can only be accessed and modified by the destination neuron, and the rule can only use locally available information, such as the spike trains from the pre-synaptic (source) and post-synaptic (destination) neurons. Loihi was the first fully integrated digital SNN chip that supported diverse local information for programmable synaptic learning process such as: 1) spike traces corresponding to filtered presynaptic and postsynaptic spike trains with configurable time constants, 2) multiple spike traces for a given spike train filtered with different time constants, 3) two additional state variables per synapse, besides the normal weight, to provide more flexibility for learning and 4) reward traces that correspond to special reward spikes carrying signed impulse values to represent reward or punishment signals for reinforcement learning.[52]

In Intel Labs original work the performance of Loihi was checked on theleast absolute shrinkage and selection operator (LASSO) task (l_1-minimising sparse coding problem). The goal of this task is to determine the sparse set of coefficients that best represents a given input signal as a linear combination of features from a feature dictionary.[52] This task was solved on a 52×52 image with a dictionary of 224 atoms and during that the Loihi allowed to provide 18 times compression of synaptic resources for this network. The sparse coding problem was solved to within 1% of the optimal solution. Unfortunately, the article does not provide data on energy efficiency and speed of the chip when solving this problem. A bit later in[53] the classical classification task on modified NIST dataset was solved with accuracy of 96.4%.

In 2021 Intel Labs introduced their second-generation neuromorphic research chip Loihi 2 (figure 11b), as well as the open-source software framework LAVA for developing neuro-inspired applications. Based on the Loihi experience, Loihi 2 supports new classes of neuro-inspired algorithms and applications, while providing up to 10 times faster processing, up to 15 times greater resource density with up to 1 million neurons per chip, and improved energy efficiency.[54] Loihi 2 has the same base architecture as its predecessor Loihi, but with new functionality and improvements. For example, the new chip supports fully programmable neuron models with graded spikes (Loihi supported only generalised LIF neuron model with binary spikes, whereas Loihi 2 supports any models) and achieves a 2× higher synaptic density. Ref. [55] reports a comparison of the performance and energy efficiency of the Loihi 2 chip compared to the performance of the the NVIDIA Jetson Orin Nano on video and audio processing task. Computing neuromorphic systems based on the Loihi 2 provide significant gains in energy efficiency, latency, and even throughput for intelligent signal processing applications (such as navigation and autopilot systems, voice recognition systems) compared to conventional architectures. For example, the Loihi 2 implementation of the Intel NSSDNet (Nonlocal Spectral Similarity-induced Decomposition Network) increases its power advantage to 74× compared to NsNet2 (Noise Suppression Net 2) running on the Jetson Orin Nano platform. The Loihi 2 has also demonstrated their advantages in Locally Competitive Algorithm implementation.[56] Loihi 2 is also capable of reproducing bio-realistic neural network implementation and it is flexible in terms of supporting different neuron models. Ref. [57] demonstrates a showcase of implementing a simplified bio-realistic basal ganglia neural network that carries “Go/No-Go” task, by using Izhikevich neurons.

3.3 Memristor-based realisations

A memristor is the fourth passive element of electrical circuits. This element is a two-terminal device, the main property of which is the ability to memorise its state depending on the applied bias current. Theoretically proposed[58] by Leon Chua in 1971, the memristor has seen the daylight as a prototype (memory + resistor) based on a thin film of titanium dioxide in 2008 thanks to HP Labs company.[59] The reason for the development of this device in the first place was the following problem: to further improve the efficiency of computing, electronic devices must be scalable to reduce manufacturing costs, increase speed and reduce power consumption – that is, more and more transistors must be placed on the same area of the crystal each time. However, due to physical limitations and rising manufacturing costs when moving to new process standards (to a 10 nm process, for example), the processing nodes of a traditional CMOS transistor can no longer scale cost-effectively and sustainably. As a result, new electronic devices with higher performance and energy efficiency have become necessary to satisfy the needs of the ever-growing information technology market,[60] implementing new “non-von Neumann” paradigms of in-memory computation.[61,62]

Initially, memristive systems acted as elements of energy-efficient resistive random-access memory memory (RRAM) by using two metastable states with high and low resistance, switching between which is carried out by applying an external voltage. However, in recent years, the potential application of memristors can be used to realise the functions of both synapses and neurons in both ANNs and SNNs.[63] Figure 12 shows one of the realisations of a memristor-based neuron. It exploits the diffusion processes between two types of layers: dielectric SiO_xN_y:Ag layer (doped with Ag nanoclusters) and Pt layer.[64] The SiO_xN_y:Ag material serves as the functional part of the memristor, allowing the creation of a model of the leaky integrate-and-fire neuron. The diffusive memristor integrates the presynaptic signals (arriving at one of the Pt electrodes) within a time window and transitions to a low resistance state only when a threshold is reached.

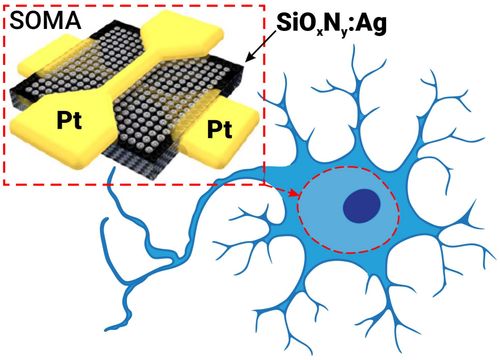

Figure 12. Illustration of the artificial neuron based on a diffusive memristor, consisting of a SiO_xN_y:Ag layer between two Pt electrodes.[64]

Using nanotechnology capabilities, it is possible to miniaturise memristive electronic devices to units of nanometers, which allows achieving a high density of elements on a chip. An important advantage of memristors is their compatibility with CMOS technology: memristors can be organised fairly easily into a crossbar architecture that takes advantage of parallel in-memory computing. With nanoscale, two-terminal and semiconductor memristor, memristor crossbars are characterised by high element density and better energy efficiency than their transistor counterparts. Due to this, this approach makes it possible to implement memristive networks based on 2D- and 3D-integrated crossbar structures to increase the speed of signal transmission.[65–70] This is why memristor crossbars are seen as a good candidate as a basis for neuromorphic networks.[71]

It is assumed that due to similar mechanisms of ion exchange in biological nerve cells and memristors, the last ones can mimic synapses and even neurons with sufficiently high accuracy. Since the capabilities of a neural network are usually determined by its size (number of neurons and inter-neuron connections), a scalable and energy-efficient component base is required to create a more powerful and energy-efficient system.[72,73] There have been many works aimed at studying the properties of memristors in terms of their application as synaptic elements and neurons, and there have even been successes in demonstrating the effect of synaptic plasticity[74] and the operation of the integrate-and-fire neural model.[75] Also an artificial neuron based on the threshold switching and fabricated on the basis of NbO_x material, has been demonstrated. Such a neuron displays four critical features: threshold-driven spiking, spatiotemporal integration, dynamic logic and gain modulation.[76]

The dynamic characteristics of memristors in combination with their nonlinear resistance allow us to observe the responses of the system to external stimulation.[77] At the same time, the stochastic properties of memristors due to interaction with the external environment[78] can be used both for controlling metastable states and for hardware design of SNN circuits.[79] The first experimental prototypes of SNNs based on memristors and CMOS have already been created (synapses are realised via memristor crossbars, and neurons - via semiconductor transistors) and they can "to a certain extent" emulate spike-timing dependent plasticity.[80,81] However, they are based on a simplified concept of synaptic plasticity based on overlapping pre- and postsynaptic adhesions,[81] which has led to reduced energy efficiency and rather complex technological design of SNN design circuits. Currently, approaches to overcome these problems are being developed, for example, on the basis of complete rejection of analogue-digital and digital-analogue transformations and creation of neuromorphic systems in which all signal processing occurs in analogue form[82] or by creating the concept of self-learning memristor SNNs.

Unfortunately, to realise a fully-memristive neuromorphic neural network it is necessary to achieve a non-linear dynamic signal processing. This challenge has so far not overcome by memristors alone, and every memristive neural network proposal relies on the operation of classical semiconductor transistors in one way or another. Below we consider two interesting realisations of CMOS memristive neural networks.

Neuromorphic network based on diffusive memristors

In 2018 Wang *et al.* presented an artificial neural network implemented on diffusive memristors (and also on transistors) that is capable to solve pattern classification task with unsupervised learning.[64] Note that the network demonstrated in the paper, recognised only four letters ("U", "M", "A", "S"), presented as 4-by-4 pixel images. Nevertheless, a working memristive network is a significant achievement and shows the feasibility in principle of the idea of memristor-based neuromorphic hardware computing. In figure 12 demonstrated the central part of this network and artificial neuron in particular – diffusive memristor consisted of a SiO_xN_y:Ag layer between two Pt electrodes and serving as the neuron's soma.

The most important difference between a diffusion memristor and a traditional memristor is that once the voltage is removed from the device terminals, it automatically returns to its original high-resistance state. The dynamics of the diffusion process in a diffusion memristor has similar physical behaviour to biological Ca^{2+} dynamics, which can accurately mimic different temporal synaptic and neuronal properties.[72]

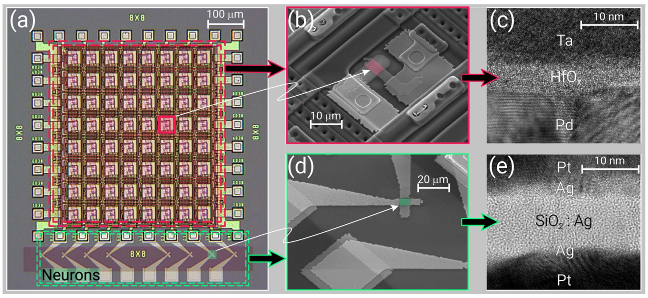

Figure 13. **a** – Microphotograph of the fully memristive spiking neural network, consisting of memristive synapse crossbar (in red frame) and memristive neurons (in blue frame). **b** – SEM (scanning electron microscopy) microphotograph of a single memristive synapse. **c** – TEM (transmission electron microscopy) image of the synapse cross-section with the structure of drift memristor, $Pd/HfO_x/Ta$. **d** – SEM microphotograph of a single memristive neuron. **e** – TEM image of the neuron cross-section with the structure of diffusive memristors, $Pt/Ag/SiO_x$: Ag/Ag/Pt. These images were adapted from Ref. [64].

The diffusive memristor in the artificial neuron is very different from non-volatile drift memristors or phase-change memory devices used as long-term resistive memory elements or synapses. The point is that the memristor processes the incoming signals within a certain time window (characteristic time, which in the diffusive memristor model is determined by the Ag diffusion dynamics to dissolve the nanoparticle bridge and return the neuron to its resting state) and then, only when a threshold has been reached, transitions to a low-resistance state. Figure 13a shows an integrated chip of the memristive neural network,[64] consisting of a one-transistor–one-memristor (figure 13b,c) synaptic 8-by-8 array and eight diffusive memristor neurons (figure 13d,e). The synapses were created by combining drift memristors with arrays of transistors. In this configuration, each memristor (*i.e.*, the $Pd/HfO_2/Ta$ structure) is connected to a series of n-type enhancement-mode transistors. When all the transistors are in an active state, the array functions as a fully connected memristor crossbar.

The input images are divided into four 2-by-2 pixel subsets, where each pixel is assigned a specific pair of voltages (equal in modulus but different in sign), depending on the colour and intensity of the pixel. Each resulting subset is expanded into a single-column input vector comprising eight voltages. This input vector is then applied to the network, which consists of eight rows, at each time step. For each possible subset, there is a corresponding convolution filter implemented using eight memristor synapses per column. In total, there are eight filters in an 8×8 array. The convolution of the eight filters for each sub-image simultaneously results in the "firing" of the corresponding neurons, which fulfil the role of ReLU. Eight outputs of these "ReLUs" coupled with the 8-by-3 fully connected memristive crossbar, whose fan-out concentrates all spikes on the last layer of the neural network consisting of 3 neurons "firing" which corresponds to a certain recognised image. It is claimed that the neuromorphic nature of the presented network is ensured due to the realisation of the effect of STDP used in the learning process and reflected in the change in the resistance of memristors in the crossbar when the next voltage pulse

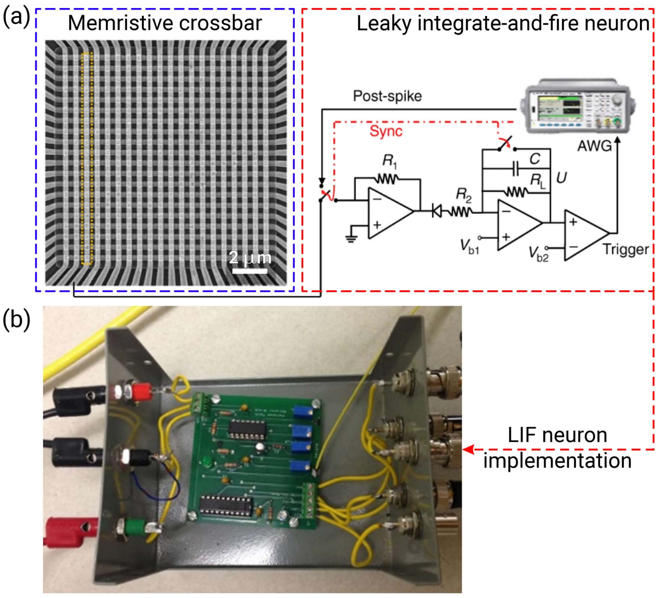

Figure 14. **a** – The SEM top view image of the 20 memristive crossbar-integrated synapses connected to a single leaky-integrate-and-fire neuron (schematics is shown). **b** – The experimental setup of the LIF neuron implementation.[80] These images were adapted from Ref. [80].

is passed. Despite the insufficient (in our opinion) representativeness of the learning results, the network architecture and the physics behind the used devices do not allow us to doubt the presence of the STDP effect, considering that similar effects were observed in memristors back in 2015.[83]

STDP learning in partially memristive SNN

The next realisation of the memristive-based neural network is proposed by Prezioso *et al.* [80], who experimentally demonstrated operation and STDP learning in SNN, implemented with the passively integrated (0T1R) memristive synapses connected to a silicon LIF neuron. The experimental setup consisted of 20 input neurons connected via 20 memristive crossbar-integrated synapses to a single LIF neuron. The input neurons – one neuron for each row of the memristive crossbar – are implemented using the off-the-shelf digital-to-analogue converter circuits. Synapses are implemented by $\mathrm{Pt/Al_2O_3/TiO_{2-x}/Pt}$ based memristors in a 20 × 20 crossbar array. In this SNN implementation there is only a single LIF output neuron that connected to the third array column, while the other columns are grounded. LIF neuron is also realised on the custom-printed circuit board (see figure 14). This arrangement allows connecting the crossbar lines either to the input/output neurons during network operation or to a switch matrix, which in turn is connected to the parameter analyser, for device forming, testing, and conductance tuning. Once the threshold is reached, the LIF neuron fires an arbitrary waveform generator. The characteristic duration of voltage spikes is on the order of 5 ms.

The neural network was trained to solve the coincidence detection problem (the task of identifying correlated spiking activity) using the STDP learning mechanism, which allows training a single neuron to produce an output pulse when it receives simultaneous (i.e., correlated) pulses from multiple input neurons. The relevance of such a task is due to the fact that the coincidence detection mechanism is an integral part of various parts of the nervous system, such as the auditory and visual cortex, and is generally believed to play a very important role in brain function.[84–86]

The conducted experiment has confirmed one of the main challenges for SNN implementation with memristors – their device-to-device variations. This imposes its own limitations on STDP learning, where it is important to consider certain time intervals (windows). Ideally, all synapses should be identical, and conductance updates for them should occur in equal STDP windows. In reality, however, conductance updates differ significantly between different memristive synapses, precisely because of differences in device switching thresholds. SNNs usually operate with spikes of the same magnitude, which allows to realise parallel updating of weights in several devices in crossbar circuit designs. In this experiment, the magnitude of the spikes was chosen based on the average switching threshold of the devices. Therefore, the change of conductivity in devices with a larger switching threshold was naturally smaller.

So, CMOS models provides great integration capabilities, while at the same time requiring high power supply and a large number of auxiliary elements to achieve bio-realism. Also for this technology it is still difficult to achieve high parallelism in the system due to significant interconnect losses. Meanwhile, important applications based on semiconductor neuromorphic chips are already being solved, and within the framework of the “Human Brain Project”, the second generation of the spiking neural network architecture SpiNNaker has even been created. Creating and advancing higher performance and energy efficient semiconductor chips is a very important issue. There are broad areas where these devices may be in high demand, primarily because of the possibility of mobile deployment from smart bioprostheses and brain-computer interfaces to “thinking” robot-androids.

Memristors can achieve bio-realism with fewer components (the ionic nature of their functioning is similar to that in neurons), but the technology of their manufacturing has not yet been refined and the problem of device-to-device variations has not been solved. Therefore, at the moment, we should assume that memristors will be an auxiliary tool for semiconductor technology. It is not realistic to create a fully memristive neuromorphic processor separately, but maybe it is not necessary?

At the device level, the energy required for computation and weight updates is minimal, as everything is rooted in the presence or absence of voltage spike. At the architecture level, computation is performed directly at the point of information storage (neuromorphism and rejection of von Neumann architecture), avoiding data movement as is the case in traditional digital computers. In addition, potentially memristor networks have the ability to directly process analogue information from various external sensors and sensing devices, which will further reduce processing time and power consumption. The superconductor element base used to build neuromorphic systems, discussed below, has the same capability. Experimental implementation of large memristor neural networks used for working with real data sets is at an early stage of development compared to CMOS analogues.[72] And the device-to-device variation in memristors' switching thresholds is still the major challenge.

4 Superconductor-based bio-inspired elements of neural networks

Superconducting digital circuits are also an attractive candidate for creating large-scale neuromorphic computing systems.[87–89] Their niche is in tasks that require both high performance and energy-efficient computing. Modern superconducting technologies make it possible to perform logical operations at high frequencies, up to 50 GHz, with energy consumption in the order of $10^{-19} - 10^{-20}$ J per operation.[87,90–94] Superconducting devices[95] lend themselves to the creation of highly distributed networks that offer greater parallelism than the conventional approaches mentioned above. For example, in a crossbar-based synaptic network, the resistive interconnection leads to performance degradation and self-heating. In contrast, the zero-dissipation superconducting interconnection at cryogenic temperatures provides a way to limit interconnection losses.

The main problem with superconductor-based technologies is their relatively low scalability. Recently, the size of superconducting logic elements, the main part of which is the Josephson junction (JJ),[96,97] is about $0.2\,\mu\text{m}^2$ (approximately 10^7 JJs per cm^2).[98–100] This value is comparable to the size of a transistor at 28 nm process technology in 2020. At the same time, superconducting hardware has a competitive advantage over CMOS technology due to its ability to exploit the third dimension in chip manufacturing processes. Incorporating vertically stacked Josephson inductors fabricated with self-shunted Josephson junctions in single-flux-quantum (SFQ) based circuits would increase circuit density with minimal impact on circuit margins.[101] In addition, the operating principles of Josephson digital circuits, which manipulate magnetic flux quanta with associated picosecond voltage pulses, are very close to the ideas of spiking neural networks.

Further development of the superconducting implementation of neuromorphic systems thus offers the prospect of creating a neuronet that emulates the functioning of the brain with ultra-high performance, and at the same time the neurons themselves prove to be relatively compact, since it is enough to use only a few heterostructures for the proper functioning of the cell.

The design of neurons and synapses using Josephson junctions and superconducting nanowires is discussed in the following subsections.

4.1 Implementations based on Josephson junctions

This approach is based on the quantisation of magnetic flux in superconducting circuits. Moreover, the flux quantum[102–104] can only enter and exit through a weak link in the superconductor: the Josephson junction, an analogue of an ion-permeable pore in the membrane of a biological neuron. This fact is important because studies of neural systems focus mainly on studying and reproducing the behaviour of neurons, including complex patterns of neuronal activity, their "firings". Just as biological neurons have a threshold voltage above which an action potential is generated, a Josephson junction has a threshold current, the Josephson junction critical current, I_c. When the current through the junction exceeds this value, a voltage spike-like pulse is generated.

One of the most common ways to describe Josephson junctions is the resistively shunted junction model, where the junction can be replaced with an equivalent circuit of three parallel elements: a Josephson junction, a resistor and a capacitor.[93] The current through the Josephson junction can be written as the sum of three currents:

$$I_S + I_N + I_D = I, \tag{6}$$

where I_S is the supercurrent governed by the Josephson phase φ of the JJ (the current phase relation is an important property of the heterostructure), I_N is the normal component of the current, for which Ohm's law can be applied, and I_D is the capacitive component of the current. Based on the Josephson relations for current components, we obtain a second-order differential equation describing the phase dynamics of the Josephson junction:

$$\frac{\hbar C}{2e}\ddot{\varphi} + \frac{\hbar}{2eR}\dot{\varphi} + I_c \sin\varphi = I, \tag{7}$$

where C and R are the capacitance and the normal-state resistance of the Josephson junction.

This equation is identical to that of a forced damped pendulum, where the first term gives the torque due to a "gravitational" potential, the second term is the damping term and the third term is the kinetic energy with a mass promotional to C. The sum of all three terms is the external torque corresponding to the applied current. When a small torque below the critical value is applied, the phase φ will increase and reach a static value. As the phase gets close to π, there will be a probability that the pendulum will go over the potential energy maximum, resulting in the emission of a SFQ-pulse. When the applied current exceeds the critical current, the torque is enough to continually drive the pendulum over the potential energy maximum generating a series of SFQ-pulses.

The Josephson junction soma (figure 15a), or JJ soma, proposed by Crotty *et al.* [105], is a circuit of two Josephson junctions connected in a loop which displays very similar dynamics to the HH model. The two junctions behave phenomenologically like the sodium and potassium channels, one allowing magnetic flux to charge up the loop and the other allowing flux to discharge from the loop. The circuit exhibits many features of biologically realistic neurons, including the evocation of action potentials "firing" in response to input stimuli, input strength

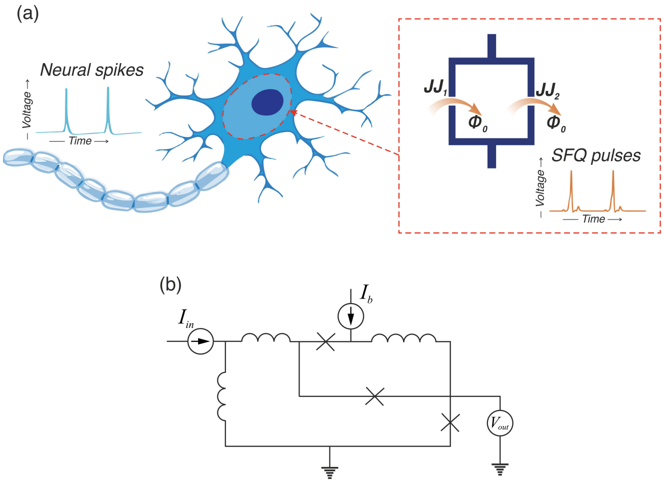

Figure 15. **a** – A sketch explaining the concept of the Josephson neuron: a superconducting circuit plays the role of a membrane impermeable to magnetic flux quanta; weak points of Josephson junctions allow quanta to enter (and exit) the circuit. **b** – By replacing one of the junctions with an asymmetric superconducting quantum interferometer device (SQUID) one enables control of the ratio between the "widths" of the input and output channels. The image in the panel b was adapted from Ref. [106].

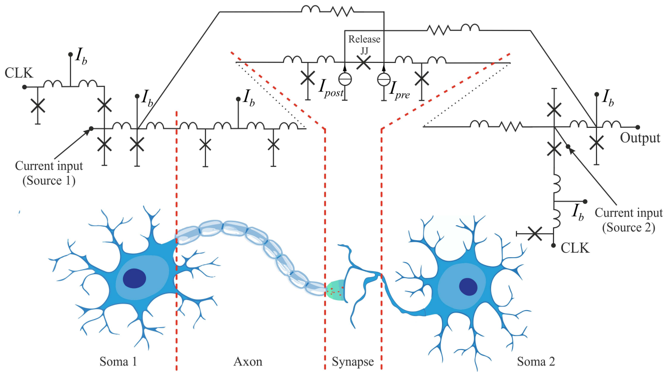

Figure 16. Schematic representation of the complete RSFQ-based architecture, along with a comparison of each of its components to the biological prototype. Here the JTLs act as axons, the Josephson junction in the centre as soma. This image was adapted from Ref. [109] and then recomposed by authors.

thresholds below which no action potential is evoked, and refractory periods after "firing" during which it is difficult to initiate another action potential.

Refs. [106–108] discuss an improved version of such a soma, where the input "pore" is represented as an asymmetric interferometer (figure 15b). The main advantage of the 3JJ neuron is that its mode of operation is easier to control. It has been shown that the 3JJ neuron has a much wider range of parameters in which switching between all operating modes (bursting, regular, dead, injury) is possible simply by controlling the bias current. Furthermore, the 3JJ neuron can be made controllable using identical Josephson junctions, and this design tolerates larger variations in the physical parameters of the circuit elements.

Each element of the nervous system can be represented by a similar behavior element of classical rapid-SFQ (RSFQ) logic. Complete architecture and comparison with the biological archetype are shown in figure 16. This circuit is driven by clocking regime in order to maintain stability when unforeseen side effects occur. One of the most compelling capabilities of superconducting electronics is its ability to support very high clock rates.

1. Soma – Josephson Comparator (JC)
   This is a clocked decision element that decides to let a single flux quantum pass in response to a current driven into source 1 in figure 16. The decision function of the comparator is similar to the activation of a neuron in response to a current stimulus. Note that the Josephson comparator has been widely used as a nonlinear element in superconducting spiking neural networks.[110, 111]

2. Axon – Josephson Transmission Line (JTL)
   The transmission of the action potential originating from the Soma to adjacent neurons can be carried out by the Josephson Transmission Line (JTL). A magnetic flux quantum can move along the JTL with a short delay and low energy dissipation, and its passage through the Josephson junction is accompanied by the appearance of a spike voltage pulse on the heterostructures. This mechanism can be likened to the process observed in biological systems, where the myelin sheath covering axons enables the action potential to "hop" from one point to the next.

3. Synapse – Adaptive Josephson Transmission Line (AJTL)
   Synapses exert an inhibitory or excitatory influence on the postsynaptic neuron with respect to the past activity of the pre- and post-synaptic neuron. While memory is still difficult to implement in RSFQ technology, Feldhoff *et al.*[109] have designed a short-term adaptation element that sets a connection weight depending on the steady state activity of the pre- and post-synaptic neuron. A common design element in RSFQ circuits is a release junction to prevent congestion. A release junction is inserted into a JTL, making it controllable by two currents. As a result, the release probability of an RSFQ from the JTL-based superconducting quantum interference device (SQUID) can be controlled by the current flowing through the junction. By driving the pulse sequence of the pre- and post-synaptic neuron through an L-R low-pass filter, the current through the JJ output is a function of the pulse frequency and thus of the activity level of both neurons. Thermal noise adds uncertainty to the junction switching and flux release from the superconducting loop. This creates a continuous dependence of the SFQ transmission probability on the junction current balance. Recently Feldhoff *et al.* [112] have presented an improved version of the synapse where the single junction is replaced by a two junction SQUID, called a release SQUID. This allows the critical current to be controlled by coupling an external magnetic field into the release circuit. Since the flux can be stored in another SQUID loop, the

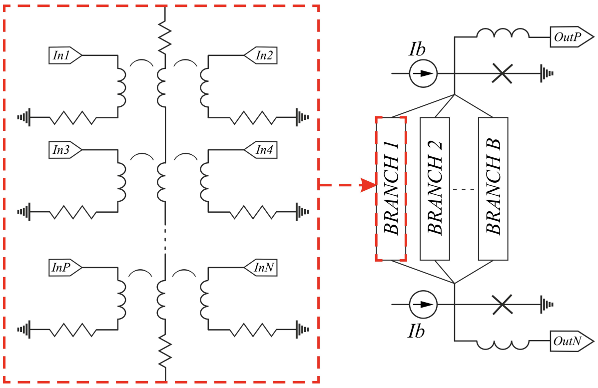

Figure 17. Schematics of an advanced neuron proposed by Karamuftuoglu *et al.* [114] (right) and its input data branch structure that enables the high-fan-in feature (left). This image was adapted from Ref. [114] and then redrawn by authors.

critical current can be permanently adjusted, which changes the transmission probability of SFQs passing through the synapse. This makes the synaptic connection more transparent to the connected neurons. The realization of tunable synaptic interconnections is also possible by utilizing adjustable kinetic inductance.[113]

To enable parallel processing in a network, it is necessary to have sufficient capabilities for both input (fan-in) and output (fan-out) in the technology platform. To address the issue of limited fan-in in JJ-based neuron designs, Karamuftuoglu *et al.* [114] introduced a high-fan-in superconducting neuron. The neuron design includes multiple branches representing dendrites, with each branch placed between two JJs that set the threshold of the neuron (see figure 17). This configuration allows for both positive and negative inductive coupling in each input data branch, supporting both excitatory and inhibitory synaptic data. The resistors on each branch create leaky behaviour in the neuron. A three hidden layer SNN using this neuron design achieved an accuracy of 97.07% on the modified NIST dataset. The network had a throughput of 8.92 GHz and consumed only 1.5 nJ per inference, including the energy required to cool the network to 4 K.[115]

Since memory storage is difficult to implement in RSFQ technology, magnetic Josephson junctions can be used to implement memory of past activity of pre- and post-synaptic neurons. In these devices, the wavefunction of Cooper pair extends into the ferromagnetic layer with a damped oscillatory behavior. Leveraging the physics of the interacting order parameters, Schneider et al. developed a new kind of synapse that utilizes a magnetic doped Josephson junction.[116] Inserting magnetic nanoparticles into the insulating barrier between two superconductors allows for the adjustment of the Josephson junction's critical current. Since numerous particles can be placed within the same barrier, each aligned in various directions, the critical current can effectively vary across a continuous range of values, making magnetic Josephson junctions an ideal memory element for the synaptic strength.

The memristive Josephson junctions (MRJJ) can also serve as a neuron-inspired device for neuromorphic computing. The paper by Wu *et al.*[117] investigates the dynamic properties of neuron-like spiking, excitability and bursting in the memristive Josephson junction and its improved version (the inductive memristive Josephson junction, L-MRJJ). Equivalent circuits of MRJJ and L-MRJJ are shown in figures 18a and 18b respectively. The MRJJ model is able to reproduce the spiking dynamics of the FitzHugh-Nagumo neuron (FHN model). Unlike the FHN model, the MRJJ model is bistable. The two class excitabilities (class I and class II) in the Morris-Lecar neuron are reproduced by the MRJJ model based on the frequency-current curve. The L-MRJJ oscillator exhibits bursting modes analogous to the neuronal busting of the 3-D Hindmarsh-Rose (HR) model in terms of purely dynamical behaviour, but there is a discrepancy between the two models. The generating origin of the bursting patterns depends on the saddle-node and homoclinic bifurcation using a fast-slow decomposition method. The L-MRJJ model has infinite equilibria. The coupled L-MRJJ oscillators can achieve both in-phase and antiphase burst synchronisation, similar to the behaviour of coupled Hindmarsh-Rose neurons. During burst synchronisation, the L-MRJJ network is partially synchronised, but the HR network is fully synchronised.

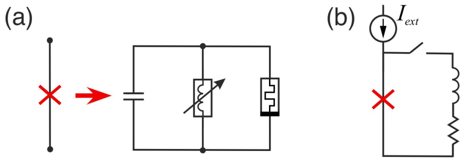

Figure 18. **a** – Equivalent circuit of a memristive Josephson junction (MRJJ) with, in order, capacitor, Josephson nonlinear device, memristor. **b** – A memristive Josephson junction connected in parallel with an inductor (schematic with internal resistor, L-MRJJ) is able to mimic neuron-like bursting behaviour. This image was adapted from Ref. [117] and then redrawn by authors.

Adjusting neuron threshold values in spiking neural networks is important for optimizing network performance and accuracy, as this adjustment allows for fine-tuning the network's behavior to specific input patterns. Ucpinar *et al.* [115] proposed a novel on-chip trainable neuron design, where the threshold values of the neurons can be adjusted individually for specific applications or during training.

4.2 BrainFreeze

Combining digital and analogue concepts in mixed-signal spiking neuromorphic architectures offers the advantages of both types of circuits while mitigating some of their disadvantages. Tschirhart *et al.* [118] proposed a novel mixed-signal neuromorphic design based on superconducting electronics (SCE) – BrainFreeze. This novel architecture integrates bio-inspired analogue neural circuits with established digital technology to enable scalability and programmability not achievable in other superconducting approaches.

The digital components in BrainFreeze support time-multiplexing, programmable synapse weights and programmable neuron connections, enhancing the effective-

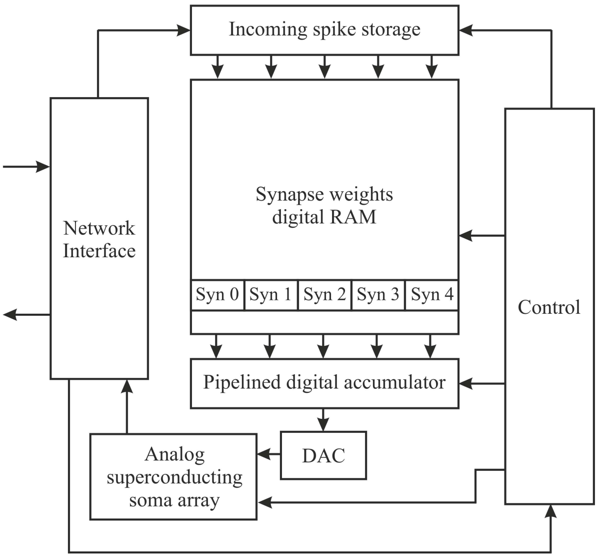

Figure 19. A high-level block diagram of the Neuron Core as part of the BrainFreeze concept. This image was adapted from Ref. [118] and then redrawn by authors.

ness of the hardware. The architecture's time-multiplexing capability enables multiple neurons within the simulated network to sequentially utilize some of the same physical components, such as the pipelined digital accumulator, thereby enhancing the hardware's effective density. Communication among neurons within BrainFreeze is facilitated through a digital network, akin to those employed in other large-scale neuromorphic frameworks. This digital network allows the sharing of wires connecting neuron cores across multiple simulated neurons, eliminating the necessity for dedicated physical wires to link each pair of neurons and significantly improves scalability. The flexible connectivity offered by the digital network also allows to implement various neural network structures by adjusting the routing tables within the network. By employing this approach, BrainFreeze leverages recent progress in SCE digital logic and insights gleaned from large-scale semiconductor neuromorphic architecture.

In its fundamental configuration, the BrainFreeze architecture consists of seven primary elements: control circuitry, a network interface, a spike buffer, a synapse weight memory, an accumulator, a digital-to-analogue converter, and at least one analogue soma circuit. A schematic representation illustrating the overall architecture is provided in figure 19. The authors refer to one instance of this architecture as a Neuron Core. This architectural framework merges the scalability and programmability features allowed by superconducting digital logic with the biological suggestivity functionalities enabled by superconducting analogue circuits.

Tschirhart *et al.* [118] provided a comparison of state-of-art neuromorphic architectures based on CMOS such as TrueNorth, SpiNNaker, BrainScale, Neurogrid and Loihi to BrainFreeze in order to demonstrate the potential of the proposed architecture (see figure 20). In conclusion, the findings indicate that employing a mixed-signal SCE neuromorphic approach has the potential to enhance performance in terms of speed, energy efficiency, and model intricacy compared to the current state of the art.

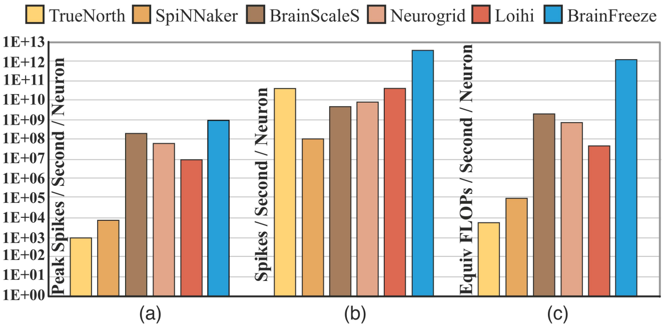

Figure 20. A comparison of state-of-art neuromorphic architectures with the BrainFreeze results. **a** – The first comparison examines spike emission speed. **b** – The second comparison examines the time and power efficiency of each architecture. **c** – The final comparison evaluates the computational complexity of the neuron models embedded in each architecture. In summary, BrainFreeze shows promising potential to achieve significant improvements over existing neuromorphic approaches. This image was adapted from Ref. [118] and then redrawn by authors.

4.3 Superconducting nanowire-based and phase-slip-based realisations

For a large neuromorphic network, the number of SFQ pulses generated should be high enough to drive a large fan-out. In this case, the JJ is limited in the number of SFQ pulses it can generate. Therefore, it may be very difficult to implement a complete neuromorphic network based solely on the JJ. Schneider *et al.* [119] have theoretically reported a fan-out of 1 to 10000 and a fan-in of 100 to 1. An approximate estimate of the power dissipated for a 1-to-128 flux-based fan-out circuit for a given critical current value is reported to be 44 aJ. Additionally, the action potentials in JJ are not sufficiently strong to be easily detectable. An alternative to JJ could be a thin superconducting wire, also known as a superconducting nanowire (SNW). The intrinsic non-linearity exhibited by superconducting nanowires positions them as promising candidates for the hardware generation of spiking behavior. When a bias current flowing through a superconducting nanowire exceeds a threshold known as the critical current, the superconductivity breaks down and the nanowire becomes resistive, generating a voltage. The nanowire switches back to the superconducting state only when the bias current is reduced below the retrapping current and the resistive part (the "hotspot") cools down. Placing the nanowire in parallel with a shunt resistor initiates electrothermal feedback, resulting in relaxation oscillations.[120] SNWs demonstrate reliable switching from superconducting to resistive states and have shown the capability to produce a higher number of SFQ pulses as output. Toomey *et al.* [121, 122] have proposed a nanowire-based neuron circuit that is topologically equivalent to the JJ-based bio-inspired neurons discussed above.

Quantum phase slip can be described as the exactly dual process to the Josephson effect based on charge-flux duality (figure 21). In a quantum phase-slip junction (QPSJ), a magnetic flux quantum tunnels across a superconducting nanowire along with Cooper pair transport and generate a corresponding voltage across the junction.[123, 124] Unlike Josephson junctions and superconducting nanowires, QPSJs do not require a constant current bias. However, the “flux-tunneling” together with voltage spike generation in such systems can be used to implement neuropodic systems on a par with Josephson junctions.

Cheng *et al.* [125] introduced a theoretical QPSJ-based spiking neuron design in 2018 (figure 22). When an input QPSJ fires, it charges a capacitor, building a potential that eventually exceeds the threshold of the output QPSJs connected in parallel. A resistor can be added to maintain the same bias across all QPSJs. This behaviour is consistent with the leaky integrate-and-fire neuron model. The total “firing” energy for this circuit design is given by the switching energy of the QPSJ multiplied by the number of QPSJs required for “firing”, and is estimated to be on the order of 10^{-21} J, compared to about 0.33 aJ (per switching event) for a typical JJ-based neuron.

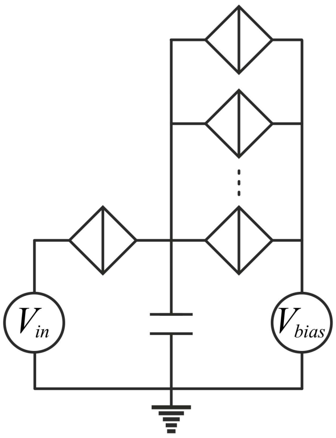

Figure 22. A QPSJ-based integrate and fire neuron circuit with integration capacitor and multiple parallel output QPS junctions. This image was adapted from Ref. [125] and then redrawn by authors.

5 Bio-inspired elements for optical neuromorphic systems

Another alternative neuromorphic solution is networks with physical realisation of spikes in the form of electromagnetic field packets. The advantage of such systems as candidates for hardware implementation of optical neural networks (ONN) is also their speed of information transmission, which can be carried out at frequencies exceeding 100 GHz (even at room temperature!),[126] as well as the ability to create distributed networks with a high degree of connectivity.[127] High bandwidth is important for practical applications such as those based on the control of hypersonic aircraft or related to the processing of radio signals. The first ONN solutions are based on silicon photonics, which is well compatible with CMOS technology, for example based on Mach-Zender interferometers[128] and micro-ring resonators.[129]

A common feature of optical computing systems is the ability to perform linear operations efficiently,[127, 130] whereas nonlinear signal transformations, including spike-based ones, pose a problem. As a result, these systems are poorly suited for implementing non-linear computations directly in the photonic domain. For this reason, hybrid solutions that combine the strengths of optical and electronic platforms are of interest. However, hybrid architectures consisting of photonic synapses and electronic spiking neurons require the use of high-speed photodetectors and analogue-to-digital converters to translate the results of optical linear computations back into the digital domain. This is complicated by high losses and packaging costs due to the need for strict alignment between lasers and waveguides.

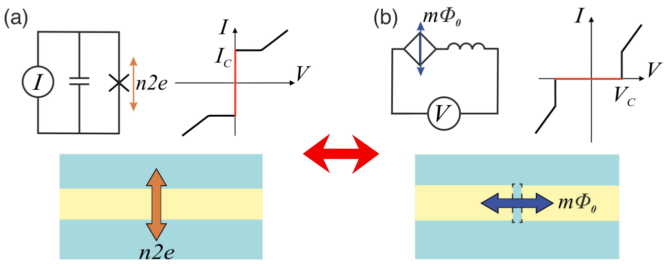

Figure 21. Illustration of the concept of charge-flux duality: **a** – sketch of a JJ, consisting of an insulating tunnel barrier (yellow) between a superconducting island (blue) and ”ground”; **b** – sketch of a QPSJ, consisting of a superconducting nanowire between an insulating island and ‘ground’. The inserts show the corresponding electrical circuits and current-voltage characteristics.

Recently, approaches have been developed to implement photonic spiking neurons and to create fully optical spiking neural networks (OSNN) using nonlinear optical elements. Several implementations of leaky integrate-and-fire neurons have been proposed based on vertical cavity surface emitting lasers (VCSELs),[131, 132] distributed feedback lasers (DFB),[133] phase change materials (PCM).[134] For example, VCSELs have a wide range of laser dynamics with distinct modes corresponding to orthogonal and parallel polarisation. The excitation of a sub-ns spike in this photonic neuron is based on the injection of an external signal and the conversion of electrical impulses into optical ones, showing all the typical signs of excitability of integrate-and-fire neuronal models. At the same time, typical microwave modulation frequencies of 30-50 GHz, combined with high efficiency, provide a sufficiently low power consumption for nonlinear conversion on the order of 10 fJ. By creating a photonic interconnect structure (bandwidth and latency), the entire structure can, after network training, perform calculations based on an optical signal at the speed of light without additional energy cost. This allows the dissipation in ONN using VCSEL to be decreased down to 100 aJ per operation. This looks promising from the point of view of energy efficiency.[135] However, it should be noted that most optical solutions require the use of coherent sources and detectors, as well as additional pre- and post-processing, which limits their scalability and compactness.

A detailed description of the operation of two common types of OSNN devices, based on phase change materials and semiconductor lasers, is given in the following subsections.

5.1 Phase change materials for elements in neural networks

Phase change materials (PCMs) are a special class of solid state materials that undergo a reversible phase transition from an amorphous to a crystalline state in response to external stimuli. Such perturbations can be both electrical and laser effects, which stimulate the release of heat in the device and, as a result, a change in temperature, causing significant changes in the optical and electrical properties of the materials.[136,137] One of the successful materials in photonic computing is the Ge-Sb-Te (GST) alloy, which recently demonstrated nanosecond recording speed using optical pulses.[138] This development has led to the creation of photonic memory devices,[139] switches[140] and non-volatile computers.[141] In addition, PCM has established itself as a platform for neuromorphic bio-inspired on-chip computing and has already demonstrated spike-timing dependent plasticity[130] and control of spiking neurons[142] in such systems.

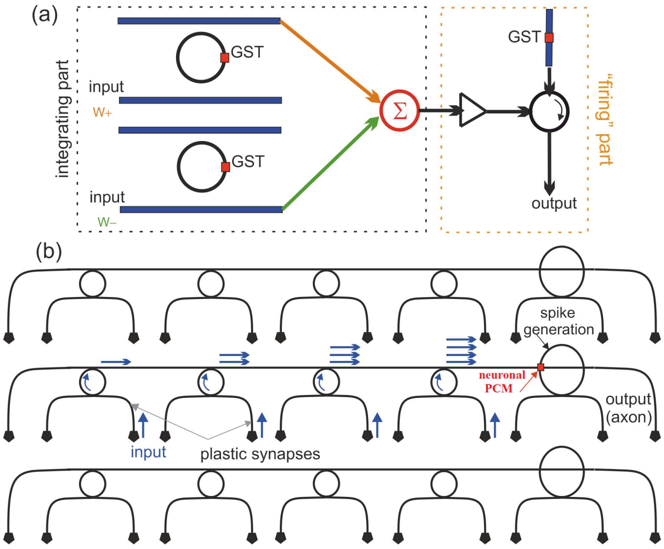

Figure 23. **a** – Schematic of a bipolar integrate-and-fire neuron based on GST ring resonator devices, where the right part in the black frame is responsible for integration part, and the right part in an orange dotted frame corresponds to the "firing" part. **b** – Schematic representation of three PCM neurons, each connected to four ring resonators (input) with different wavelengths (blue arrows). The total signal then enters the PCM cells (large rings on the right side of the figure), where the spike is generated. These images were adapted from Ref. [134] and then redrawn by authors.

Ref. [142] presented a bipolar integrate-and-fire spiking neuron, including an integration unit (black dotted block in figure 23a), consisting of two ring resonators with integrated PCM based on $Ge_2Sb_2Te_5$ and "firing" unit (orange dotted block in figure 23a). The dynamics of a spiking neuron is determined by a change in the GST phase state due to the absorption of light passing through the waveguide.

This process causes an increase in the temperature of the material and, consequently, an increase in the amorphisation of the material, that is, the GST state can be defined as a function of the thickness of the amorphous layer in the material from the amplitude of the input pulse. The use of two ring resonators allows the neuron to receive input signals of both polarities in order to process both positive and negative weight values of $w_\pm$ synapses, which is an important component in information processing. In this case, the resulting amplitude of the pulse arriving at the neuron, Σ, is equal to the difference between the values of the positive and negative inputs. Thus, the integration of the membrane potential is interconnected with the amplitude of the resulting pulse arriving at the neuron, which is represented by the integrating part of the circuit in figure 23a in a black dotted frame. As soon as GST reaches complete amorphisation, the membrane potential crosses its threshold. The "firing" action of the neuron is implemented by an additional photonic circuit (see the part highlighted by the orange dotted frame in figure 23a). This circuit consists of a photonic amplifier, a circulator and a rectangular waveguide with a GST element in a crystalline state with low pulse transmission. Based on the developed bipolar neuron circuit, the possibility of recording information at subnanosecond times is shown.[138,142] In addition, plasticity in weighing operations of synapses[130,143] were demonstrated on these PCM systems. The simplest prototype of an optical SNN was proposed, which demonstrated the scaling of individual synapses into a large-scale synaptic matrix capable of performing parallelised point computations through wavelength division multiplexing,[144] modulating the resonant wavelength by changing the size of the waveguides. This allowed higher recording densities to be achieved and circumvented some of the problems associated with designing ring resonators whose size is comparable to the operating wavelength range. Further, in the work,[145] a framework was proposed to demonstrate the operation of the proposed photonic SNN platform based on ring resonators with GST in solving image classification problems.

In 2019, the first experimental implementation of the integrated photonic SNN[134] was presented, consisting of three presynaptic neurons, one output (postsynaptic) neuron based on ring waveguides with GST and a six-network integrated all-optical synapses with integrated wavelength division multiplexing technology. An illustration of the experimental scheme of a neuromorphic PCM cell is shown in figure 23b. Ref. [134] has already tested the possibility of unsupervised network learning, for which a feedback waveguide was added to the circuit design, through which part of the output neuronal pulse propagates back through the synaptic elements in the PCM. This means that the connections with all the inputs that contributed to a particular jump in the output data are strengthened, and the connections that did not contribute to the jump are weakened. As a result, the optical SNN developed was able to detect the simplest patterns.

5.2 Spiking networks with semiconductor lasers

Semiconductor lasers are solid-state devices whose operation is based on the properties of a semiconductor ma-

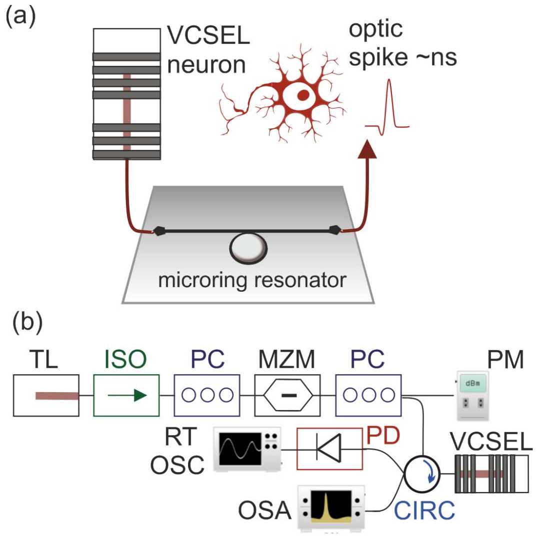

Figure 24. **a** – Schematic diagram showing the basic working principle of the experimentally investigated weighting of sub-ns optical spikes produced by a VCSEL-neuron. **b** – An experimental scheme of a photonic spiking neuron based on the use of the photodetector-resonant tunneling diode – VCSEL scheme, see more details in Ref. [153], where TL – tunable laser, ISO – optical isolator, PC – polarization controller, MZM – Mach-Zehnder modulator, PM – optical power meter, CIRC – optical circulator, OSA – optical spectrum analyzer, PD – photodetector, and RT OSC – real-time oscilloscope. These images were adapted from Ref. [152] and then redrawn by authors.

terial. The power, directivity and compactness of solid-state lasers make them indispensable for high-intensity tasks, while the adaptability and efficiency of semiconductor lasers lend themselves to applications requiring precision and stability. Fairly recently, another promising application of semiconductor lasers has appeared – neuromorphic computing. It has already been possible to observe the manifestation of bio-inspired properties of such systems, such as excitability[146, 147] and demonstration of nonlinear dynamics,[148, 149] which became promising first steps towards the implementation and study of optical spiking neurons based on semiconductor lasers.

Vertical-Cavity Surface-Emitting Lasers (VCSEL)[131, 132] and Distributed Feedback Semiconductor Lasers (DFB-SL)[133] are currently the main types of devices for creating and studying optical spiking neurons. The photonic elements under consideration consist of three parts: a photodetector acting as an optical-electrical converter, a receiver – a pulse converter of the micrometer range that generates pulses in response to incoming disturbances at the input, and VCSEL with a wavelength of 1550 nm, acting as a converter of an electrical signal into an optical one. A typical scheme for implementing spiking neuron based on VCSEL is shown in figure 24a. Obtaining controlled optical spikes when exposed to exciting signals is based on the effects of polarisation switching, as well as synchronisation of phase and amplitude modulated injection locking.[150]

Another way of implementing the spiking optical neuron[151] in laser systems is to use a resonant tunneling diode: a semiconductor heterostructure with a double-barrier quantum well.[152] Due to the N-shaped I-V characteristic of the diode and the effect of resonant quantum tunneling, such devices have rich nonlinear dynamics. The amplitude of optical pulses in synaptic connections can be controlled by adjusting the VCSEL bias current. An artificial optoelectronic neuron based on an InGaAs resonant-tunneling diode connected to a VCSEL has been proposed and experimentally implemented[153] (see figure 24b), which allows the presynaptic weight of the emitted optical pulses to be fully tuned at high speed. The operation of the optical neuron is based on coherent injection locking of the VCSEL with a signal from an external tunable laser source (TL). The TL signal is passed through an optical isolator (ISO) to provide unidirectional communication between the lasers, and the TL light intensity is modulated using a Mach–Zehnder modulator (MZM). The polarization of the modulated signal is consistent with the orthogonally polarized VCSEL mode before it is fed into the device through an optical circulator (CIRC). Another branch of this connector is used to register power of the VCSEL-neuron using the photodetector (PD) and the real-time oscilloscope (RT OSC) from the power meter (PM). The wavelength TL corresponds to a peak in the laser spectrum. Switching between the states (threshold and steady) is carried out by adjusting the input power. The information is encoded in the signal intensity in such a way that the “stronger” stimuli correspond to a greater decrease in injection power.

The threshold characteristics and refractory period of neurons based on VCSELs[154–157] have already been studied. These properties naturally determine the maximum pulse response frequency and are key properties for spike processing using rate coding, photonic polarisation dynamics and excitability of neurons,[158] as well as controlled distribution spike pulses.[159, 160] Furthermore, the simplest integrated photonic accelerator processor based on VCSELs has been experimentally proposed and the simplest implementation of the XOR[133] classification problem has been demonstrated. It is shown that the spike laser neuron performs coincidence detection with nanosecond time resolution with a refractive period of about 0.1 ns. In addition,[161] proposed a physical model for pattern recognition based on photonic STDP, which is also based on VCSELs. However, the neurons on VCSELs require a continuous power supply to maintain the behaviour of the neurons, so the advantages of energy efficiency in such systems are negated. With regard to DFB lasers, schemes have also been proposed for the implementation of passive micro-ring optical spiking neurons,[162] where neuromorphic information processing is performed, including image recognition based on STDP. Note that an important difference from VCSEL in implementing STDR on DFB-SL is the absence of wavelength conversion and the use of optical filters.[161, 163]

It should be noted that spiking of optical neurons on other types of semiconductor lasers is currently being proposed. For example, ring lasers have achieved multiple spikes with a single perturbation,[164] excitation responses based on semiconductor lasers on quantum dots[165, 166] have been successfully modelled, threshold properties of optically injected microdisk lasers[167] have been studied, and an integrated graphene-excited laser has been shown to exhibit dynamics on the order of picosecond timescales.[168] However, these types of lasers are in the early stages of research for SNN compared to VCSEL and DFB-SL.

6 Discussion and conclusion

The opportunities for neuromorphic computing technology are immense, ranging from classical tasks such as pattern recognition and video stream analysis to central nervous system modelling and brain-computer interfaces. Challenges for the SNN include: neuromorphic locomotion control, neurorobotics, gait control, environmental perception, adaptation; computational modelling of the brain in the study of biological nervous systems (Human Brain Project); dynamic recognition; prosthetics (visual and auditory implants, treatment of Parkinson's, dystonia, schizophrenia, etc.), etc.

For the time being, not many laboratories in the world are involved in these projects and tasks, as the main focus is now on the development of narrowly focused software models that solve a strictly defined problem. There is not yet a demand from large international companies or large private consumer sectors for the creation of versatile neural network models, but this moment is approaching: the problem of designing and training deep neural networks of large dimensionality is becoming more and more obvious. Nowadays, almost all neural network models are implemented in one way or another on the basis of NVIDIA's video chips, the annual production of which is very limited, and there are even certain quotas for bulk purchases. The energy required to train such networks is also a significant problem. At the same time, there is no guarantee that the neural network model is designed correctly and that the training is carried out as required: it may turn out that the accuracy of the neural network is not high enough, or there may be an overtraining effect.

The advantages of the semiconductor element base for hardware implementation of bio-inspired neural networks are significant developments in the field of information input/output devices, digital-to-analogue and analogue-to-digital converters. Unfortunately, one of the main problems when trying to implement hardware parallelism of large networks is the implementation of synaptic connections. In two-dimensional parallel hardware, physical wiring only allows connections between adjacent neurons, whereas biological neurons are distributed in three-dimensional space and have many (thousands) connections between populations.

Memristive technologies can be instrumental in the creation of large-scale networks with a large number of synaptic connections.[169] The memristive crossbars, which are used as a kind of synaptic grid with both STDP and STDD (Spike Timing Dependent Depression). The neurons themselves are mostly implemented using transistors. Attempts are being made to create a fully memristive neural network, but it is still not possible to realise without more conventional semiconductor devices.

The field of superconductivity has its own distinct successes (high performance and energy efficiency) and problems (low integration density). Special attention should be paid to hybrid interdisciplinary approaches:[170–173] for signal transmission, for light pulses transmitted from neuron to neuron via optical waveguides on a chip, for information processing and storage, and for superconducting circuits, including single-photon detectors and superconducting digital logic cells. Superconducting technologies make it possible to reduce the energy stored in pulses by the electromagnetic field so that a signal containing only a few photons can be used. To increase the compactness and efficiency of the interaction with electromagnetic radiation, current concentrating heterostructures (variable thickness bridges or Dayem bridges) and multilayer thin film heterostructures can be used instead of traditional superconductor-insulator-superconductor Josephson junctions. Finally, superconducting implementations are interesting because they allow close integration with superconducting quantum bits.[174] This offers the hope of being able to experimentally test hypotheses about the role of quantum effects in the functioning of consciousness.

In the pursuit of bio-inspiration, performance, energy efficiency, scalability and compactness, one should not fall into the extremes of the capabilities of a single element base – it is likely that some elements of a neural network are much more convenient and efficient to implement in a different way. In this review, we have tried to show not only that the field of spiking neural networks with bio-inspired properties is actively developing, but that it is developing in different directions, like an octopus with its tentacles finding the right solution, the direction of development. In our view, all the areas discussed in this article have their own strengths and weaknesses. At the moment, however, it is difficult to say which of them will "take off". This is why hybrid approaches are so popular at the moment, taking the advantages of their components and compensating for their mutual disadvantages. In addition to hardware implementations and software SNNs, biological neural networks based on biological organoids and reservoir computing[175–177] are on the way to creating a biocomputer,[178] but we have left this area outside the scope of this review.

7 Acknowledgments

The concept of developing spiking neural networks was carried out with the support of the Grant of the Russian Science Foundation No. 22-72-10075. We are grateful to the the Foundation for the Advancement of Theoretical Physics and Mathematics "BASIS" (A.S. grant 22-1-3-16-1; M.B. grant 22-1-3-41-1; A.M. grant 23-2-1-16-1). A.S. contributed to the Introduction, the second section "CMOS-based bio-inspired neuromorphic circuits", Discussion and general edition. M.B. contributed to the second section on memristive systems, as well as on optical neuromorphic systems. A.M. contributed to the fourth section "Superconductor-based bio-inspired elements of neural networks". The analysis of the possibilities of hybrid approaches was supported by the Ministry of Science and Higher Education of the Russian Federation (Agreement No. 075-15-2024-632).

Contact information

Corresponding author: Nikolay V. Klenov, orcid.org/ 0000-0001-6265-3670, e-mail nvklenov@mail.ru.

Competing Interests

The authors declare no competing financial or non-financial interests.

References

[1] Abramson J., Adler J., Dunger J., Evans R. *et al. Accurate structure prediction of biomolecular interactions with AlphaFold 3.* Nature, vol. **630**, 493–500 (2024).

[2] Abramson J., Adler J., Dunger J., Evans R. *et al. Neural networks and physical systems with emergent collective computational abilities.* Proc. Natl. Acad. Sci. U.S.A., vol. **79**, 2554-2558 (1982).

[3] Prieto A., Prieto B., Ortigosa E. M, Ros E., and Pelayo F., Ortega J., Rojas I. *Neural networks: An overview of early research, current frameworks and new challenges.* Neurocomputing, vol. **214**, 242-268 (2016).

[4] Taherkhani A., Belatreche A., Li Y., Cosma G., Maguire L. P., McGinnity T. M. *A review of learning in biologically plausible spiking neural networks.* Neural Netw., vol. **122**, 253-272 (2020).

[5] Markram H. *The blue brain project.* Nat. Rev. Neurosci., vol. **7**, 153-160 (2006).

[6] Van Der Smagt P., Arbib M. A., Metta G. *Neurorobotics: From Vision to Action. In: Siciliano B., Khatib O. (eds) Springer Handbook of Robotics.* Springer Handbooks. p. 2069–2094 (2006).

[7] Iosa M., Morone G., Cherubini A., Paolucci S. *The three laws of neurorobotics: a review on what neurorehabilitation robots should do for patients and clinicians.* J. Med. Biol. Eng., vol. **36**, 1-11 (2006).

[8] Falotico E., Vannucci L., Ambrosano A., Albanese U. *et al. Connecting artificial brains to robots in a comprehensive simulation framework: the neurorobotics platform.* Front. Neurorobot., vol. **11**, 2 (2017).

[9] Raspopovic S. *Neurorobotics for neurorehabilitation.* Science, vol. **373**, 634-635 (2021).

[10] Kasabov N. K. *NeuCube: A spiking neural network architecture for mapping, learning and understanding of spatio-temporal brain data.* Neural Netw., vol. **52**, 62-76 (2014).

[11] Yamazaki K., Vo-Ho V.-K., Bulsara D., Le N. *Spiking neural networks and their applications: A Review.* Brain Sci., vol. **12**, 863 (2022).

[12] Liang Q., Zeng Y., Xu B. *Temporal-sequential learning with a brain-inspired spiking neural network and its application to musical memory.* Front. Comput. Neurosci., vol. **14**, 51 (2020).

[13] He B., Yuan H., Meng J., Gao S. *Brain-computer interfaces. In: He B. (eds) Neural Engineering* Springer, p. 131-183 (2020).

[14] Gao X., Wang Y., Chen X., Gao S. *Interface, interaction, and intelligence in generalized brain-computer interfaces.* Trends Cogn. Sci., vol. **25**, 671-684 (2021).

[15] Yadav D., Yadav S., Veer K. *A comprehensive assessment of Brain Computer Interfaces: Recent trends and challenges.* J. Neuroscie. Met., vol. **346**, 108918 (2020).

[16] Flesher S. N., Downey J. E., Weiss J. M., Hughes C. L., Herrera A. J., Tyler-Kabara E. C., Boninger M. L., Collinger J. L., Gaunt R. A. *A brain-computer interface that evokes tactile sensations improves robotic arm control.* Science, vol. **372**, 831-836 (2021).

[17] Bonci A., Fiori S., Higashi H., Tanaka T., Verdini F. *An introductory tutorial on brain-computer interfaces and their applications.* Electronics, vol. **10**, 560 (2021).

[18] Hodgkin A. L., Huxley A. F. *A quantitative description of membrane current and its application to conduction and excitation in nerve.* J. Physiol., vol. **117**, 500 (1952).

[19] Malcom K., Casco-Rodriguez J. *A comprehensive review of spiking neural networks: Interpretation, optimization, efficiency, and best practices.* arXiv preprint arXiv:2303.10780.

[20] Häusser M. *The Hodgkin-Huxley theory of the action potential.* Nat. Neurosci., vol. **3**, 1165 (2000).

[21] Zheng N., Mazumder P. *Operational Principles and Learning in Spiking Neural Networks*, chapter in: *Learning in Energy-Efficient Neuromorphic Computing: Algorithm and Architecture Co-Design.* Wiley-IEEE Press, 2020.

[22] Thanapitak S. *Bionics Chemical Synapse.* PhD thesis, Imperial College London, UK, (2012).

[23] Izhikevich E. M. *Simple Model of Spiking Neurons.* IEEE Trans. Neural Netw. Learn. Syst., vol. **14**, 1569-1572 (2003).

[24] Izhikevich E. *Dynamical Systems in Neuroscience: The Geometry of Excitability and Bursting.* Comput. Neurosci. Series, The MIT Press (2006).

[25] Izhikevich E. *Neural excitability, spiking, and bursting.* Int. J. Bifurc. Chaos, vol. **10**, 1171-1266 (2000).

[26] Wu Y., Deng L., Li G., Zhu J., Shi L. *Spatio-temporal backpropagation for training high-performance spiking neural networks.* Front. Neurosci., vol. **12**, 331 (2018).

[27] Eshraghian J. K., Ward M., Neftci E. O., Wang X., Lenz G., Dwivedi G., Bennamoun M., Jeong D. S., Lu W. D. *Training spiking neural networks using lessons from deep learning.* Proc. IEEE, vol. **111**, 1016 - 1054 (2023).

[28] Pérez-Carrasco J. A., Zhao B., Serrano C., Acha B., Serrano-Gotarredona T., Chen S., Linares-Barranco B. *Mapping from frame-driven to frame-free event-driven vision systems by low-rate rate coding and coincidence processing-application to feedforward ConvNets.* IEEE Trans. Pattern Anal. Mach. Intell., vol. **35**, 2706-2719 (2013).

[29] Yin B., Corradi F., Bohté S. M. *Accurate online training of dynamical spiking neural networks through Forward Propagation Through Time.* Nat. Mach. Intell., vol. **5**, 518-527 (2023).

[30] Irie K., Gopalakrishnan A., Schmidhuber J. *Exploring the promise and limits of real-time recurrent learning.* arXiv preprint arXiv:2305.19044 (2023).

[31] Reljan-Delaney M., Wall J. *Solving the linearly inseparable XOR problem with spiking neural networks.* 2017 Computing Conference, London, UK, pp. 701-705 (2017).

[32] Indiveri G., Linares-Barranco B., Hamilton T. J., Schaik A. *et al. Neuromorphic silicon neuron circuits.* Front. Neurosci., vol. **5**, 73 (2011).

[33] Merolla P. A., Arthur J. V., Alvarez-Icaza R., Cassidy A. *et al. A million spiking-neuron integrated circuit with a scalable communication network and interface.* Science, vol. **345**, 668-673 (2014).

[34] Akopyan F., Sawada J., Cassidy A., Alvarez-Icaza R., *et al. Truenorth: Design and tool flow of a 65 mW 1 million neuron programmable neurosynaptic chip.* IEEE Trans. Comput.-Aided Des. Integr. Circuits Syst., vol. **34**, 1537-1557 (2015).

[35] Benjamin B. V., Gao P., McQuinn E., Choudhary S., Chandrasekaran A. R., Bussat J.-M., Alvarez-Icaza R., Arthur J. V., Merolla P. A., Boahen K. *Neurogrid: A mixed-analog-digital multichip system for large-scale neural simulations.* IEEE Trans. Comput.-Aided Des. Integr. Circuits Syst., vol. **102**, 699-716 (2014).

[36] Camuñas-Mesa L. A., Linares-Barranco B., Serrano-Gotarredona T. *Neuromorphic spiking neural networks and their memristor-CMOS hardware implementations.* Materials, vol. **12**, 2745 (2019).

[37] Hynna K. M., Boahen K. *Thermodynamically equivalent silicon models of voltage-dependent ion channels.* Neural Comput., vol. **19**, 327-350 (2007).

[38] Park Y.-S., Woo S., Lim D., Cho K., Kim S. *Integrate-and-fire neuron circuit without external bias voltages.* Front. Neurosci., vol. **15**, 644604 (2021).

[39] Wijekoon J. H. B., Dudek P. *Compact silicon neuron circuit with spiking and bursting behaviour.* Neural Netw., vol. **21**, 524-534 (2008).

[40] Furber S. B, Lester D. R., Plana L. A., Garside J. D., Painkras E., Temple S., Brown A. D. *Overview of the SpiNNaker system architecture.* IEEE Trans. Comp., vol. **62**, 2454-2467 (2012).

[41] Sawada J., Akopyan F., Cassidy A. S., Taba B. *et al. Truenorth ecosystem for brain-inspired computing: scalable systems, software, and applications.* SC '16: Proceedings of the International Conference for High Performance Computing, Networking, Storage and Analysis, Salt Lake City, USA, pp. 130-141 (2016).

[42] Stromatias E., Neil D., Galluppi F., Pfeiffer M., Liu S.-C., Furber S. *Scalable energy-efficient, low-latency implementations of trained spiking deep belief networks on spinnaker.* 2015 International Joint Conference on Neural Networks (IJCNN), Killarney, Ireland, pp. 1-8 (2015).

[43] *GPU-Based Deep Learning Inference: A Performance and Power Analysis.* NVidia Whitepaper (2015).

[44] Mayr C., Hoeppner S., Furber S. *SpiNNaker 2: A 10 Million Core Processor System for Brain Simulation and Machine Learning.* arXiv preprint arXiv:1911.02385 (2019).

[45] Painkras E., Plana L. A., Garside J., Temple S., Galluppi F., Patterson C., Lester D. R., Brown A. D., Furber S. B. *SpiNNaker: A 1-W 18-core system-on-chip for massively-parallel neural network simulation.* IEEE J. Solid-State Circuits, vol. **48**, 1943-1953 (2013).

[46] Stromatias E., Galluppi F., Patterson C., Furber S. *Power analysis of large-scale, real-time neural networks on SpiNNaker.* 2013 International Joint Conference on Neural Networks (IJCNN), Dallas, TX, USA, pp. 1-8 (2013).

[47] Höppner S., Yan Y., Dixius A., Scholze S. *et al. The SpiNNaker 2 processing element architecture for hybrid digital neuromorphic computing.* arXiv preprint arXiv:2103.08392 (2021).

[48] Merolla P., Arthur J., Alvarez R., Bussat J.-M., Boahen K. *A Multicast Tree Router for Multichip Neuromorphic Systems.* IEEE Trans. Circuits Syst. I: Regul. Pap., vol. **61**, 820-833 (2014).

[49] Benjamin B. V., Steinmetz N. A., Oza N. N., Aguayo J. J., Boahen K. *Neurogrid simulates cortical cell-types, active dendrites, and top-down attention.* Neuromorph. Comput. Eng., vol. **1**, 013001 (2021).

[50] Knight J. C., Nowotny T. *Larger GPU-accelerated brain simulations with procedural connectivity.* Nat. Comput. Sci., vol. **1**, 136-142 (2021).

[51] Modha D. S., Akopyan F., Andreopoulos A., Appuswamy R. *et al. Neural inference at the frontier of energy, space, and time.* Science, vol. **382**, 329-335 (2023).

[52] Davies M., Srinivasa N., Lin T.-H., Chinya G. *et al. Loihi: A neuromorphic manycore processor with on-chip learning.* IEEE Micro, vol. **38**, 82-99 (2018).

[53] Lin C.-K., Wild A., Chinya G. N., Cao Y., Davies M., Lavery D. M., Wang H. *Programming spiking neural networks on Intel's Loihi.* Computer, vol. **51**, 52-61 (2018).

[54] *Taking neuromorphic computing to the next level with Loihi2.* Intel Labs' Loihi (2021).

[55] Shrestha S. B., Timcheck J., Frady P., Campos-Macias L., Davies M. *Efficient video and audio processing with Loihi 2.* ICASSP 2024-2024 IEEE International Conference on Acoustics, Speech and Signal Processing, Seoul, Korea, p. 13481-13485 (2024).

[56] Parpart G., Risbud S., Kenyon G., Watkins Y. *Implementing and Benchmarking the Locally Competitive Algorithm on the Loihi 2 Neuromorphic Processor.* Proceedings of the 2023 International Conference on Neuromorphic Systems, Santa Fe, USA, p. 1-6 (2023).

[57] Uludağ R. B., Çağdaş S., İşler Y. S., Şengör N. S., Akturk I. *Bio-realistic Neural Network Implementation on Loihi 2 with Izhikevich Neurons.* Neuromorph. Comput. Eng., vol. **4**, 024013 (2024).

[58] Chua L. *Memristor – The missing circuit element.* IEEE Trans. Circuit Theory, vol. **18**, 507-519 (1971).

[59] Strukov D. B., Snider G. S., Stewart D. R., Williams, R. S. *The missing memristor found.* Nature, vol. **453**, 80-83 (2008).

[60] Li Y., Wang Z., Midya R., Xia Q., Yang J. J. *Review of memristor devices in neuromorphic computing: materials sciences and device challenges.* J. Phys. D: Appl. Phys., vol. **51**, 503002 (2018).

[61] Li Y., Wang Z., Midya R., Xia Q., Yang J. J. *Memristive Devices for Neuromorphic Applications: Comparative Analysis.* BioNanoSci., vol. **10**, 834-847 (2020).

[62] Lee S. H., Zhu X., Lu W. D. *Nanoscale resistive switching devices for memory and computing applications.* Nano Res., vol. **13**, 834-847 (2020).

[63] Mikhaylov A. N., Gryaznov E. G., Koryazhkina M. N., Bordanov I. A., Shchanikov S. A., Telminov O. A., Kazantsev V. B. *Neuromorphic Computing Based on CMOS-Integrated Memristive Arrays: Current State and Perspectives.* Supercomp. Front. Innovations, vol. **13**, 77–103 (2023).

[64] Wang Z., Joshi S., Savel'ev S., Song W. *et al. Fully memristive neural networks for pattern classification with unsupervised learning.* Nat. Electron., vol. **1**, 137-145 (2018).

[65] Strukov D. B., Williams R. S. *Four-dimensional address topology for circuits with stacked multilayer crossbar arrays.* Proc. Natl. Acad. Sci. U.S.A., vol. **106**, 20155-20158 (2009).

[66] Jo S. H., Chang T., Ebong I., Bhadviya B. B., Mazumder P., Lu W. *Nanoscale Memristor Device as Synapse in Neuromorphic Systems.* Nano Lett., vol. **10**, 1297-1301 (2010).

[67] Likharev K. K. *CrossNets: Neuromorphic hybrid CMOS/nanoelectronic networks.* Sci. Adv. Mater., vol. **3**, 322-331 (2011).

[68] Prezioso M., Merrikh-Bayat F., Hoskins B. D., Adam G. C., Likharev K. K., Strukov D. B. *Training and operation of an integrated neuromorphic network based on metal-oxide memristors.* Nature, vol. **521**, 61-64 (2015).

[69] Prezioso M., Merrikh Bayat F., Hoskins B., Likharev K., Strukov D. *Self-adaptive spike-time-dependent plasticity of metal-oxide memristors.* Sci. Rep., vol. **6**, 21331 (2016).

[70] Papandroulidakis G., Vourkas I., Abusleme A., Sirakoulis G. Ch., Rubio A. *Crossbar-Based Memristive Logic-in-Memory Architecture.* IEEE Trans. Nanotechnol., vol. **16**, 491-501 (2017).

[71] Zhang X., Huang A., Hu Q., Xiao Z., Chu P. K. *Neuromorphic computing with memristor crossbar.* Phys. Status Solidi A, vol. **215**, 1700875 (2018).

[72] Xia Q., Yang J. J. *Memristive crossbar arrays for brain-inspired computing.* Nat. Mater., vol. **18**, 309–323 (2019).

[73] Tzouvadaki I., Gkoupidenis P., Vassanelli S., Wang S., Prodromakis T. *Interfacing Biology and Electronics with Memristive Materials.* Adv. Mater., vol. **35**, 2210035 (2023).

[74] La Barbera S., Vuillaume D., Alibart F. *Filamentary switching: synaptic plasticity through device volatility.* ACS Nano, vol. **9**, 941-949 (2015).

[75] Zhang X., Wang W., Liu Q., Zhao X *et al. An artificial neuron based on a threshold switching memristor.* IEEE Electron Device Lett., vol. **39**, 308-311 (2017).

[76] Duan Q., Jing Z., Zou X., Wang Y., Yang K., Zhang T., Wu S., Huang R., Yang Y. *Spiking neurons with spatiotemporal dynamics and gain modulation for monolithically integrated memristive neural networks.* Nat. Commun., vol. **11**, 3399 (2020).

[77] Pershin Y. V., Slipko V. A. *Dynamical attractors of memristors and their networks.* Europhys. Lett., vol. **125**, 20002 (2019).

[78] Carboni R., Ielmini D. *Stochastic memory devices for security and computing.* Adv. Electron. Mater., vol. **5**, 1-27 (2019).

[79] Makarov V. A., Lobov S. A., Shchanikov S., Mikhaylov A., Kazantsev V. B. *Toward Reflective Spiking Neural Networks Exploiting Memristive Devices.* Front. Comput. Neurosci., vol. **16** (2022).

[80] Prezioso M., Mahmoodi M. R., Bayat F. M., Nili H., Kim H., Vincent A., Strukov D. B. *Spike-timing-dependent plasticity learning of coincidence detection with passively integrated memristive circuits.* Nat. Commun., vol. **9**, 5311 (2018).

[81] Demin V. A., Nekhaev D. V., Surazhevsky I. A., Nikiruy K. E., Emelyanov A. V., Nikolaev S. N. *Necessary conditions for STDP-based pattern recognition learning in a memristive spiking neural network.* Neural Netw., vol. **134**, 64-75 (2021).

[82] Amirsoleimani A., Alibart F., Yon V., Xu J., Pazhouhandeh M. R., Ecoffey S., Beilliard Y., Genov R., Drouin D. A. *In-memory vector-matrix multiplication in monolithic complementary metal-oxide-semiconductor-memristor integrated circuits: design choices, challenges, and perspectives.* Adv. Intell. Syst., vol. **2**, 2000115 (2020).

[83] Saïghi S., Mayr C. G., Serrano-Gotarredona T., Schmidt H. *et al. Plasticity in memristive devices for spiking neural networks.* Front. Neurosci., vol. **9**, 123457 (2015).

[84] Softky W. R., Koch C. *The highly irregular firing of cortical cells is inconsistent with temporal integration of random EPSPs.* J. Neurosci., vol. **13**, 334-350 (1993).

[85] Mainen Z. F., Sejnowski T. J. *Reliability of spike timing in neocortical neurons.* Science, vol. **268**, 1503-1506 (1995).

[86] Stevens C. F., Zador A. M. *Input synchrony and the irregular firing of cortical neurons.* Nat. Neurosci., vol. **1**, 210-217 (1998).

[87] Ishida K., Byun I., Nagaoka I., Fukumitsu K., Tanaka M., Kawakami S., Tanimoto T., Ono T., Kim J., Inoue K. *Superconductor computing for neural networks.* IEEE Micro, vol. **41**, 19-26 (2021).

[88] Semenov V. K., Golden E. B., Tolpygo S. K. *A new family of bioSFQ logic/memory cells.* IEEE Trans Appl. Supercond., vol. **32**, 1-5 (2021).

[89] Semenov V. K., Golden E. B., Tolpygo S. K. *BioSFQ circuit family for neuromorphic computing: Bridging digital and analog domains of superconductor technologies.* IEEE Trans Appl. Supercond., vol. **5**, 1-8 (2023).

[90] Herr Q. P., Herr A. Y., Oberg O. T., Ioannedis A. G. *Ultra-low-power superconductor logic.* J. Appl. Phys., vol. **109**, 103903 (2011).

[91] Mukhanov O. A. *Energy-Efficient Single Flux Quantum Technology.* IEEE Trans Appl. Supercond., vol. **21**, 760 (2011).

[92] Tanaka M., Ito M., Kitayama A., Kouketsu T., Fujimak, A. *18-GHz, 4.0-aJ/bit operation of ultra-low-energy rapid single-flux-quantum shift registers.* Jpn. J. Appl. Phys., vol. **51**, 053102 (2012).

[93] Soloviev I. I., Klenov N. V., Bakurskiy S. V., Kupriyanov M. Yu., Gudkov A. L., Sidorenko A. S. *Beyond Moore's technologies: operation principles of a superconductor alternative.* Beilstein J. Nanotechnol., vol. **8**, 2689-2710 (2017).

[94] Semenov V. K., Polyakov Y. A., Tolpygo S. K. *AC-biased shift registers as fabrication process benchmark circuits and flux trapping diagnostic tool.* IEEE Trans. Appl. Supercond., vol. **27**, 1-9 (2017).

[95] Przybysz J. X., Miller D. L., Toepfer H., Mukhanov O., Lisenfeld J., Weides M., Rotzinger H., Febvre P. *Superconductor Digital Electronics, chapter in Applied Superconductivity: Handbook on Devices and Applications.* Wiley-VCH Verlag GmbH & Co. KGaA: Weinheim, Germany, p. 1111-1206 (2015).

[96] Josephson B. D. *Possible new effects in superconductive tunnelling.* Phys. Lett., vol. **1**, 251-253 (1962).

[97] Anderson P. W., Rowell J. M. *Probable observation of the Josephson superconducting tunneling effect.* Phys. Rev. Lett., vol. **10**, 230 (1963).

[98] Tolpygo S. K., Bolkhovsky V., Oates D. E., Rastogi R., Zarr S., Day A. L., Weir T. J., Wynn A., Johnson L. M. *Superconductor electronics fabrication process with MoNx kinetic inductors and self-shunted Josephson junctions.* IEEE Trans. Appl. Supercond., vol. **28**, 1100212 (2018).

[99] Tolpygo S. K., Golden E. B., Weir T. J., Bolkhovsky V. *Inductance of superconductor integrated circuit features with sizes down to 120 nm.* Supercond. Sci. Technol., vol. **34**, 085005 (2021).

[100] Tolpygo S. K., Rastogi R., Weir T., Golden E. B., Bolkhovsky V. *Development of Self-Shunted Josephson Junctions for a Ten-Superconductor-Layer Fabrication Process: Nb/NbN$_x$/Nb Junctions.* IEEE Trans. Appl. Supercond., vol. **34**, 1-8 (2024).

[101] Castellanos-Beltran M. A., Olaya D. I., Sirois A. J., Dresselhaus P. D., Benz S. P., Hopkins P. F. *Stacked Josephson Junctions as Inductors for Single Flux Quantum Circuits.* IEEE Trans. Appl. Supercond., vol. **29**, 1-5 (2019).

[102] Roditchev D., Brun C., Serrier-Garcia L., Cuevas J. C., Bessa V. H. L., Milošević M. V., Debontridder F., Stolyarov V., Cren T. *Direct observation of Josephson vortex cores.* Nat. Phys., vol. **11**, 332 (2015).

[103] Stolyarov V. S., Cren T., Brun C., Golovchanskiy I. A., Skryabina O. V., Kasatonov D. I., Khapaev M. M., Kupriyanov M. Yu., Golubov A. A., Roditchev D. *Expansion of a superconducting vortex core into a diffusive metal.* Nat. Commun., vol. **9**, 2277 (2018).

[104] Grebenchuk S. Yu., Hovhannisyan R. A., Dremov V. V., Shishkin A. G., Chichkov V. I., Golubov A. A., Roditchev D., Krasnov V. M., Stolyarov V S. *Observation of interacting Josephson vortex chains by magnetic force microscopy.* Phys. Rev. Research, vol. **2**, 023105 (2020).

[105] Crotty P., Schult D., Segall K. *Josephson junction simulation of neurons.* Phys. Rev. E, vol. **82**, 011914 (2010).

[106] Skryabina O. V., Schegolev A. E., Klenov N. V., Bakurskiy S. V. *et al. Superconducting Bio-Inspired Au-Nanowire-Based Neurons.* Nanomaterials, vol. **12**, 1671 (2022).

[107] Schegolev A. E., Klenov N. V., Gubochkin G. I., Kupriyanov M. Yu., Soloviev I. I. *Bio-Inspired Design of Superconducting Spiking Neuron and Synapse.* Nanomaterials, vol. **13**, 2101 (2023).

[108] Karimov T., Ostrovskii V., Rybin V., Druzhina O., Kolev G., Butusov D. *Magnetic Flux Sensor Based on Spiking Neurons with Josephson Junctions.* Sensors, vol. **24**, 2367 (2024).

[109] Feldhoff F., Toepfer H. *Niobium neuron: RSFQ based bio-inspired circuit.* IEEE Trans. Appl. Supercond., vol. **31**, 1-5 (2021).

[110] Harada Y., Goto E. *Artificial neural network circuits with Josephson devices.* IEEE Trans. Magn., vol. **27**, 2863-2866 (1991).

[111] Yamanashi Y., Umeda K., Yoshikawa N. *Pseudo sigmoid function generator for a superconductive neural network.* IEEE Trans. Appl. Supercond., vol. **23**, 1701004 (2012).

[112] Feldhoff F., Toepfer H. *Short-and Long-Term State Switching in the Superconducting Niobium Neuron Plasticity.* IEEE Trans. Appl. Supercond., vol. **34**, 1-5 (2024).

[113] Schegolev A. E., Klenov N. V., Bakurskiy S. V., Soloviev I. I., Kupriyanov M. Yu., Tereshonok M. V., Sidorenko A. S. *Tunable superconducting neurons for networks based on radial basis functions.* Beilstein J. Nanotechnol., vol. **13**, 444-454 (2022).

[114] Karamuftuoglu M. A., Ucpinar B. Z., Fayyazi A., Razmkhah S., Kamal M., Pedram M. *Scalable Superconductor Neuron with Ternary Synaptic Connections for Ultra-Fast SNN Hardware.* arXiv preprint arXiv:2402.16384 (2024).

[115] Ucpinar B. Z., Karamuftuoglu M. A., Razmkhah S., Pedram M. *An On-Chip Trainable Neuron Circuit for SFQ-Based Spiking Neural Networks.* IEEE Trans. Appl. Supercond., vol. **34**, 1-6 (2024).

[116] Schneider M. L., Donnelly C. A., Russek S. E. *Tutorial: High-speed low-power neuromorphic systems based on magnetic Josephson junctions.* J. Appl. Phys., vol. **124**, 161102 (2018).

[117] Wu F., Meng H., Ma J. *Reproduced neuron-like excitability and bursting synchronization of memristive Josephson junctions loaded inductor.* Neural Netw., vol. **169**, 607-621 (2024).

[118] Tschirhart P., Segall K. *BrainFreeze: Expanding the Capabilities of Neuromorphic Systems Using Mixed-Signal Superconducting Electronics.* Front. Neurosci., vol. **15**, 750748 (2024).

[119] Schneider M. L., Segall K. *Fan-out and fan-in properties of superconducting neuromorphic circuits.* J. Appl. Phys., vol. **128**, 214903 (2020).

[120] Toomey E., Zhao Q.-Y., McCaughan A. N., Berggren K. K. *Frequency pulling and mixing of relaxation oscillations in superconducting nanowires.* Phys. Rev. Applied, vol. **9**, 064021 (2018).

[121] Toomey E., Segall K., Berggren K. K. *Design of a power efficient artificial neuron using superconducting nanowires.* Front. Neurosci., vol. **13**, 481146 (2019).

[122] Toomey E., Segall K., Berggren K. K. *Superconducting nanowire spiking element for neural networks.* Nano Lett., vol. **20**, 8059-8066 (2020).

[123] Astafiev O. V., Ioffe L. B., Kafanov S., Pashkin Yu. A., Arutyunov K. Yu., Shahar D., Cohen O., Tsai J. S. *Coherent quantum phase slip.* Nature, vol. **484**, 355-358 (2012).

[124] Cheng R., Goteti U. S., Walker H., Krause K. M., Oeding L., Hamilton M. C. *Toward Learning in Neuromorphic Circuits Based on Quantum Phase Slip Junctions.* Front. Neurosci., vol. **15**, 765883 (2021).

[125] Cheng R., Goteti U. S., Hamilton M. C. *Spiking neuron circuits using superconducting quantum phase-slip junctions.* J. Appl. Phys., vol. **124**, 152126 (2018).

[126] Liu J., Wu Q., Sui X., Qian C., Guohua G., Liping W., Shengcai L. *Research progress in optical neural networks: theory, applications and developments.* PhotoniX, vol. **2**, 5 (2021).

[127] Feldmann J., Youngblood N., Karpov M., Gehring H. *et al. Research progress in optical neural networks: theory, applications and developments.* Nature, vol. **589**, 52-58 (2021).

[128] Jha A., Huang C., Prucnal P. R. *Reconfigurable all-optical nonlinear activation functions.* 2020 IEEE Photonics Conference (IPC), p. 1-2 (2020).

[129] Tait A. N., Ferreira de Lima T., Nahmias M. A., Miller H. B., Peng H.-T., Shastri B. J., Prucnal P. R. *Silicon Photonic Modulator Neuron.* Phys. Rev. Applied, vol. **11**, 064043 (2019).

[130] Cheng Z., Ríos C., Pernice W. H. P., Wright C. D., Bhaskaran H. *On-chip photonic synapse.* Sci. Adv., vol. **3**, e1700160 (2017).

[131] Robertson J., Wade E., Kopp Y., Bueno J., Hurtado A. *Toward Neuromorphic Photonic Networks of Ultrafast Spiking Laser Neurons.* IEEE J. Sel. Top. Quantum Electron., vol. **26**, 1-15 (2020).

[132] Zhang Y., Robertson J., Xiang S., Hejda M., Bueno J., Hurtado A. *All-optical neuromorphic binary convolution with a spiking VCSEL neuron for image gradient magnitudes.* Photon. Res., vol. **5**, B201-B209 (2021).

[133] Peng H.-T., Angelatos G., de Lima T. F., Nahmias M. A., Tait A. N., Abbaslou S., Shastri B. J., Prucnal P. R. *Temporal Information Processing With an Integrated Laser Neuron.* IEEE J. Sel. Top. Quantum Electron., vol. **26**, 1-9 (2020).

[134] Feldmann J., Youngblood N., David Wright, C., Bhaskaran H., Pernice W. H. P. *All-optical spiking neurosynaptic networks with self-learning capabilities.* Nature, vol. **569**, 208-214 (2019).

[135] Nahmias M. A., Shastri B. J., Tait A. N., de Lima T. F., Prucnal P. R. *All-optical spiking neurosynaptic networks with self-learning capabilities.* Opt. Photon. News, vol. **29**, 34-41 (2018).

[136] Cao T., Wang R., Simpson R. E., Li G. *Photonic Ge-Sb-Te phase change metamaterials and their applications.* Progr. Quant. Electr., vol. **74**, 100299 (2020).

[137] Raeis-Hosseini N., Rho J. *Metasurfaces Based on Phase-Change Material as a Reconfigurable Platform for Multifunctional Devices.* Materials, vol. **10**, 1046 (2017).

[138] Ríos C., Youngblood N., Cheng Z., Le Gallo M., Pernice W. H. P., Wright C. D., Sebastian A., Bhaskaran H. *In-memory computing on a photonic platform.* Sci. Adv., vol. **5**, eaau5759 (2019).

[139] Ríos C., Stegmaier V., Hosseini P., Wang D., Scherer T., Wright C. D., Bhaskaran H., Pernice W. H. P. *Integrated all-photonic non-volatile multi-level memory.* Nat. Photon., vol. **9**, 725 (2015).

[140] Stegmaier M., Rios C., Bhaskaran H., Wright C. D., Pernice W. H. P. *Nonvolatile all-optical 1×2 switch for chipscale photonic networks.* Adv. Opt. Mater., vol. **5**, 1600346 (2016).

[141] Zheng J., Khanolkar A., Xu P., Colburn S., Deshmukh S., Myers J., Frantz J., Pop E., Hendrickson J., Doylend J., Boechler N., Majumdar A. *GST-on-silicon hybrid nanophotonic integrated circuits: a non-volatile quasi-continuously reprogrammable platform.* Opt. Mater. Express, vol. **8**, 1551-1561 (2018).

[142] Chakraborty I., Saha G., Sengupta A., Roy K. *Toward fast neural computing using all-photonic phase change spiking neurons.* Sci. Rep., vol. **8**, 12980 (2018).

[143] Kuzum D., Jeyasingh R. G., Lee B., Wong H. S. *Nanoelectronic programmable synapses based on phase change materials for brain-inspired computing.* Nano Lett., vol. **12**, 2179 (2012).

[144] Ji R., Zhang L., Tian Y., Ding J., Yang L. *On-chip CMOS-compatible optical signal processor.* in Asia Communications and Photonics Conference, OSA Technical Digest (online) (Optica Publishing Group, 2012), paper AF4A.4

[145] Chakraborty I., Saha G., Roy K. *Photonic In-Memory Computing Primitive for Spiking Neural Networks Using Phase-Change Materials.* Phys. Rev. Applied, vol. **11**, 014063 (2019).

[146] Pei S., Tang S., Yan S., Jiang S., Zhang X., Zheng Z. *How to enhance the dynamic range of excitatory-inhibitory excitable networks.* Phys. Rev. E, vol. **86**, 021909 (2012).

[147] Rinzel J., Huguet G. *Nonlinear Dynamics of Neuronal Excitability, Oscillations, and Coincidence Detection.* Commun. Pure Appl. Math., vol. **66**, 1464 (2013).

[148] Hurtado A., Quirce A., Valle A., Pesquera L., Adams M. J. *Nonlinear dynamics induced by parallel and orthogonal optical injection in 1550 nm Vertical-Cavity Surface-Emitting Lasers (VCSELs).* Opt. Express, vol. **18**, 9423 (2010).

[149] Kingni S. T., Van der Sande, G. and Gelens L., Erneux T., Danckaert, J. *Direct modulation of semiconductor ring lasers: Numerical and asymptotic analysis.* Opt. Soc. Am. B, vol. **29**, 1983 (2012).

[150] Lu, Y and Zhang, W and Fu, B and He Z. *Frequency-switched photonic spiking neurons.* Opt. Express, vol. **30**, 21599 (2022).

[151] Romeira B., Figueiredo J. M. L., Javaloyes J. *Delay dynamics of neuromorphic optoelectronic nanoscale resonators: Perspectives and applications.* Chaos, vol. **27**, 114323 (2017).

[152] Cimbri D., Wang J., Al-Khalidi A., Wasige E. *Resonant Tunneling Diodes High-Speed Terahertz Wireless Communications – A Review.* IEEE Trans. Terahertz Sci. Technol., vol. **12**, 226-244 (2022).

[153] Zhang W., Hejda M., Malysheva E., Al-Taai Q. R. A., Javaloyes J., Wasige E., Figueiredo J. M. L., Dolores-Calzadilla V., Romeira B., Hurtado A. *Tunable presynaptic weighting in optoelectronic spiking neurons built with laser-coupled resonant tunneling diodes.* J. Phys. D: Appl. Phys., vol. **56**, 084001 (2023).

[154] Nahmias M. A., Shastri B. J., Tait A. N., Prucnal P. R. *A Leaky Integrate-and-Fire Laser Neuron for Ultrafast Cognitive Computing.* IEEE J. Sel. Top. Quantum Electron., vol. **19**, 1-12 (2013).

[155] Nahmias M. A., Tait A. N., Shastri B. J., de Lima F. T., Prucnal P. R. *Excitable laser processing network node in hybrid silicon: analysis and simulation.* Opt. Express, vol. **20**, 26800-26813 (2015).

[156] Prucnal P. R., Shastri B. J., de Lima T. F., Nahmias M. A., Tait A. N. *Recent progress in semiconductor excitable lasers for photonic spike processing.* Adv. Opt. Photon., vol. **8**, 228-299 (2015).

[157] Robertson J., Deng T., Javaloyes J., Hurtado A. *Controlled inhibition of spiking dynamics in VCSELs for neuromorphic photonics: theory and experiments.* Optics Lett., vol. **42**, 1560-1563 (2017).

[158] Hurtado A., Henning I. D., Adams M. J. *Optical neuron using polarisation switching in a 1550nm–VCSEL.* Opt. Express, vol. **18**, 25170-25176 (2010).

[159] Robertson J., Wade E., Hurtado A. *Electrically Controlled Neuron-Like Spiking Regimes in Vertical-Cavity Surface-Emitting Lasers at Ultrafast Rates.* IEEE J. Sel. Top. Quantum Electron., vol. **25**, 1-7 (2019).

[160] Deng T., Robertson J., Hurtado A. *Controlled Propagation of Spiking Dynamics in Vertical-Cavity Surface-Emitting Lasers: Towards Neuromorphic Photonic Networks.* IEEE J. Sel. Top. Quantum Electron., vol. **23**, 1-7 (2017).

[161] Xiang S., Zhang Y., Gong J., Guo X., Lin L., Hao Y. *STDP–Based Unsupervised Spike Pattern Learning in a Photonic Spiking Neural Network With VCSELs and VCSOAs.* IEEE J. Sel. Top. Quantum Electron., vol. **25**, 1-9 (2020).

[162] Ma B., Zou W. *Demonstration of a distributed feedback laser diode working as a graded-potential-signaling photonic neuron and its application to neuromorphic information processing.* Sci. China Inf. Sci., vol. **63**, 160408 (2020).

[163] Toole R., Tait A. N., de Lima T. F., Nahmias M. A., Shastri B. J., Prucnal P. R., Fok M. P. *STDP–Based Unsupervised Spike Pattern Learning in a Photonic Spiking Neural Network With VCSELs and VCSOAs.* J. Light. Technol., vol. **34**, 470-476 (2016).

[164] Coomans W., Gelens L., Beri S., Danckaert J., Van der Sande G. *Solitary and coupled semiconductor ring lasers as optical spiking neurons.* Phys. Rev. E, vol. **84**, 036209 (2011).

[165] Kelleher B., Bonatto C., Huyet G., Hegarty S. P. *Excitability in optically injected semiconductor lasers: Contrasting quantum-well- and quantum-dot-based devices.* Phys. Rev. E, vol. **83**, 026207 (2011).

[166] Kelleher B., Goulding D., Hegarty S. P., Huyet G., Cong D.-Y., Martinez A., Lemaître A., Ramdane A., Fischer M., Gerschütz F., J. Koeth J. *Excitable phase slips in an injection-locked single-mode quantum-dot laser.* Optics Lett., vol. **34**, 440-442 (2009).

[167] Alexander K., Van Vaerenbergh T., Fiers M., Mechet P., Dambre J., Bienstman P. *Excitable phase slips in an injection-locked single-mode quantum-dot laser.* Opt. Express, vol. **21**, 26182-26191 (2012).

[168] Shastri B. J., Nahmias M. A., Tait A. N., Rodriguez A. W., Wu B., Prucnal P. R. *Spike processing with a graphene excitable laser.* Sci. Rep., vol. **6**, 19126 (2016).

[169] Berggren K., Xia Q., Likharev K. K., Strukov D. B. *et al. Roadmap on emerging hardware and technology for machine learning.* Nanotechnol., vol. **32**, 012002 (2020).

[170] Shainline J. M., Buckley S. M., McCaughan A. N., Chiles J., Jafari-Salim A., Mirin R. P., Nam S. W. *Circuit designs for superconducting optoelectronic loop neurons.* J. Appl. Phys., vol. **124**, 152130 (2018).

[171] Shainline J. M., Buckley S. M., McCaughan A. N., Chiles J. T., Jafari S. A., Castellanos-Beltran M., Donnelly C. A., Schneider M. L., Mirin R. P., Nam S. W. *Superconducting optoelectronic loop neurons.* J. Appl. Phys., vol. **126**, 044902 (2019).

[172] Khan S., Primavera B. A., Chiles J., McCaughan A. N. *et al.*, *Superconducting optoelectronic single-photon synapses.* Nat. Electron., vol. **5**, 650 (2022).

[173] Shainline J. M., Primavera B. A., Khan S. *Phenomenological model of superconducting optoelectronic loop neurons.* Phys. Rev. Research, vol. **5**, 013164 (2023).

[174] Pashin D. S., Pikunov P. V., Bastrakova M. V., Schegolev A. E., Klenov N. V., Soloviev I. I. *A bifunctional superconducting cell as flux qubit and neuron.* Beilstein J. Nanotechnol., vol. **14**, 1116-1126 (2023).

[175] Suárez L. E., Richards B. A., Lajoie G., Misic B. *Learning function from structure in neuromorphic networks.* Nat. Mach. Intell., vol. **3**, 771-786 (2021).

[176] Cai H., Ao Z., Tian C., Wu Z., Liu H., Tchieu J., Gu M., Mackie K., Guo F. *Brain organoid reservoir computing for artificial intelligence.* Nat. Electron., vol. **6**, 1032-1039 (2023).

[177] Suárez L. E., Mihalik A., Milisav F., Marshall K., Li M., Vértes P. E., Lajoie G., Misic B. *Connectome-based reservoir computing with the conn2res toolbox.* Nat. Commun., vol. **15**, 656 (2024).

[178] Smirnova L., Caffo B. S., Gracias D. H., Huang Q. *et al. Organoid intelligence (OI): the new frontier in biocomputing and intelligence-in-a-dish.* Front. Sci., vol. **1**, 1017235 (2024).

Editor's note: We invite readers to explore the philosophy of the Journal [V. Stolyarov, Mesosci. Nanotechnol., vol. 1, 01001 (2023)] and consider the possibility of submitting their contributions for publication in our Journal.

Mesoscience and Nanotechnology

Mesoscience & Nanotechnology is a peer-reviewed interdisciplinary journal that publishes original research articles, letters, reviews, methods and perspectives across all fields of physics, chemistry, materials science, and related disciplines, focusing on processes and materials at the nano- and mesoscopic levels. The journal provides an open-access and free-of-charge platform for the fast communication of scientists, engineers, and other researchers in the rapidly growing areas of mesoscience and nanotechnology. Mesoscience & Nanotechnology welcomes both experimental and theoretical papers that emphasize the in-depth understanding of nano- and mesoscale physics, the reporting of new phenomena (especially for letters), and linking the fundamental results with practical applications.

ISSN: 3034-6622 (electronic)

Membership in the Crossref (2025)

Publication in the Mesoscience & Nanotechnology is free of charge

Key topics: Superconductivity/Superconducting Devices, Nanoelectronics/Nanotechnology, Surfaces/Interfaces, Functional Materials/Fabrication and Properties, Quantum Physics and Materials, Topologically Protected Electronic Phenomena, 2D Materials and Devices, Quantum Dots, Low-dimensional Magnetism, Strongly-correlated Electronic Systems, Heterostructures and Superlattices, Ferroelectricity, Thin Films, Neuromorphic Systems, Nanobiotechnology, New Methods

Types of publications: Article, Review, Letter, Perspectives, Methods

Types of review process**:** Single-Blind Review, Double-Blind Review

E-mail: editor.chief@phtreatise.com
Web-pages: https://jmsn.press, https://colab.ws
Publisher: Treatise LLC, Moscow, Russia
Publisher's address: 3A Dolgoprudnenskoe Highway, office 262,
Moscow, 117148, Russia

Treatise

CoLab connected

The hardcover edition is sponsored by акметрон

Limited print run of 100 copies